Doctoral thesis for the degree of Doctor of Philosophy

Excursions along the Drip line

By

Thomas Nilsson

Department of Physics
Chalmers University of Technology
S-412 96 Göteborg, Sweden

Göteborg 1995

ISBN 91-7197-215-3

Reproservice, Chalmers Bibliotek
Göteborg 1995

List of publications

This thesis is based on work reported in the following papers:

I. Experimental determination of cross-talk between neutron detectors

M. Cronqvist, B. Jonson, T. Nilsson, G. Nyman, K. Riisager, H. Roth, Ö. Skeppstedt, O. Tengblad and K. Wilhelmsen

Nuclear Inst. and Meth. **A317**(1992)273-280

II. Study of charged particles emitted in the ß-decay of ^{6,8}He

M.J.G. Borge, L. Johannsen, B. Jonson, T. Nilsson, G. Nyman, K. Riisager, O. Tengblad, K. Wilhelmsen Rolander and the ISOLDE Collaboration

Nucl. Phys. **A560**(1993)664-676

III. Longitudinal and transverse momentum distributions of ^{9}Li fragments from break-up of ^{11}Li

F. Humbert, T. Nilsson, W. Schwab, M. Zinser, Th. Blaich, M.J.G. Borge, L.V. Chulkov, H. Eickhoff, Th.W. Elze, H. Emling, B. Franzke, H. Freiesleben, H. Geissel, K. Grimm, D. Guillemaud-Mueller, P.G. Hansen, R. Holzmann, H. Irnich, L. Johannsen, B. Jonson, J.G. Keller, O. Klepper, H. Klingler, J.V. Kratz, R. Kulessa, D. Lambrecht, Y. Leifels, A. Magel, M. Mohar, A.C. Mueller, G. Münzenberg, P. Møller, F. Nickel, G. Nyman, A. Richter, K. Riisager, C. Scheidenberger, G. Schrieder, B.M. Sherrill, H. Simon, K. Stelzer, J. Stroth, O. Tengblad, W. Trautmann, E. Wajda and E. Zude

Phys. Lett. **B347**(1995)198-204

IV. **Neutron momentum distributions from ”core break-up” reactions of halo nuclei**

T. Nilsson, Th. Blaich, M.J.G. Borge, L.V. Chulkov, Th.W. Elze, H. Emling, H. Geissel, K. Grimm, D. Guillemaud-Mueller, P.G. Hansen, R. Holzmann, P. Hornshøj, F. Humbert, H. Irnich, L. Johannsen, B. Jonson, M. Keim, J.G. Keller, H. Klingler, J.V. Kratz, R. Kulessa, D. Lambrecht, Y. Leifels, M. Lewitowicz, A. Magel, M.F. Mohar, A.C. Mueller, G. Münzenberg, R. Neugart, F. Nickel, G. Nyman, A. Richter, K. Riisager, M.-G. Saint-Laurent, C. Scheidenberger, G. Schrieder, W. Schwab, B.M.Sherrill, H. Simon, O. Sorlin, K. Stelzer, J. Stroth, O. Tengblad, E. Wajda, K. Wilhelmsen Rolander, M. Zinser and E. Zude

Europhys. Lett., **30**(1995)19-24

V. **Study of the unstable nucleus ^{10}Li in stripping reactions of the radioactive projectiles ^{11}Be and^{11}Li**

M. Zinser, F. Humbert, T. Nilsson, W. Schwab, Th. Blaich, M.J.G. Borge, L.V. Chulkov, Th.W. Elze, H. Emling, H. Freiesleben, H. Geissel, K. Grimm, D. Guillemaud-Mueller, P.G. Hansen, R. Holzmann, H. Irnich, B. Jonson, J.G. Keller, H. Klingler, J.V. Kratz, R. Kulessa, D. Lambrecht, Y. Leifels, A. Magel, M. Mohar, A.C. Mueller, G. Münzenberg, F. Nickel, G. Nyman, A. Richter, K. Riisager, C. Scheidenberger, G. Schrieder, B.M. Sherrill, H. Simon, K. Stelzer, J. Stroth, O. Tengblad, W. Trautmann, E. Wajda and E. Zude

Phys. Rev. Lett. **75**(1995)1719-1722

VI. **^{6}He and neutron momentum distributions from ^{8}He in nuclear break-up reactions at 240 MeV/u**

T. Nilsson, F. Humbert, W. Schwab, M.H. Smedberg, M. Zinser, Th. Blaich, M.J.G. Borge, L.V. Chulkov, Th.W. Elze, H. Emling, H. Freiesleben, H. Geissel, K. Grimm, D. Guillemaud-Mueller, P.G. Hansen, R. Holzmann, H. Irnich, B. Jonson, J.G. Keller, H. Klingler, A.A. Korsheninnikov, J.V. Kratz, R. Kulessa, D. Lambrecht, Y. Leifels, A. Magel, M. Mohar, A.C. Mueller, G. Münzenberg, F. Nickel, G. Nyman, A. Richter, K. Riisager, C. Scheidenberger, G. Schrieder, B.M. Sherrill, H. Simon, K. Stelzer, J. Stroth, O. Tengblad, W. Trautmann, E. Wajda, M.V. Zhukov and E. Zude

Internal report CTHSP 95/12, submitted to Nucl. Phys. A

List of publications

This thesis is based on work reported in the following papers:

I. Experimental determination of cross-talk between neutron detectors

M. Cronqvist, B. Jonson, T. Nilsson, G. Nyman, K. Riisager, H. Roth, Ö. Skeppstedt, O. Tengblad and K. Wilhelmsen

Nuclear Inst. and Meth. **A317**(1992)273-280

II. Study of charged particles emitted in the ß-decay of ^{6,8}He

M.J.G. Borge, L. Johannsen, B. Jonson, T. Nilsson, G. Nyman, K. Riisager, O. Tengblad, K. Wilhelmsen Rolander and the ISOLDE Collaboration

Nucl. Phys. **A560**(1993)664-676

III. Longitudinal and transverse momentum distributions of ^{9}Li fragments from break-up of ^{11}Li

F. Humbert, T. Nilsson, W. Schwab, M. Zinser, Th. Blaich, M.J.G. Borge, L.V. Chulkov, H. Eickhoff, Th.W. Elze, H. Emling, B. Franzke, H. Freiesleben, H. Geissel, K. Grimm, D. Guillemaud-Mueller, P.G. Hansen, R. Holzmann, H. Irnich, L. Johannsen, B. Jonson, J.G. Keller, O. Klepper, H. Klingler, J.V. Kratz, R. Kulessa, D. Lambrecht, Y. Leifels, A. Magel, M. Mohar, A.C. Mueller, G. Münzenberg, P. Møller, F. Nickel, G. Nyman, A. Richter, K. Riisager, C. Scheidenberger, G. Schrieder, B.M. Sherrill, H. Simon, K. Stelzer, J. Stroth, O. Tengblad, W. Trautmann, E. Wajda and E. Zude

Phys. Lett. **B347**(1995)198-204

IV. **Neutron momentum distributions from ”core break-up” reactions of halo nuclei**

T. Nilsson, Th. Blaich, M.J.G. Borge, L.V. Chulkov, Th.W. Elze, H. Emling, H. Geissel, K. Grimm, D. Guillemaud-Mueller, P.G. Hansen, R. Holzmann, P. Hornshøj, F. Humbert, H. Irnich, L. Johannsen, B. Jonson, M. Keim, J.G. Keller, H. Klingler, J.V. Kratz, R. Kulessa, D. Lambrecht, Y. Leifels, M. Lewitowicz, A. Magel, M.F. Mohar, A.C. Mueller, G. Münzenberg, R. Neugart, F. Nickel, G. Nyman, A. Richter, K. Riisager, M.-G. Saint-Laurent, C. Scheidenberger, G. Schrieder, W. Schwab, B.M.Sherrill, H. Simon, O. Sorlin, K. Stelzer, J. Stroth, O. Tengblad, E. Wajda, K. Wilhelmsen Rolander, M. Zinser and E. Zude

Europhys. Lett., **30**(1995)19-24

V. **Study of the unstable nucleus ^{10}Li in stripping reactions of the radioactive projectiles ^{11}Be and^{11}Li**

M. Zinser, F. Humbert, T. Nilsson, W. Schwab, Th. Blaich, M.J.G. Borge, L.V. Chulkov, Th.W. Elze, H. Emling, H. Freiesleben, H. Geissel, K. Grimm, D. Guillemaud-Mueller, P.G. Hansen, R. Holzmann, H. Irnich, B. Jonson, J.G. Keller, H. Klingler, J.V. Kratz, R. Kulessa, D. Lambrecht, Y. Leifels, A. Magel, M. Mohar, A.C. Mueller, G. Münzenberg, F. Nickel, G. Nyman, A. Richter, K. Riisager, C. Scheidenberger, G. Schrieder, B.M. Sherrill, H. Simon, K. Stelzer, J. Stroth, O. Tengblad, W. Trautmann, E. Wajda and E. Zude

Phys. Rev. Lett. **75**(1995)1719-1722

VI. **^{6}He and neutron momentum distributions from ^{8}He in nuclear break-up reactions at 240 MeV/u**

T. Nilsson, F. Humbert, W. Schwab, M.H. Smedberg, M. Zinser, Th. Blaich, M.J.G. Borge, L.V. Chulkov, Th.W. Elze, H. Emling, H. Freiesleben, H. Geissel, K. Grimm, D. Guillemaud-Mueller, P.G. Hansen, R. Holzmann, H. Irnich, B. Jonson, J.G. Keller, H. Klingler, A.A. Korsheninnikov, J.V. Kratz, R. Kulessa, D. Lambrecht, Y. Leifels, A. Magel, M. Mohar, A.C. Mueller, G. Münzenberg, F. Nickel, G. Nyman, A. Richter, K. Riisager, C. Scheidenberger, G. Schrieder, B.M. Sherrill, H. Simon, K. Stelzer, J. Stroth, O. Tengblad, W. Trautmann, E. Wajda, M.V. Zhukov and E. Zude

Internal report CTHSP 95/12, submitted to Nucl. Phys. A

Excursions along the Drip line

1. Introduction

1.1 Subatomic physics - its past and present

The subject of subatomic physics is soon completing its first century, beginning with Henri Bequerel's discovery of radioactivity in 1896. It has been *the* ultimate research subject for decades, with its fast progress, huge experimental facilities and useful/horrifying applications which are a part of every man's imagination. The comparatively large resources given to subatomic physics research have brought us to a situation where we have a reasonable understanding of the subatomic world. Especially the research traditionally labelled **nuclear physics** has been able to explain the atomic nucleus to a very high degree. Are there still fundamental questions to answer within nuclear physics, or should the field be subject to applied research only?

The fact that we now rather well understand nuclei under normal conditions does not mean that we have the complete picture of the complicated many-body system that constitutes an atomic nucleus. To answer all our questions, the theories must be tested upon nuclear matter which is not in equilibrium with regard to temperature, spin and isospin. There is currently a large activity within the subatomic physics community to proceed further and further along these directions. This is made possible by the rapid development of accelerators, isotope separators, detection systems, fast read-out electronics and adequate data analysis tools, giving new input for the theorists to refine their calculations.

The theoretical limits for large isospin values – large inequalities in the neutron and proton number – are the neutron and proton drip lines, where further addition of neutrons or protons is impossible due to negative binding energies for the last nucleon. The very lightest region of the chart of nuclides is at present the only one where the neutron and proton drip line can be reached experimentally. More than 2000 additional nuclides, not yet experimentally accessible, are expected to be bound, mainly on the neutron rich side of the valley of stability due to the Coulomb repulsion prohibiting formation of extremely neutron deficient nuclei. This work deals with the phenomena found in light neutron-rich nuclei at the neutron drip line, concentrating upon the neutron-halo nucleus ^{11}Li but with additional results regarding ^{6,8}He and ^{11}Be.

1.2 The halo nuclei discovered

One of the most spectacular findings within nuclear physics in recent years is the discovery of a **neutron halo** in some nuclei at the neutron drip line. The best known case is ^{11}Li for which a model has been developed, and gradually confirmed by experiments, describing this nucleus as an inert core of ^{9}Li surrounded by two loosely bound neutrons at large distance. We will here take a look upon the various experimental investigations that have been important for our understanding of this phenomenon.

1.2.1 Total interaction cross section

The adventure of halo nuclei started with measurements of the total interaction cross section for light, neutron-rich nuclei. This was done in 1985 by Tanihata and co-workers with secondary beams of 790 MeV/u [1], and from the results a matter radius could be deduced according to **(1.1)**.

$$\frac{I}{I_0} = e^{-\sigma_I \rho t}$$
$$\sigma_I = \pi [R_I(P) + R_I(T)]^2 \qquad \textbf{(1.1)}$$
$$R_I(P) \Rightarrow \langle r^2_{\text{matter}} \rangle^{1/2}$$

with

- I/I_0 - relative intensity change when passing the secondary reaction target
- σ_I - total interaction cross section
- ρ - target density (atoms/cm^3)
- t - target thickness (cm)
- $R_I(P)$ - radius of projectile nucleus
- $R_I(T)$ - radius of target nucleus

The results are compiled in figure 1.1. As can be seen, there is a drastic increase in matter radius as we go from ^{9}Li to ^{11}Li. The missing point for ^{10}Li indicates that this nucleus is unbound. Furthermore, there is a large increase in matter radius when going from ^{4}He to ^{6}He.

The data inspired P.G. Hansen and B. Jonson to develop a simple model [2] in order to describe this anomalous behaviour. A calculation analogous to what can be made for the deuteron was made, substituting the proton with a ^{9}Li nucleus and the neutron with a dineutron. With the low two-neutron separation energy, as much as 80 % of the dineutron wavefunction is outside the nuclear potential.

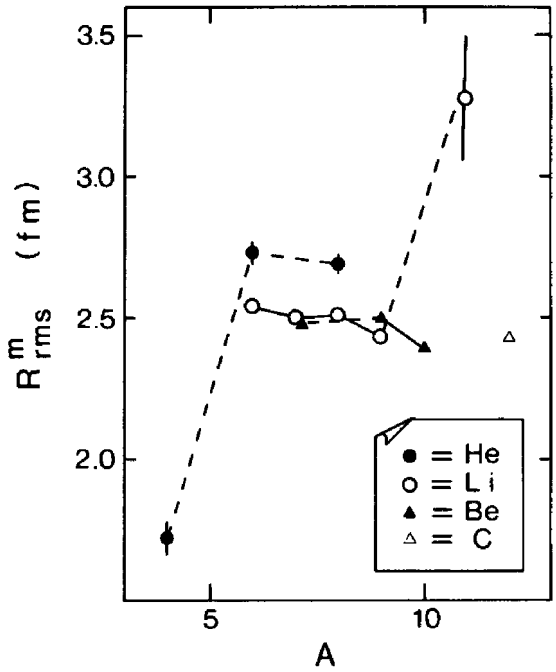

Fig. 1.1. Deduced matter radii for some neutron rich helium and lithium isotopes. The data were obtained with a secondary beam energy of 790 MeV/u. From ref. [1].

This simple model was soon modified to take into account a picture where the core and two halo neutrons are treated as a three-body system [3]. See figure 1.2 for a simplified view of the configuration.

The halo phenomenon is not limited to the case of ^{11}Li, although it is the standard example. In fig. 1.3 an overview of the experimentally known halo nuclei is shown.

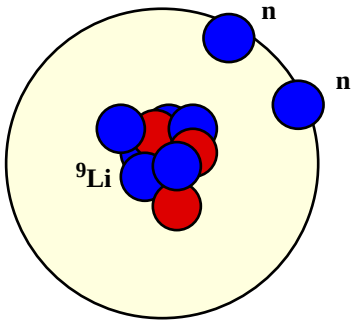

Fig. 1.2. Schematic picture of the neutron halo configuration in ^{11}Li.

The halo nuclei discovered

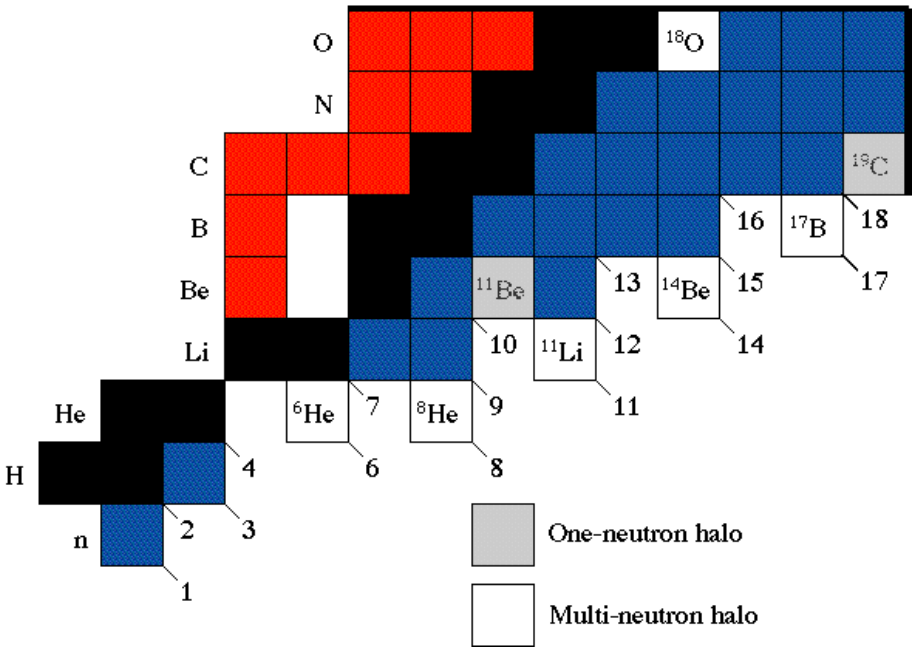

Fig. 1.3. Overview of the drip-line nuclei with a confirmed halo structure. The term multi-neutron halo is used to cover the case of ^{8}He, having four outer neutrons surrounding an α-core.

1.2.2 Quadrupole and dipole moments

Why this somewhat complicated, previously unknown halo picture? A large r.m.s. value of the radius is also found in nuclei being deformed which would provide a more natural solution to this anomaly. To clear this question, very important measurements of the quadrupole moment of ^{11}Li have been made with ß-NMR spectroscopy [4] at ISOLDE, CERN. The value relative to the quadrupole moment of ^{9}Li was measured and gave the result $\left|(Q(^{11}Li))/(Q(^{9}Li))\right| = 1.14(16)$, excluding a strong deformation of ^{11}Li and supporting the picture of a ^{9}Li core, unchanged by the additional neutrons.

The nuclear spin and magnetic moment of ^{11}Li were measured with a similar method, yielding the values $I = 3/2$ and $\mu_I = 3.6673(25)$ n.m. [5]. The latter is very close to the single-particle Schmidt value, $\mu_{Schmidt} = 3.792$ n.m. , expected for a spherical nucleus. Thus, no evidence of deformation in ^{11}Li is found from the optical data available.

1.2.3 Single-neutron angular distribution

The first measurement of neutrons from dissociation of a halo nucleus was made by Anne et al. [6]. The incoming beam hit a target, the charged fragments were identified in a silicon-detector telescope and the neutrons were detected in an array of liquid-scintillator detectors. Thus, angular distributions of the neutrons from the dissociation could be measured. The results for ^{11}Li and ^{9}Li are shown in fig. 1.4. The neutrons

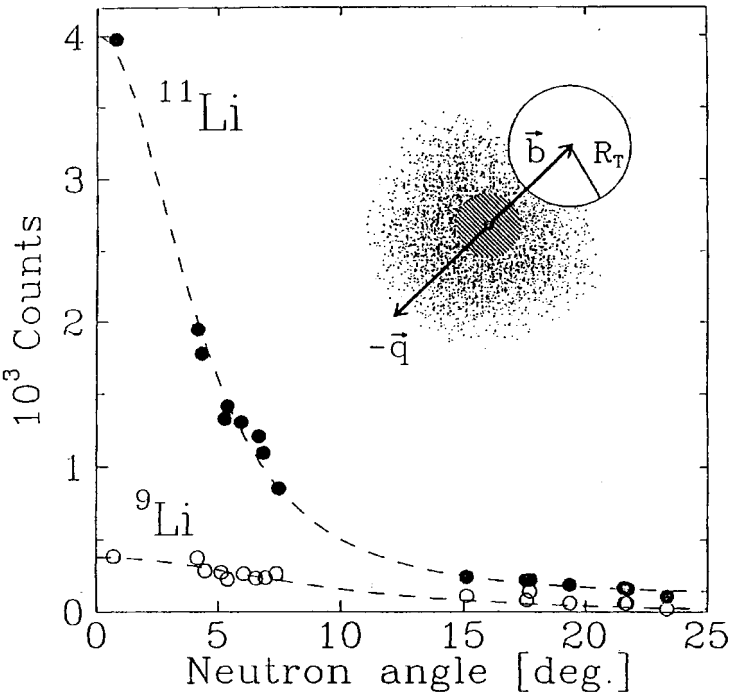

Fig. 1.4. Neutron angular distributions from dissociation of ^{11}Li and ^{9}Li. From ref. [6].

from the former exhibit a very narrow angular distribution compared to the more "normal" distribution in the case of ^{9}Li. In the framework of the Serber model [7], or the sudden approximation, the dissociated nucleon is very little perturbed by the reaction process and thus carries its initial internal momentum. According to Heisenberg´s uncertainty relation we have

$$\overline{(\Delta p)^2}\,\overline{(\Delta x)^2} \geq \hbar^2/4 \quad . \tag{1.2}$$

Thus, a narrow momentum distribution implies **(1.2)** a large spatial extension of the neutron wave function. This is a signal of a neutron halo.

1.2.4 Matter radius versus charge radius

A very illustrative experiment supporting the halo picture was done by Blank and coworkers [8], measuring the charge-changing and total reaction cross sections for Li isotopes. See fig. 1.5. The data was taken with 80 MeV/u beam energy on a carbon target. As can be seen, the total interaction cross section rises drastically by adding two neutrons to ^{9}Li. In contrast, the charge-changing cross section is practically constant which favours the assumption that the ^{9}Li core is unperturbed by the halo neutrons.

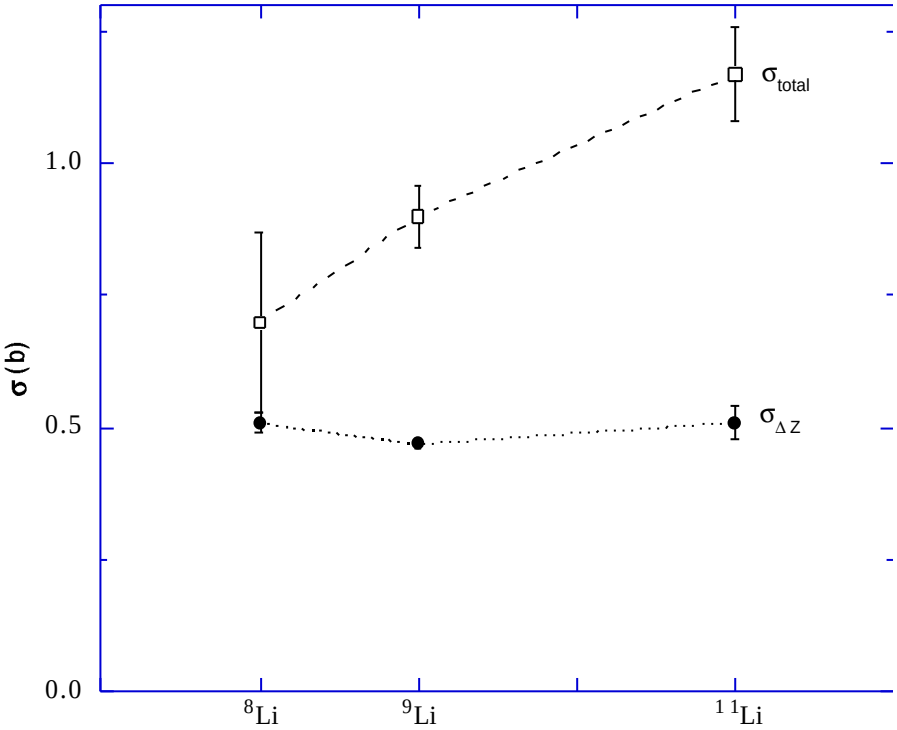

Fig. 1.5. Charge-changing (filled circles) and total reaction (hollow squares) cross sections for Li isotopes. From ref. [8].

1.2.5 ß-delayed particle emission

Another way to study halo nuclei is to investigate their decay modes. The use of ß-delayed particle emission for nuclear structure studies is by no means a new method. During the years, a multitude of particle-emitting ß-delayed decay modes have been found experimentally as shown in table 1.1.

The lifetime of a halo nucleus is typically in the order of milliseconds. The Q-values for ß-decay are usually very high, 20.68 MeV in the case of ^{11}Li, which allows population of excited states above the particle emission threshold in the daughter nucleus. The most abundant nucleus with respect to exotic decay modes is ^{11}Li, with ß-delayed n-, 2n-, 3n-, t-, d-, α- and ^{6}He-emission. See fig. 1.6. The high Q-values found in this region of the nuclear chart can, to some extent, intuitively be understood by considering the large relative difference in the neutron and proton number when moving one step along the isobar, causing a large change in the asymmetry term in the semi-empirical mass formula.

That a high Q-value allows a multitude of decay modes might not be especially surprising. This is found e.g. in ^{9}Li, which does not exhibit an anomalous structure [9]. The interesting question is how and if it can be related to the halo structure and exploited in order to gain information about it. The key might be found in the strength

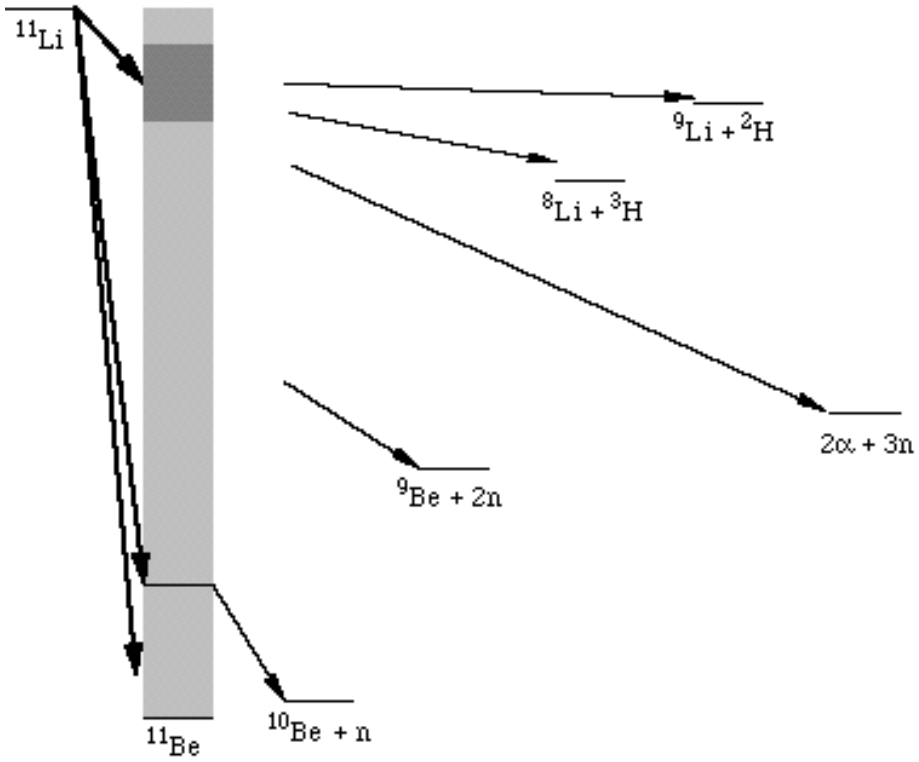

Fig. 1.6. Schematic picture of the experimentally confirmed beta-delayed particle emission branches from ^{11}Li.

of certain decay branches, i.e. their B_{GT}-values [10]. A striking feature would be a peripheral ß-decay of the two-neutron halo in ^{11}Li, resulting in the unbound system ^{9}Li + d shown in fig. 1.7. This decay mode has been searched for in several experiments, and has only recently [11] been unambiguously identified. This is due to the difficulty of discriminating between deuterons and the tritons, also known to be emitted in the decay. However, certain conclusions can be drawn from the shape of the energy spectrum of the Z=1-particles [12] and identification of the activity from the resulting ^{9}Li nuclei.

1.3 Beyond the basics

How can the structure of a halo nucleus be understood? From the beginning, it must be stated that the extended matter distribution is a phenomenon that can be perceived within a quantum mechanical model only. The wavefunction of the halo nucleon(s) is mainly resident beyond the range of the strong force due to tunnelling into the classically forbidden region.

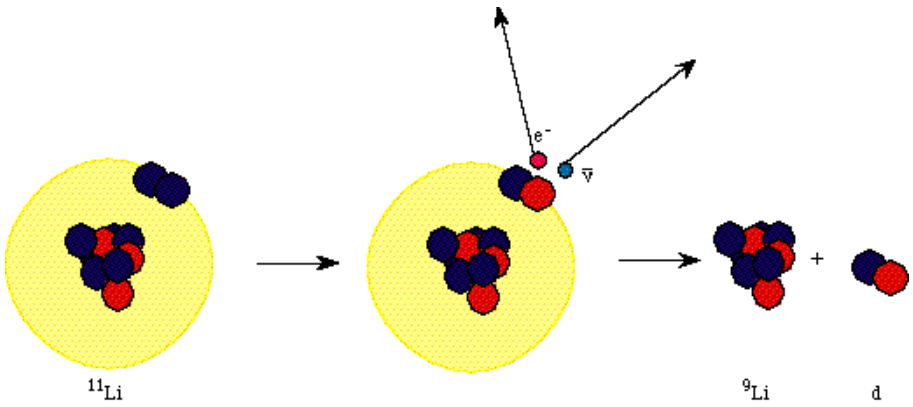

Fig. 1.7. Peripheral ß-decay of a halo neutron in ^{11}Li. The decay leaves the system as an unbound ^{9}Li + d configuration.

ß-delayed particle	Year of discovery
α	1916 [13]
n	1939 [14]
p	1962 [15]
fission	1966 [16]
2n	1979 [17]
3n	1980 [18]
^{6}He	1981 [19]
2p	1984 [20]
t	1984 [21]
4n	1988 [22]
d	1989 [23]
3p	1992 [24]

Table 1.1. Chronological development of the discovery of beta-delayed particle emission. A thorough review is found in ref. [25].

The theoretical attempts made have been based upon a number of methods, the variational approach [3], the cluster-orbital shell model (COSM) [26], the two-particle Green's function method [27], the variational shell model [28], the Fadeev approach and the hyperspherical harmonics method [29]. The details of these calculations are beyond the scope of this work, but some general properties will be quoted.

1.3.1 The deuteron

The simplest possible composite nuclear system is the deuteron, often taken as the first example when introducing the concepts of a nuclear model in undergraduate courses. As a matter of fact, the deuteron can also serve as the first example of a halo nucleus if the distinction used in [30] that approximately at least 50 % of the wavefunction should be outside the nuclear potential is used. A simple calculation, also done in classes of undergraduates, with a square well potential shows that as much as 62 % of the wavefunction resides in the classically forbidden region. This makes the deuteron an ”associate” of the halo family.

1.3.2 Halo and skin

Together with the term *neutron halo*, the concept of a *neutron skin* also exists. In ref. [31], the neutron skin is defined as the radial difference of the neutron and the proton distributions, with thickness $t = R_n - R_z$. The neutron skin then occurs as a consequence of the neutron excess in heavy nuclei. In [32], the term is used to describe the configuration of ^{6,8}He, constituted of an α-particle surrounded by two and four neutrons respectively. Here, the r.m.s. value of the neutron density distribution exceeds the proton density distribution with 0.9 fm. What is then the difference between a neutron halo and a neutron skin nucleus? The distinction is not very clear, but in [32] it is stated that the neutron halo nuclei are characterized by an irregular slope of the radial neutron distribution compared to the neutron skin nuclei.

1.3.3 General conditions for halo states

Fedorov, Jensen and Riisager [33,34] have investigated general properties of loosely bound systems with a short-range attractive potential. Some general conditions for the development of a halo state can be obtained without knowing the details of the potential. The one-neutron halo nuclei are characterized by the difference in position between the core, $\boldsymbol{r}_1$, and the neutron, $\boldsymbol{r}_2$, meaning that $\boldsymbol{r}_{12} = \boldsymbol{r}_1 - \boldsymbol{r}_2$ is the relevant entity. For the two-neutron case the Jacobi coordinates are used;

$$\boldsymbol{x} = \frac{1}{\sqrt{2}}(\boldsymbol{r}_2 - \boldsymbol{r}_3), \boldsymbol{y} = \sqrt{\frac{2A_c}{A}}\left(\frac{\boldsymbol{r}_2 + \boldsymbol{r}_3}{2} - \boldsymbol{r}_1\right) \quad \textbf{(1.3)}$$

The radial variable ρ is defined as $\rho = r_{12}\sqrt{A_c/A}$ and $\rho^2 = x^2 + y^2$ respectively. The total mean-square radius for the nucleus is then given by **(1.4)** for one- and two-neutron halos:

$$\langle r^2\rangle_{tot} = \frac{A_c}{A}\langle r^2\rangle_{core} + \frac{1}{A}\langle \rho^2\rangle \quad \textbf{(1.4)}$$

The Schrödinger equation is then solved with E as binding energy and R_{cn} as the range of the equivalent square-well potential. In the case of a one-neutron halo, the authors obtain the following asymptotic scaling behaviour for the mean-square radius with a neutron in an s-, p- or d-state relative to the core when the binding energy approaches zero;

$$\frac{\langle \rho^2 \rangle}{R_{cn}^2} \cong \begin{cases} 10.44 \text{ MeV fm}^2 / (-ER_{cn}^2) & l = 0 \\ 3.65 \text{ MeV}^{1/2}\text{fm} / (-ER_{cn}^2)^{1/2} & l = 1 \\ 1.40 & l = 2 \end{cases} \quad \textbf{(1.5)}$$

Eq. **(1.5)** shows that, with decreasing binding energy, the mean-square radius diverges for s- and p-states, allowing arbitrarily large values of $\langle \rho^2 \rangle$, but yields a finite result for higher angular momenta.

In the two-neutron halo case, the hypermoment K defined in the hyperspherical harmonics method is a reasonably good quantum number. For a brief description of the method, see e.g. the appendix of ref. [34]. Here, the parameter R_{cn} must be replaced with a weighted average ρ_0 defined by

$$\rho_0^2 = \frac{2}{3}\mu_{cn}R_{cn}^2 + \frac{1}{3}\mu_{nn}R_{nn}^2 \quad \textbf{(1.6)}$$

The asymptotic scaling then becomes

$$\frac{\langle \rho^2 \rangle}{\rho_0^2} \cong \begin{cases} -7\ln(-E\rho_0^2/3 \text{ MeV fm}^2) & K = 0 \\ 9 & K = 1 \\ 3 & K = 2 \end{cases} \quad \textbf{(1.7)}$$

where $K = 0, 1, 2$ corresponds to a system with the two halo neutrons in s-states, in a superposition of s- and p-states and mainly p-states relative to the core respectively. In fig. 1.8 the contribution from the halo neutrons to the total mean-square radius according to **(1.4)** is displayed for $A = 11$ nuclei.

1.3.4 Borromean systems

When investigating the most famous halo system, ^{11}Li, the unbound, resonant nature of ^{10}Li is a key towards detailed understanding. Furthermore, a dineutron is also unbound. It shows that though ^{11}Li is bound, all three possible two-body subsystems are unbound if one constituent is removed, being one of the key properties of a genuine three-body system [29,35]. This is a property also found in the Borromean rings[1], three rings put together in such a way that the two remaining rings are loose if any ring is removed. See figure 1.9.

1. This name originates from the coat-of-arms of the princes of Borromeo, reigning between 1416 and 1884 on four islands in Lago Maggiore, Italy. It displays, among other symbols, three rings coupled together in the fashion described in the text.

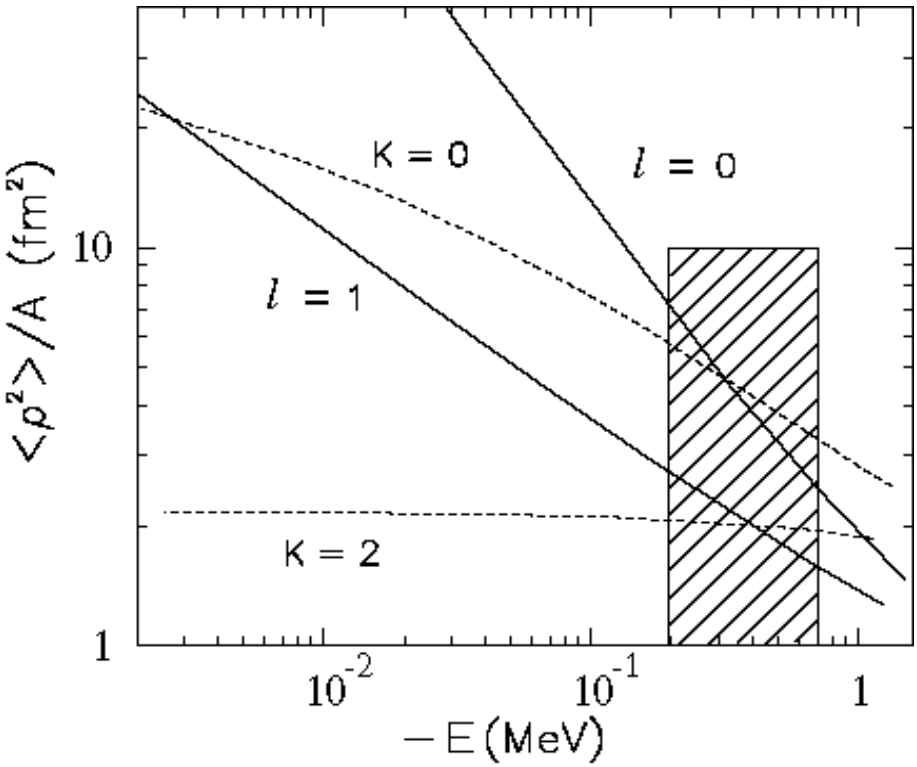

Fig. 1.8. The contribution from the halo neutrons to the total mean-square radius. From ref. [30].

1.4 Increasing knowledge — increasing complexity

1.4.1 Reaction mechanisms — nuclear structure

What happens actually when a neutron halo nucleus with high kinetic energy dissociates in a collision with a target nucleus? The ideal dissociation reaction takes the constituents of the nuclear system apart like a ghost, perturbing nothing. Gradually, the knowledge that this is definitely not the case has become apparent. This is illustrated in fig. 1.16, showing a slight increase of the momentum width with increasing secondary beam energy, a property not stemming from the internal structure of ^{11}Li. A thorough understanding of reaction mechanisms is thus of utmost importance when interpreting the experimental results.

The difference to dissociation of an ordinary nucleus is that we can regard the halo particle(s) as semi-unbound, thus simple diffraction or absorption of a halo neutron can occur. In the case of a two-neutron halo nucleus, several scenarios can take place.

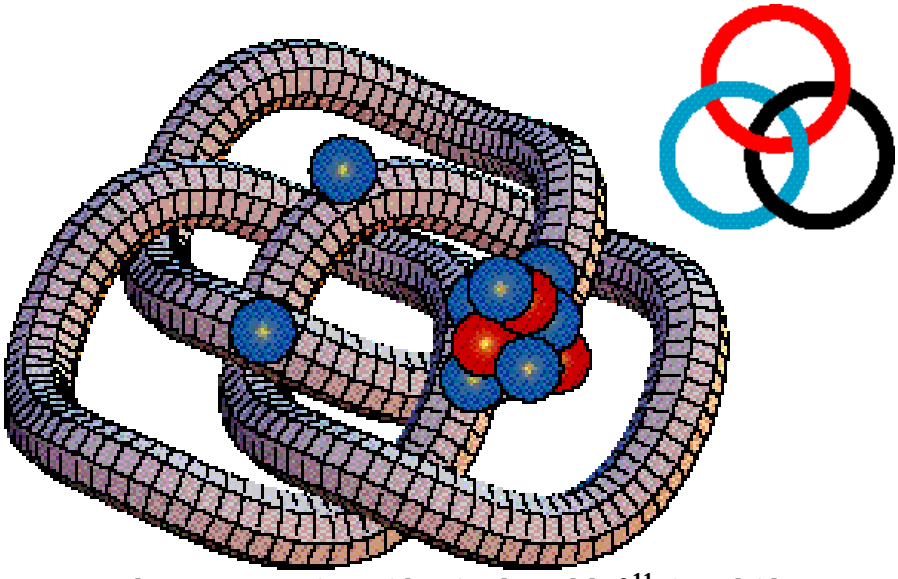

Fig. 1.9. The Borromean rings with a simple model of ^{11}Li overlaid.

1.4.1.1 Diffraction dissociation

A target nucleus can be regarded as an absorbing black disc for an incoming nucleon. In analogy to black-disc diffraction in optics, it is possible to diffract a loosely bound halo neutron. Diffraction dissociation of deuterons was originally treated by Glauber in 1955 [36]. The target nucleus truncates the wavefunction of the halo neutron and the localization following from the volume reduction, if no absorption occurs, leads to an increase of the internal momentum according to **(1.2)**. The projectile nucleus is then in an admixture of the ground state and bound/unbound excited states. For a two-neutron halo nucleus, the diffraction process leaves the core with one remaining neutron, which is unbound. See fig. 1.10. The measured neutron distribution is then a mixture of the diffracted and the remaining neutron, but as the former constitutes a very broad component of the resulting distribution, it might to a large extent lie outside the acceptance and detector coverage of the set-up. The question here is whether we measure the true momentum of the remaining neutron or if final state interactions and/or resonances of the remnants influence the determined momentum distribution.

In the case of a one-neutron halo nucleus, there is not much choice but measuring the diffracted neutron. This makes the one-neutron halo nuclei very good test cases for examining reaction mechanisms, although we might not get much information about the true halo wavefunction by looking at the halo removal channel.

1.4.1.2 Absorption

If a halo neutron is absorbed, the scenario is analogous to the diffraction process with the exception that the absorbed neutron does not contribute to the measured distribution. See fig. 1.11. An absorption process can lead to excitation of the target nucleus and might thus be identified by detection of the subsequent gamma ray emission.

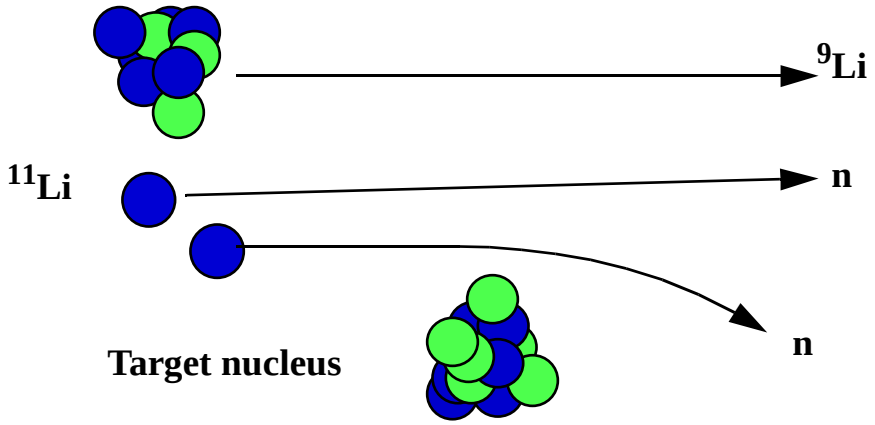

Fig. 1.10. Diffraction of one of the halo neutrons in ^{11}Li.

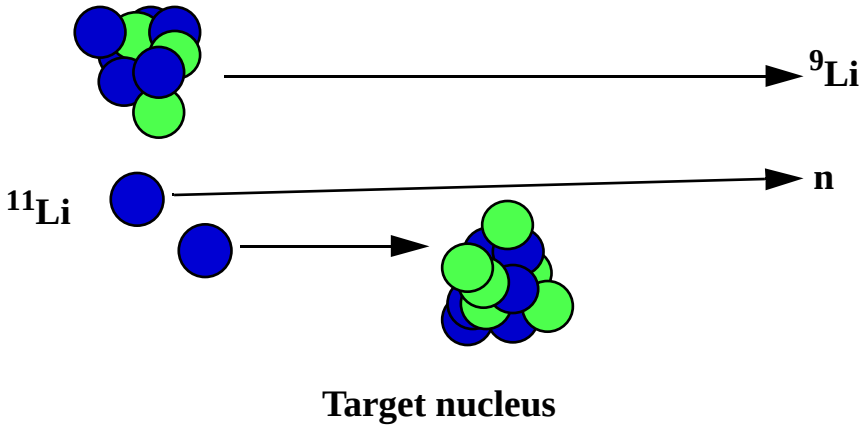

Fig. 1.11. Absorption of one of the halo neutrons in ^{11}Li.

1.4.1.3 Coulomb dissociation

The Coulomb field from a target nucleus can be strong enough to dissociate the incoming nucleus. For a neutron halo nucleus it can be understood as if the core is kicked away from the halo neutrons, like in fig. 1.12. The energy transferred to the incoming nucleus can be calculated with the equivalent photons method [37]. Here, the influence of the Coulomb field upon the incoming nucleus is translated into two virtual photons, one along the beam direction and one perpendicular to it, interacting with the incoming nucleus. See fig. 1.13. The strength of the dominating transverse component of this **virtual photon field** is shown for two different beam energies in fig. 1.13, with the adiabatic cutoff energy, $E_\gamma^{\max} = \gamma\, \hbar c / b$, limiting the maximum photon energy.

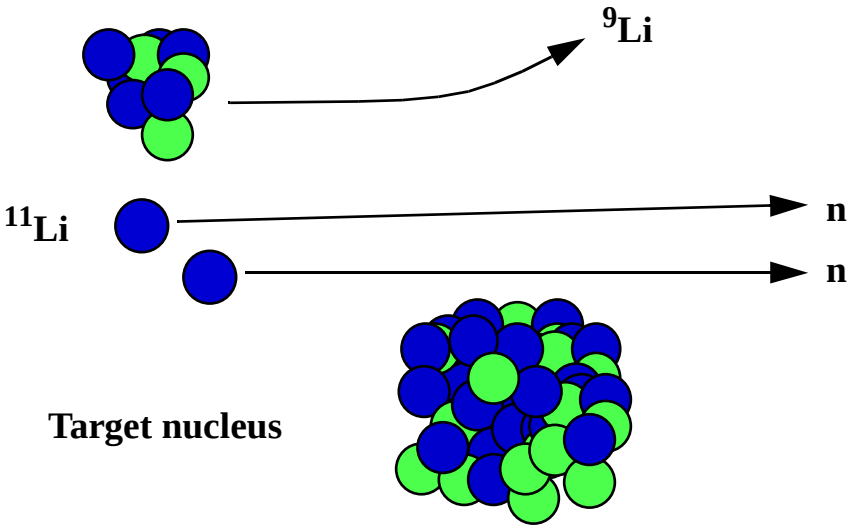

Fig. 1.12. Coulomb dissociation of ^{11}Li.

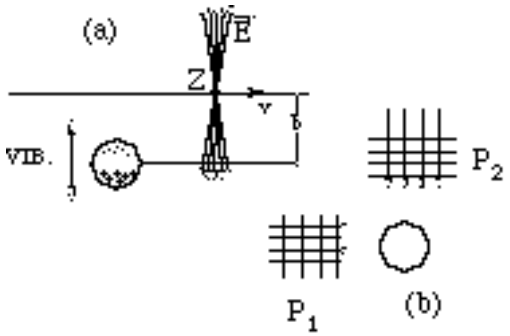

Fig. 1.13. In (a) the influence of the Coulomb field from the target nucleus upon the incoming nucleus (here shown in the reference frame of the latter) is shown. This field can be transformed into two virtual photons, one along the beam direction and one perpendicular to it, shown in (b). From ref. [37].

1.4.2 Longitudinal momentum distributions

All first-generation experiments [6,38] measured angular or momentum distributions of neutrons and charged fragments in the direction perpendicular to the incoming beam. The versatility of the fragment separators FRS [39] at GSI and A1200 [40] at MSU allows for measurements of longitudinal momentum distributions also, by running the instrument in the energy-loss mode. Here the longitudinal momentum spread in the dissociation process, taking place in the middle focal plane, is converted into a spatial spread in the last focal plane of the separator, giving the momentum distribu-

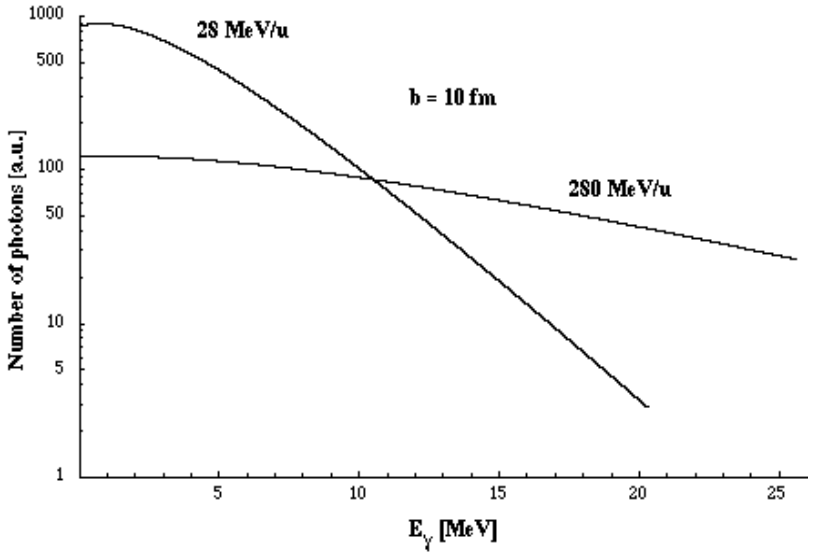

Fig. 1.14. Strength of the virtual photon field for an impact parameter of 10 fm on a Pb target with 28 MeV/u and 280 MeV/u beam energy. The high energy limit correspond to the adiabatic cutoff energy.

tion. See fig. 1.15. Similar experiments are planned at GANIL also, using the α-spectrometer for selection of the wanted isotope and measuring the longitudinal momentum with the SPEG spectrometer [41].

The transverse momentum distributions are distorted by angular straggling which is not the case for the longitudinal momentum distributions. A commonly accepted assumption has been that the longitudinal distributions are less affected by the reaction mechanism, at least for a heavy target, since the Coulomb deflection distorts the measured momentum in the direction perpendicular to the beam only. Thus, measuring the longitudinal momentum with fragment separators adds important information although the method is limited to charged fragments only. However, it has recently been stated [42], exemplified by the case of ^{11}Be, that the reaction mechanism influences the longitudinal momentum distributions significantly, both in the case of nuclear and Coulomb dissociation. Furthermore, the transverse momentum acceptance of the instrument is a parameter which influences the result strongly. This is discussed in section 5.6 and in ref. [43].

1.4.3 Complete kinematics experiments

The first experiments investigating dissociation of halo nuclei did concentrate upon measuring one entity, like the total interaction cross section or the neutron angular distribution. A natural way to proceed was to identify and measure **all** particles involved in the dissociation according to three-dimensional momenta. This was first attempted by Ieki and co-workers [44] at MSU for a 28 MeV/u beam of ^{11}Li on a Pb

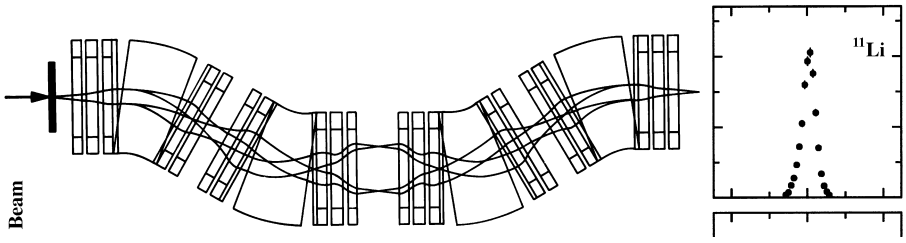

Fig. 1.15. The fragment separator FRS operated in the energy-loss mode. The upper part shows how the ^{11}Li beam is focused achromatically in a single spot, regardless of the angular and momentum spread in the production target. When a secondary reaction target is inserted in the middle focal plane (lower part), a small longitudinal momentum change in the reaction ^{11}Li $\rightarrow$ ^{9}Li + X is translated into a spatial displacement in the final focal plane. From paper III.

target, and has been extended to 43 MeV/u at RIKEN [45]. Papers III-VI stem from a kinematically complete experiment performed at GSI, which is described in detail in section 5.

1.4.4 Neutron-neutron correlations

The simple dineutron + ^{9}Li model used in [2] for describing ^{11}Li was from the beginning regarded as oversimplified. However, the question of an existing correlation, spatial or in momentum space, between the two halo neutrons has been an interesting puzzle since the beginning of the halo adventure. The kinematically complete measurements at 28 MeV/u indicate that there is no strong directional correlation between the two emitted halo neutrons [46]. Nevertheless, the authors of [45] conclude that the measured E1 response is dominated by the relative motion between ^{9}Li and the center-of-mass of the two neutrons, and can be explained within an ”extended dineutron” model.

The relation between the widths of the momentum distributions for neutrons and charged fragments can also yield information about neutron-neutron correlations. In [47], a compilation of the measured neutron and ^{9}Li momentum widths as a function of the beam energy is presented. The width shows a slight increase with increasing energy, but the ratio between the widths remains between 1.3 - 1.5. See fig. 1.16. The authors point out that the absence of an average correlation between the halo neutrons would lead to a relation of $\sqrt{2}$ between the ^{9}Li and neutron average square momentum. In a three-body model with Yukawa-type wave functions, a small anticorrelation

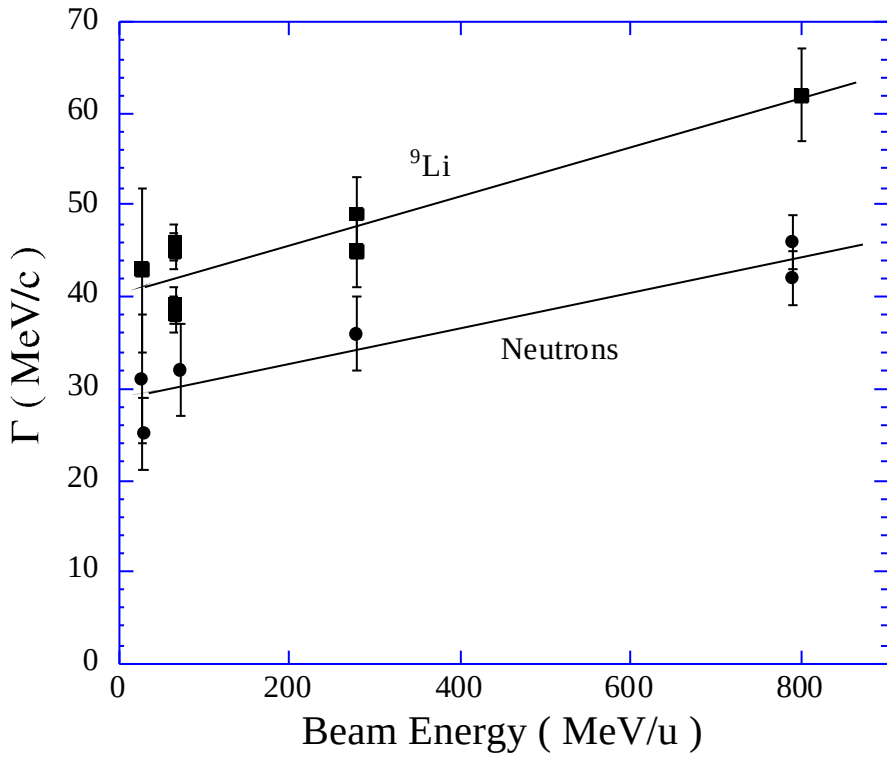

Fig. 1.16. Widths of measured ^{9}Li and neutron momentum distributions expressed in terms of simple Lorentzian Γ-values. From ref. [47].

between the halo neutrons in ^{11}Li is anticipated, in agreement with [46]. Furthermore, the relation between the neutron and ^{9}Li average square momentum is

$$\frac{\langle k_{\mathrm{core}}^2 \rangle}{\langle k_n^2 \rangle} = \frac{2A_{\mathrm{core}}}{A_{\mathrm{core}} + 1}, \tag{1.8}$$

yielding a ratio of 1.8 in the case of ^{11}Li. A value of $\sqrt{1.8}$ is also compatible with the data displayed in fig. 1.16. However, as is stated in [47], to be able to use **(1.8)** for making a comparison between the widths, the momentum distributions must have the same lineshape.

1.4.5 Excited states and unbound resonances

The nature of excited states in halo nuclei has been discussed for several years. An attractive picture has been the one of a soft dipole resonance state, where the core and the halo would vibrate with respect to each other. Such a state would bear resemblance to the GDR (Giant Dipole Resonance) excitations found at high excitation energies where the protons and neutrons vibrate with respect to each other.

It is also very interesting to study unbound systems like ^{10}Li through the decay products in order to understand the nature of the n+^{9}Li interaction in ^{11}Li [48]. This is further discussed in paper V. There are also possibilities to produce resonance structures beyond the drip line, like ^{10}He [49,50,51].

The best data on excitations and resonances stem from nuclear reaction experiments [52,53,54]. A typical reaction is ^{11}B(^{7}Li,^{8}B)^{10}Li for studying ^{10}Li. There is also a possibility to extract the same information by invariant-mass spectroscopy from break-up products, which is done in [55,56] and paper VI. Formula **(1.9)** shows how the ^{11}Li invariant-mass spectrum was constructed from the data obtained in the experiment at GSI (section 5).

$$E(^{9}\mathrm{Li} + \mathrm{n} + \mathrm{n}') = \sqrt{(E_{^{9}\mathrm{Li}} + E_{\mathrm{n}} + E_{\mathrm{n}'})^{2} - (\boldsymbol{p}_{^{9}\mathrm{Li}} + \boldsymbol{p}_{\mathrm{n}} + \boldsymbol{p}_{\mathrm{n}'})^{2}c^{2}} - M_{^{9}\mathrm{Li}}c^{2} - 2M_{\mathrm{n}}c^{2} \quad \textbf{(1.9)}$$

1.4.6 Inverse kinematics experiments

Our picture of the stable nuclei stems to a large extent from proton scattering experiments. Naturally, ordinary scattering experiments with halo nuclei as target are impossible due to the short lifetimes. Instead, the beam and target have to switch places, letting the radioactive beam hit a hydrogen-gas [57] (or hydrogen-rich [58]) target and detect the scattered proton and ion. In [57], the hydrogen gas served as target and detector gas simultaneously, giving the possibility to determine the vertex of the reaction and deduce the four momentum-transfer for elastic scattering of 674 MeV/u ^{8}He. When assuming a matter distribution of an α-core surrounded by four outer neutrons, the data could be well described with $\langle r^2 \rangle^{1/2}_{\mathrm{Core}} = 1.60$ fm and $\langle r^2 \rangle^{1/2}_{\mathrm{Skin}} = 3.20$ fm .

1.4.7 Other reaction channels - core break-up

There have been several attempts to extract the true wavefunction of the halo neutron(s), undistorted by the reaction mechanism. One of the most promising is to look at the core break-up reactions, where the core hits the target nucleus with a small impact parameter and breaks up into smaller fragments. See fig. 1.17. The basic assumption is that the halo neutrons are not necessarily directly involved in the dissociation process and thus they might carry the true internal momentum. This is the idea of paper IV and ref. [59].

The selection of the core break-up channels can be done in different fashions, depending upon the experimental data available. The criteria imposed upon the outgoing charged particles can be $Z_{\mathrm{in}} > Z_{\mathrm{out}}$, $\neq {}^{A}_{Z'}\mathrm{Core}$ or selection of one specific nuclide. The measured neutron distributions have a slight admixture of neutrons stemming from the core, but here the widths are considerably larger.

Very clean information can be gained by looking at the reaction channel where only a proton is stripped from the core. Here there is no uncertainty about the halo neutron being detected. This will be further discussed in 6.5.1.

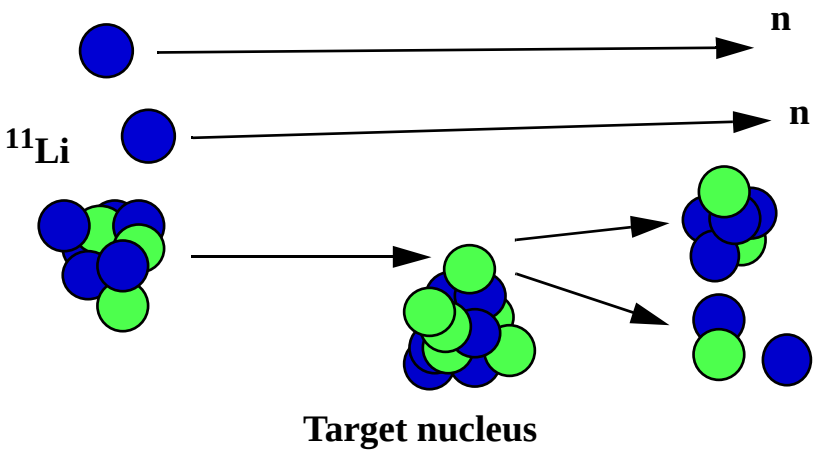

Fig. 1.17. Core break-up of ^{11}Li.

1.4.8 Complete studies of ß-decay properties

The perfect experimental set-up for decay studies of halo nuclei is a virtual impossibility since it involves detecting and distinguishing between a multitude of charged particles down to low energies, neutrons with a large range of energy and gamma rays, all in coincidence with high efficiency and solid angle coverage together with real-time information in order to identify decay chains through subsequent daughter activity.

One attempt has been made to accomplish this for the decay of ^{11}Li, at least regarding the type of detection equipment involved [11,60], but to get the true picture of the complete decay is very complicated as can be understood from fig. 1.6.

Increasing knowledge — increasing complexity

2. Experiments with halo nuclei

Nuclear reaction experiments and decay studies with extremely neutron-rich nuclei do not differ much from general nuclear physics experiments. However, some facts must be kept in mind;

- The nuclei are often extremely short-lived and must be studied immediately after production.
- Beam intensities are several orders of magnitude lower than when using stable beams. This is to some extent compensated by the large reaction cross sections exhibited by these nuclei, often several barns.

2.1 Interaction between radiation and matter

The trivial criterion for detecting radiation is that an interaction with the detector takes place. In order to understand the operation of any detector and also the methods used for isotope separation, the interaction between radiation and matter must be considered.

2.1.1 Charged particles

2.1.1.1 Energy loss

The energy loss of an energetic particle passing through matter stems from the Coulomb interaction with the atomic electrons and is governed by the Bethe-Bloch formula:

$$-\frac{dE}{dx} = 2\pi N_a r_e^2 m_e c^2 \rho \frac{Z}{A}\frac{z^2}{\beta^2}\left[ln\left(\frac{2m_e\gamma^2 v^2 W_{max}}{I^2} \right) - 2\beta^2 + \delta - \frac{2C}{Z} \right] \quad \textbf{(2.1)}$$

with

$2\pi N_a r_e^2 m_e c^2 = 0.1535$ MeV cm^2/g

z - charge of incident particle

Z - charge of absorber

ρ - density of absorber

v - velocity of incident particle

I - mean excitation potential

δ - density correction

C - shell correction

W_{max} - maximum energy transfer between the incoming particle and an atomic electron

$\beta = v/c$

$\gamma = 1/(\sqrt{1-\beta^2})$

The formula **(2.1)** is valid for all charged particles, but in the case of electrons some additional corrections must be made due to the interchangeability of the incoming and atomic electrons.

2.1.1.2 Energy straggling

The energy loss of a charged particle in matter according to **(2.1)** is a process of statistical nature and does not take an exact value but varies somewhat. This spread in the energy loss is called energy straggling and is described by (from ref. [61]):

$$\sigma^2(E_f) = \left[\frac{dE}{dx}(E_f)\right]^2 \int_{E_f}^{E_i} \frac{\frac{d}{dx}\sigma^2(E)}{\left[\frac{dE}{dx}(E)\right]^3} dE \qquad \textbf{(2.2)}$$

where

$$\sigma^2(E) = \frac{N\Delta x z^2 Z e^4}{4\pi\varepsilon_0^2} \frac{1-\frac{\beta^2}{2}}{1-\beta^2}. \qquad \textbf{(2.3)}$$

E_i and E_f are the initial and final energies of the charged particles when passing the slice of matter and N is the number of atoms per unit volume.

2.1.1.3 Multiple angular scattering

Similar to the energy straggling, the statistical nature of the Coulomb interaction yields an angular deviation from the original direction of the incoming ion. For small angles and thin slices of matter, a Gaussian approximation can be used although it underestimates the large-angle scattering probability. A reasonable approximation for the angular distribution $W(\theta)$, where θ denotes the scattering angle, according to [62] is then:

$$W(\theta) = \frac{1}{2\pi\theta_0^2} \exp\left(-\frac{\theta^2}{2\theta_0^2}\right) \qquad \textbf{(2.4)}$$

where

$$\theta_0 = \frac{13.6\ \text{MeV/c}}{p\beta} Z_{\text{inc}} \sqrt{L/L_R}\,[1 + 0.038\ \ln(L/L_R)]\ \text{(rad)} \qquad \textbf{(2.5)}$$

p - momentum of incident particle in MeV/c

Z_{inc} - charge of incident particle

L/L_R - thickness of the scattering medium expressed in units of radiation lengths

2.1.2 Neutrons

Neutrons possess no electric charge. This trivial fact makes the interaction of neutrons with matter an improbable process since the atomic electrons, making up the size of the atom, can be completely disregarded. Instead, the neutrons interact with the nuclei only, through the short-range strong interaction. The art of interaction process is strongly energy dependent;

i. Radiative neutron capture ($\text{n} + (Z,A) \Rightarrow \gamma + (Z,A+1)$) where the cross section approximately varies as $\sim 1/v$, possibly with resonance peaks superimposed at certain energies.

ii. Neutron capture reactions with charged particle emission such as (n,p), (n,d), (n,α) etc.usually occur for neutrons in the eV to keV energy region. The general dependence of the cross section is also here $\sim 1/v$ with possible resonance additions.

iii. Fission, (n,f), also preferably takes place at thermal energies.

iv. Elastic scattering from nuclei, $A(\text{n,n})A$, dominates in the MeV region.

v. Inelastic scattering, $A(\text{n,n'})A^*$, $A(\text{n,2n'})B$ etc. Here the incoming neutron must have enough energy to excite the nucleus, otherwise only elastic scattering can occur. This threshold is usually in the order of 1 MeV.

vi. Hadronic shower production, taking place only for very high energy neutrons, $E > 100$ MeV.

Neutrons of more than 1 MeV energy are normally scattered elastically or inelastically against the ”target” nucleus, producing energetic recoil ions. In the case of protons (hydrogen), only elastic scattering occurs. The neutron energy E after an elastic scattering process against a nucleus with mass A is given by

$$\left(\frac{A-1}{A+1}\right)^2 E_0 < E < E_0 \qquad \textbf{(2.6)}$$

If $A = 1$ is inserted into eq. **(2.6)**, the lower limit for the energy of the scattered neutron becomes zero, meaning that the maximum possible energy transferred to the proton is E_0. The energy of the scattered neutron exhibits a strong angular dependency:

$$\begin{aligned} E &= E_0 \cos^2\theta_L \\ 0 &\le \theta_L \le 90° \end{aligned} \qquad \textbf{(2.7)}$$

2.2 Beam production

There are several production methods of radioactive nuclei, but all of them involve the process of accelerating stable nuclei and smash them into a reaction target. The main divider here is if the nuclei of interest are remnants of the primary beam or of the target nuclei. All existing facilities for production of radioactive nuclei work according to these principles, in the following the facilities FRS at GSI, LISE-3 at GANIL and ISOLDE at CERN will be used as examples if not otherwise stated. A recent and thorough review of the fine art of producing and separating radioactive nuclei is found in ref. [63].

2.2.1 Fragmentation of the primary beam

At the facilities LISE-3 and FRS the primary beam hits a beryllium target. A typical stable primary beam is ^{18}O which can yield neutron drip-line nuclei up to ^{14}Be by projectile fragmentation.

Fission reactions have proven to be useful for production of neutron-rich nuclei in the medium mass region. In ref. [64], more than 40 new, neutron-rich nuclides were produced in one single experiment at FRS by fission of 750 MeV/u ^{238}U projectiles impinging on a lead target.

2.2.2 Target fragmentation, fission and spallation

At ISOLDE-PSB, which is a typical so-called ISOL-type facility, the primary beam is a pulsed proton beam, from the PS Booster, with an energy of 1 GeV. The beam hits a thick target consisting of a material appropriate for production of the nuclide of interest, in a chemical compound suitable for rapid diffusion of the created radioactivity. When producing light neutron-rich nuclei, the production is enhanced by the natural neutron excess of the heavy target nuclei. The energy of the production beam at ISOLDE-PSB is well chosen for producing a wide range of isotopes, some examples of the energy dependence of the production yields are given in fig. 2.1.

2.3 Separation of the nuclides

2.3.1 Fragment separators

The fragment separators LISE-3 [66] and FRS [39] both operate in a similar fashion. Fig. 2.2 gives a schematic view of the latter instrument. A first selection according to magnetic rigidity **(2.8)** is made via a dipole magnet stage.

Separation of the nuclides

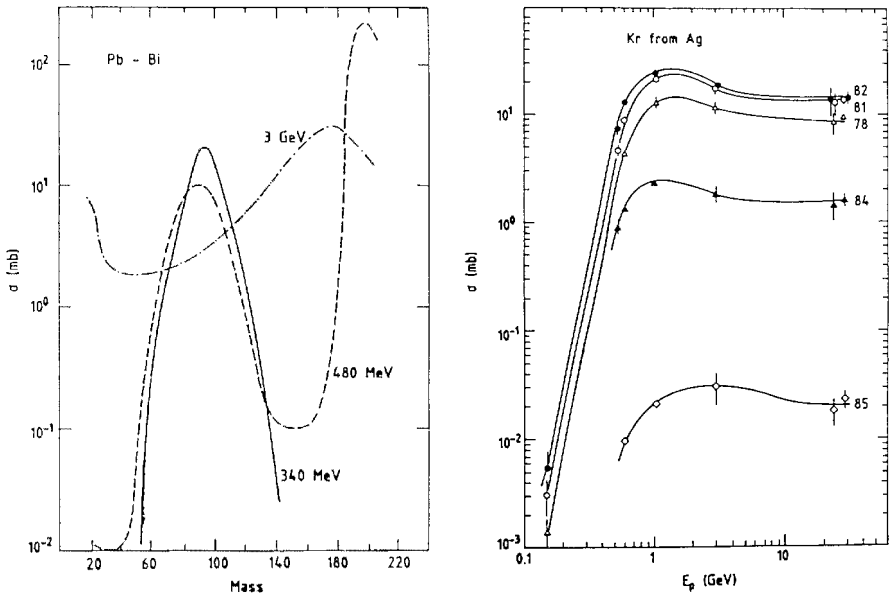

Fig. 2.1. Spallation/fragmentation yields for various proton energies. The cross-section for production of light nuclides rises dramatically with increasing energy. From ref. [65].

$$B\rho = \frac{p}{Z300}\,(\mathrm{Tm}) \qquad \textbf{(2.8)}$$

where

- $B\rho$ - magnetic rigidity (in Tm)
- p - total momentum of the ion (in MeV/c)
- Z - charge of the ion

As all secondary ions are created with roughly the same velocity, the selection practically is made in the A/Z-ratio. The ions then pass a piece of material, a degrader, where they loose energy according to the Bethe-Bloch formula **(2.1)**. A second separation is obtained according to the charge of the ion and in a subsequent dipole magnet stage, a final selection of the wanted species is made. In the dispersive focal plane, where the degrader is situated, a spatial splitting occurs due to the momentum width. With a wedge-shaped degrader it is possible to adjust the energy loss so that the momentum distribution afterwards fits with the spatial separation corresponding to the second selection, i.e. the separator is run in an achromatic mode as indicated by the envelopes in fig. 2.2.

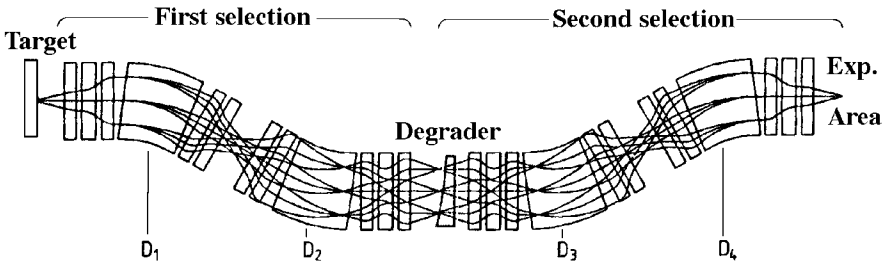

Fig. 2.2. View of the fragment separator FRS at GSI. Via the dipole magnets and the degrader, a $B\rho-\Delta E-B\rho$ isotope selection is possible. From ref. [39].

2.3.2 On-line separators

The layout of the ISOLDE-PSB facility is shown in fig. 2.3, exemplifying this kind of separator. The nuclei produced by target fragmentation are usually created as neutral atoms inside the target matrix. This presents us with a twofold problem; firstly the atoms must diffuse out of the target, secondly they must be ionized in order to enable transport to the experimental set-up. Furthermore, this is the main limitation to the shortest lifetimes allowed for studies, so the procedure must be swift. Thus, the production target is usually heated in order to enhance the diffusion speed. When isotopes of noble gases are desired, a good chemical separation can be yielded by using a cooled transfer line.

Fig. 2.3. Overview of the ISOLDE-PSB facility.

2.3.2.1 Ion sources

The process of ionizing the created radioactivity can be completed in a number of ways. In ref. [67], the plasma-discharge, FEBIAD-type, ECR (electron cyclotron resonance), surface-ionization and laser ion sources are discussed. The correct choice of target – ion source combination is crucial for reaching good production yields. When using a laser ion source, a very good selectivity can be reached by a two-step excitation and subsequent ionization where the energy of the first laser is tuned to an atomic transition in the wanted nuclei.

2.3.2.2 Beam transport and mass separation

After ionization, the ions are accelerated to 60 keV, an energy range where the bending element in the beam transport can be of the electrostatic type, meaning that the bending depends upon the charge of the ion only. The mass separation is made with a doubly–focusing 70° dipole magnet with $M/\Delta M = 2400$ (the GPS, General Purpose Separator) or two magnets with bending angles of 90° and 60° respectively, yielding a resolution of $M/\Delta M = 30000$ (the HRS, High Resolution Separator). The separated nuclei can then be transported to a multitude of experimental stations, as shown in fig. 2.3.

2.4 Detectors

2.4.1 Charged particle detectors

Charged particles are relatively easy to detect. When traversing matter, they loose energy according to eq. **(2.1)** by interacting with the atomic electrons. If by some means it is possible to measure the energy that is transferred to the electrons, information of the energy deposited in the detector is yielded.

2.4.1.1 Energy sensitive detectors

The different types of charged particle detectors used can be divided into three main groups according to the detector material and physical processes involved;

i. Semiconductor detectors, where the incoming particle creates electron-hole pairs when energy is transferred to the material. By applying an external voltage, a charge pulse is obtained.

ii. Gas detectors, where the gas is ionized by the incoming particle. By applying a non-linear electric field to the gas volume, a substantial **secondary ionization** can be achieved. If the detector works in the proportionality region, the secondary ionization is proportional to the primary, and thus the pulse read out is directly related to the energy deposited in the gas volume.

iii. Scintillators, where the molecules in the detector material get excited by the incoming particle and subsequently emit light. The light output is converted and magnified in a photomultiplier tube.

2.4.1.2 Telescope detectors

A detector telescope consists of two subdetectors. The incoming charged particles should pass through the first detector and get completely stopped in the second. The amount of energy lost in the first detector, the so-called ΔE-detector, is given by eq. **(2.1)** which can be simplified as

$$-\frac{dE}{dx} = z^2 f(\beta) \tag{2.9}$$

where $f(\beta) \propto 1/\beta$ for energies exceeding 5 MeV/u. If the energy loss is plotted as a function of the energy detected in the second detector (ΔE-E plot), a plot similar to the one shown in fig. 2.4 is obtained. Thus, an identification according to charge can be made. If the resolution in the ΔE-detector is good, an identification of the mass can also be made due to the shift in velocity for the same total energy for the different isotopes. The energy-loss curve is then shifted horizontally in the ΔE-E plot.

2.4.1.3 Position sensitive detectors

A solid state detector can easily be made position sensitive by segmenting the active volume into smaller regions. The resolution is then depending upon the granularity of the detector. One main problem is the read-out procedure of such a detector. If every pixel has its own read-out electronics, the cost for a large-area, high-granularity detector soon reaches impossible amounts. This can partly be avoided by a sequential read out, but this limits the data rate. Examples of such detectors are silicon-strip and microstrip detectors.

A scintillator can be used as a position sensitive detector if more than one photomultiplier tube is connected to the scintillating material. One method is to read out the light pulses at both ends of a scintillator paddle and deduce the position from the time difference between the two pulses. The light attenuation in the scintillator can also be used if the material is thin enough to exhibit a considerable intensity loss along the extension of the detector. Here, the position is inferred from the relative strength of the light pulses in the photomultipliers.

Position-sensitive wire chambers can be used for many purposes. Originally developed by Charpak and collaborators [68], they are now a widely used tool in many subatomic physics experiments. In the Multi-Wire Proportional Chamber (MWPC), alternating anode and cathode wires are mounted repeatedly inside a gas volume. When a charged particle traverses the detector, the gas is ionized along the track. The electrons drift towards the anode wire where a secondary ionization takes place. The spatial resolution of the MWPC is thus defined by the distance between the anode wires.

Another method is to register the time required for the electrons to drift from the ionization track to the anode wire. This is done in the so-called Multi-Wire Drift Chambers (MWDCs). Ideally, the electrons reach a constant drift velocity within a very short distance and a linear relation between drift time and distance between the ion track and the nearest wire. Only in the very close vicinity of the anode wire, a non-lin-

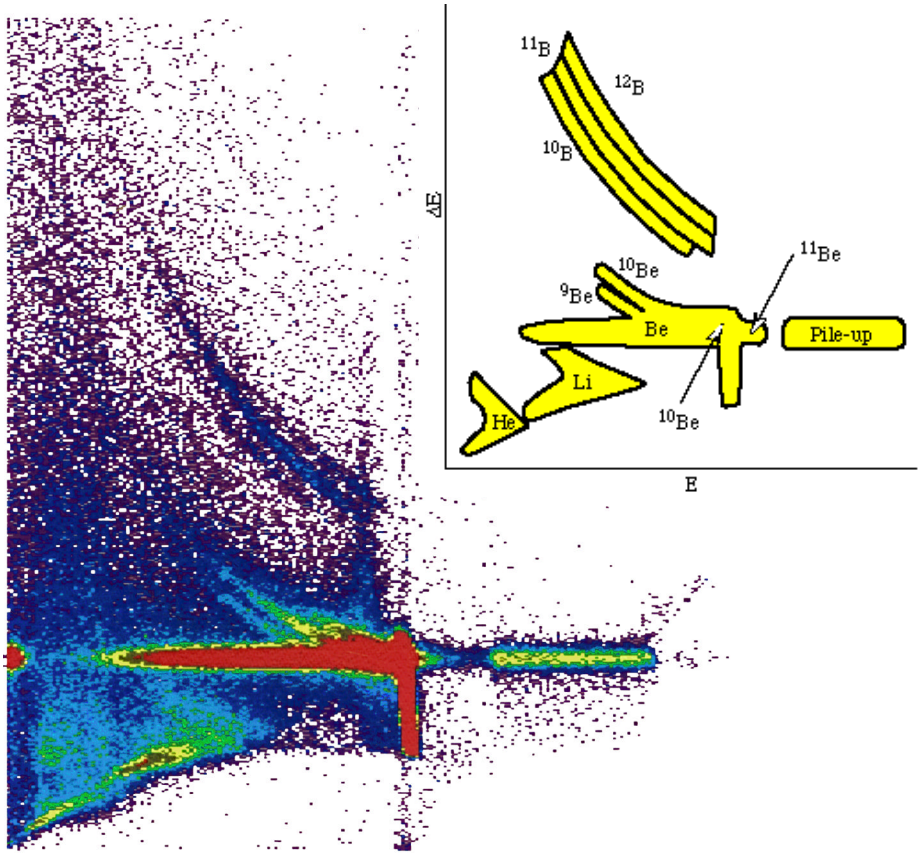

Fig. 2.4. ΔE-E-plot, in coincidence with neutrons, from a silicon-detector telescope where an incoming beam of ^{11}Be breaks up on a Be-target. See the inset for explanation of the different parts. The thickness of the E-detector was not sufficient to stop all Li- and He-isotopes, leading to the "punch-through" behaviour seen in the figure. The data stem from the experiment performed at GANIL described in ref. [59,77].

ear second ionization gives an electron avalanche. This method demands an external time reference to determine the drift time.

2.4.2 Neutron detectors

Neutrons are troublesome to detect. As mentioned in section 2.1.2, they interact via the strong nuclear force only. This means that a neutron detector must detect the secondary charged particles from a strong interaction process. Furthermore, there is no reliable way of getting the total energy of the neutron by studying the energy deposited inside the detector as the energy varies strongly with the scattering angle. Thus, time-of-flight methods normally have to be used.

2.4.2.1 ^{3}He-filled proportional counters

Low-energy neutrons can be detected in ^{3}He-filled proportional counters. The geometry of such a detector is the one of a classical proportional counter, with cylindrical cross section and a single anode wire in the middle. The incoming neutrons react with

the ^{3}He by the reaction ^{3}He(n,p)^{3}H which has a Q-value of 764 keV. The kinetic energy of the reaction products is transferred to the gas by ionization and the energy released in the detector thus corresponds to the energy of the incoming neutron plus 764 keV. However, the cross section for this reaction is strongly energy dependent, limiting the usage to low-energy (< 3 MeV) neutrons only.

2.4.2.2 Scintillator s

As seen in section 2.1.2, the mean energy transferred to the ”target” nucleus by a neutron in an elastic collision is maximal for scattering against protons. In order to increase the probability of exceeding the threshold in the read-out electronics for a given neutron energy, all efficient neutron detectors must thus have a high hydrogen content. All organic scintillators have this property, with the additional advantages of good timing properties and easy handling.

A scintillator detector used for detecting neutrons can naturally be used as a position-sensitive detector using the same timing method as described in section 2.4.1.3.

2.4.2.3 Pulse-shape discrimination

Several organic liquid scintillators can be used for discriminating between incident neutrons and gamma rays. This is done by exploiting the different processes involved when neutrons and gamma rays interact with matter. Gamma rays, on the contrary to neutrons, interact with the atomic electrons in the detector material preferably via Compton scattering. In scintillator materials capable of pulse-shape discrimination, the slowing-down processes of protons (from neutrons) and electrons (from gamma rays) populate molecular singlet and triplet states with dissimilar lifetimes in different proportions. As the excited states de-excite by emission of light, the time dependence of the intensity will vary with the relation between the long-lived and short-lived states. Thus, the pulse shape of the integrated light output will be different for an incoming neutron and a gamma ray.

In fig. 2.5, one method of exploiting the pulse-shape discrimination is shown. The energy signal is fed into a QDC (charge-to-digital converter) and is analysed using two different gate pulses. The gate pulse labelled ”Prompt” in the figure covers the energy pulse from the peak onset, while the pulse labelled ”Delayed” means an integration covering the tail of the pulse. As can be seen, this method yields a very good separation between neutrons and gamma rays.

Another method is to use a zero-crossing discrimination. Here the time between the leading edge of the pulse and the zero-crossing of a doubly differentiated version of the incoming pulse [69]. This method might work at lower energies than the charge comparison method discussed above [70].

Pulse shape discrimination is not only used in the context of neutron detectors. Inorganic crystal scintillators such as for example CsI(Tl) have a light output consisting of fast and slow components, with proportions depending on the ionization density. The pulse shape characteristics can thus be used for discriminating between α-particles,

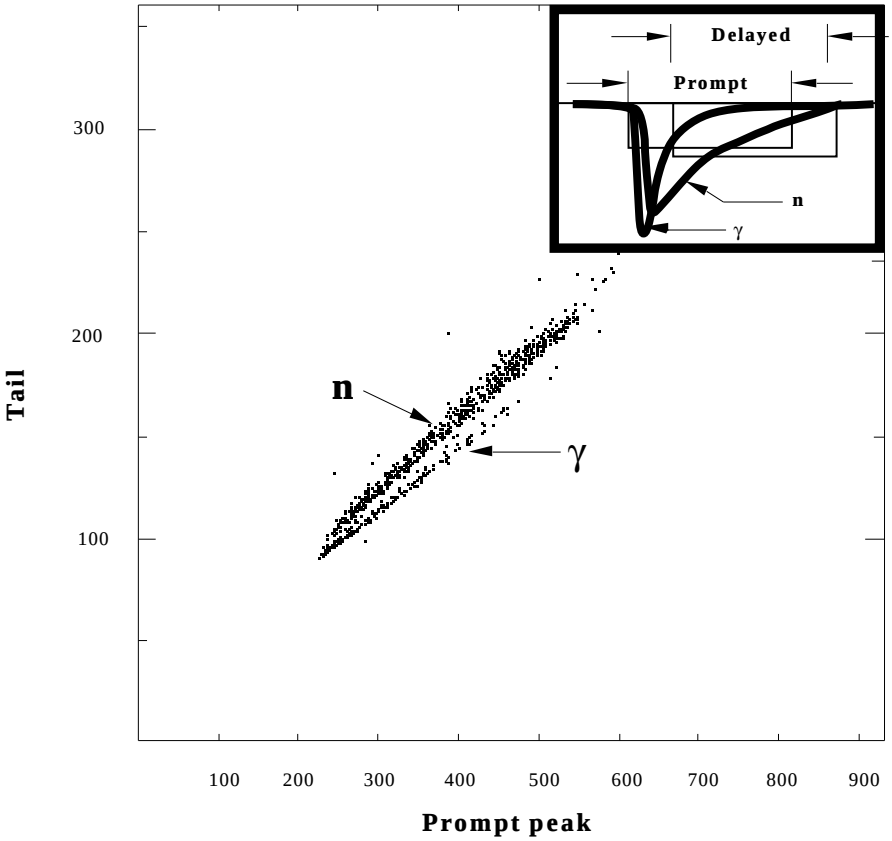

Fig. 2.5. Two-dimensional plot used for pulse-shape discrimination analysis showing the distributions connected with neutrons and gamma rays. The neutron events can easily be selected by a polygon condition. The inset shows a schematic picture how the QDC is gated to obtain the separation plot. From paper I.

protons, deuterons, tritons and electrons. Even silicon detectors can exhibit a limited Z-resolution for high energy heavy ions by means of pulse shape analysis [71].

2.4.2.4 Cross-talk

When an array of neutron detectors is used for measuring neutron-neutron coincidences, some coincidences might erroneously stem from cross-talk events. This means that a neutron hits one detector, gets scattered elastically and subsequently hits a second detector, giving an alleged neutron-neutron coincidence. Especially, if the true coincidence probability is low, the cross-talk effects might be a large problem. By comparing the energy deposited in the two detectors with the time-of-flight and applying the limits for energy transfer given by eq. **(2.7)**, a set of neutron-neutron coincidences not stemming from cross-talk can be singled out, but the acceptance correction then becomes very complicated and might bias the result. The most straightforward way to manage this problem is to have knowledge, from experiments or simulations,

of the probability for cross-talk with the current set-up and apply the appropriate corrections. Experimental measurements of cross-talk probabilities are discussed further in section 3 and paper I.

2.4.2.5 Detecting high energy neutrons

For highly energetic neutrons, the efficiency of a hydrogen-rich scintillator material is low. Instead, a hybrid construction can be used where the neutrons interact strongly with a converter material, causing hadronic showers which subsequently can be detected in a traditional scintillator. The detector LAND [72] at GSI function along these lines and is described in some detail in section 5.4.2.

2.5 Data acquisition and analysis tools

No chain is stronger than its weakest link. The best designed experiment will not be of any good if the possibilities of collecting and analysing the measured data are limited. On the contrary, a good analysis can squeeze interesting results out of an ill-planned experiment. A multitude of data acquisition and analysis methods exists and here only those will be reviewed that have been in use during this work.

2.5.1 Acquisition systems

Almost every experiment within subatomic physics today is based upon collecting coincident data event-by-event and saving it on data media as a LMD (List Mode Dump)-file. This allows the experimenters to ”replay” the experiment afterwards, putting conditions upon the various variables etc.

2.5.1.1 Hardware

The art of data-acquisition electronics will not be referred to in detail here. It will only be mentioned that the data were collected with a J11-CAMAC system (Papers I-II) and a VME-based system combining CAMAC and Fastbus (via Aleph Event Builder) electronics (Papers III-VI). In the latter case, a trigger pattern box was used which allowed for a multitude of trigger conditions with individual scale-down factors. The complexity of a typical acquisition set-up is illustrated in fig. 2.6, with the electronics demanded for TOF and pulse-shape discrimination in an experiment with 35 neutron detectors.

2.5.1.2 Software

The existence of a local, unique acquisition system seems to be a pride of every laboratory, with few exceptions. The task of the acquisition software is to write the data on media for off-line analysis and to provide the experimenters with on-line information about the running experiment. This work was made using the GSI-developed GOOSY (**G**SI **O**n-line **O**ff-line **SY**stem) [73] in papers I-II and TDAS (Temporary Data Acquisition System) [74] in papers III-VI.

There were several important differences in the mode of operation between these systems. The GOOSY on-line analysis is limited to sorting the incoming data into a

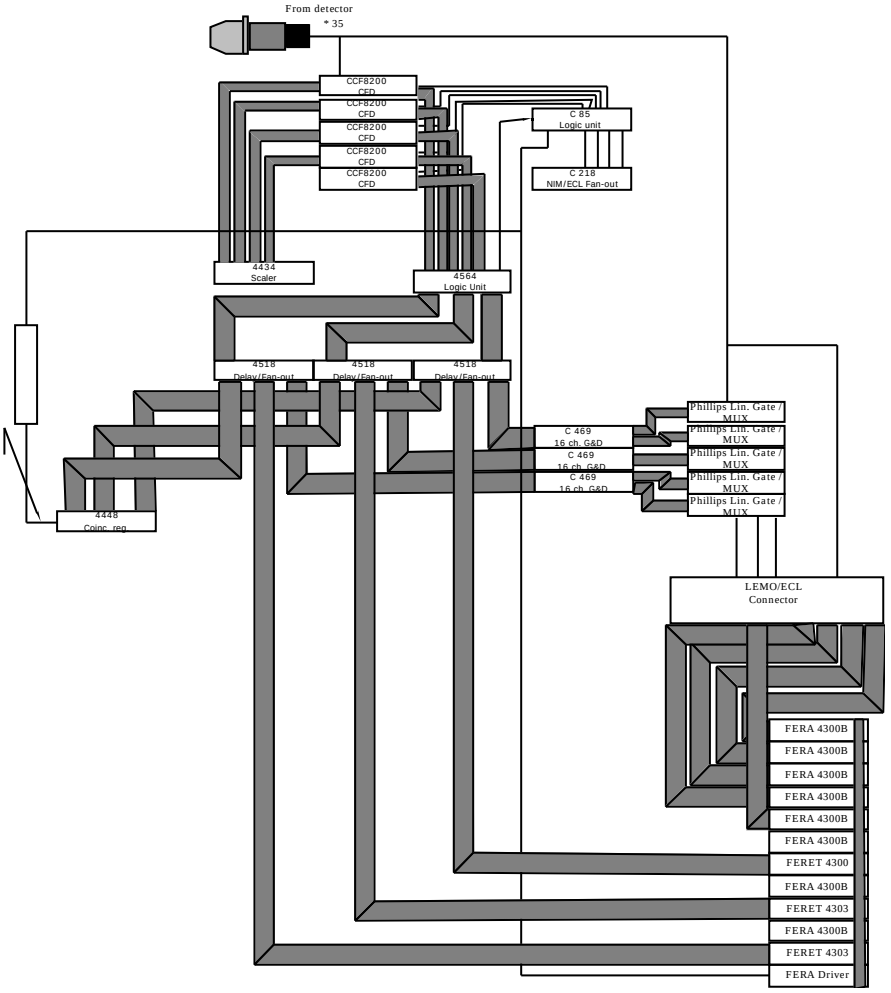

Fig. 2.6. Data acquisition electronics set-up with 35 neutron detectors, permitting TOF measurements together with pulse-shape discrimination.

number of predefined one- or two-dimensional histograms. Especially the number of two-dimensional histograms often gets limited by computer memory. The sorting procedure is made beforehand and sorts the data continuously, and the histograms with their accumulated content can be viewed at any time.

The function of the TDAS system is more complicated. To begin with, a data file (n-tuple) for the analysis system PAW is created with the incoming data, with run-time calibrations and derived entities. After closure, this file can then be opened inside PAW and the full analysis power of the program is available. The n-tuple is a list-mode-like data representation which can be resident in the RAM-memory or as a disc-file.

The preferred method is very much depending upon the size of the experiment. In the experiments at ISOLDE, the number of parameters is usually limited and it is possible to construct two-dimensional histograms for all interesting combinations. The continuous accumulation of data is also helpful in low-countrate situations. For the set-up used at GSI, described in section 5.4, the number of combinations of two parameters that might show relevant correlations exceeded the available memory by orders of magnitude. Here the nuisance of the tedious procedure of collecting data for subsequent on-line analysis, all during the experiment, was well compensated by the useful and, now and then, surprising information extracted. This led to several improvements of the experimental set-up during the run. The complexity of many experiments, with a intricate relation between the measured and the physically interesting variables, call for an advanced primary analysis while the experiment is still running, as the risk of running blindfold is substantial. This has e.g. been applied during a recent experiment at GANIL [75], where the data was copied from the set-up-specific on-line acquisition system in order to make a more elaborate on-line analysis using PAW.

2.5.2 Analysis tools

The experimental subatomic physicist spends a lot of time trying to understand experimental data. Good analysis tools can be invaluable in finding expected, and perhaps more important, unexpected effects. The ideal analysis system allows the physicist to swiftly explore every aspect of the measured data with a minimum of effort. In reality, most of the time is used for tedious typing of illogical syntax, waiting for slow CPUs and hard disks (the definition of slow is rapidly changing, naturally) to complete their tasks and fighting a constant lack of disk space.

2.5.2.1 Computer s

Traditionally, Digital VMS-based computers have been very frequently used among experimental subatomic physicists, although UNIX-based systems are getting more and more common. Today, most data analysis is made using workstations with large colour monitors and local data discs with several GByte capacity. The data analysis in this work has been performed using a VAXstation 4000/90 with 3.2 GByte disc capacity and the AXP workstations DECstation 3000/70 and Alphastation 200/166 with 7 GByte and 5 GByte respectively.

2.5.2.2 Software

The GOOSY system can be used for off-line analysis as well as on-line, directing the data input from the data media instead of the acquisition hardware. This offers the advantage of using the same analysis program, but this can also be a limitation.

PAW (Physics Analysis Workstation) [76] is an analysis package that has been developed at CERN. In its latest and most advanced form, PAW++, it is attempting at being the universal tool for multi-parameter data analysis. The very powerful concept of the n-tuple allows for on-line plotting of all parameters and combinations of parameters including mathematical expressions from one to four dimensions.

3. Experimental studies of cross-talk

3.1 Background

3.1.1 Physics motivation

As mentioned in section 2.4.2.4, cross-talk events can confuse a measurement of neutrons by emulating false neutron-neutron coincidences. The neutron detector arrays used in experiments at GANIL, reported in [6,59,77] had a geometry which might be sensitive to cross-talk, and the probability for this was investigated by using the Monte-Carlo code Menate [78]. The detectors are described in detail in [79].

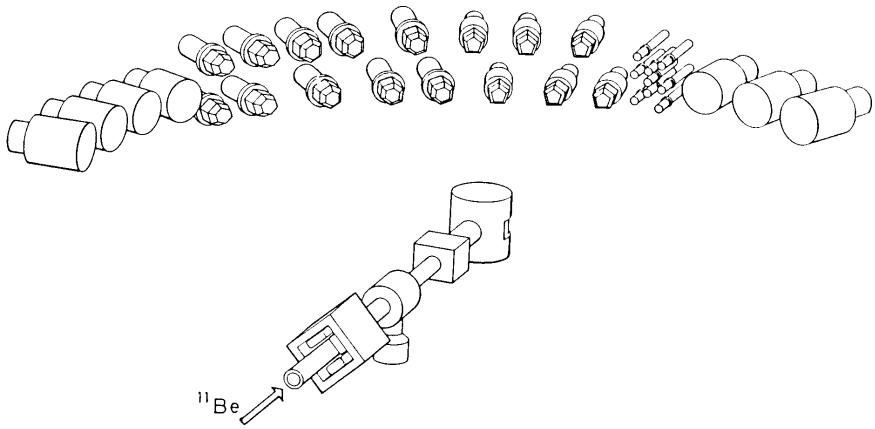

Fig. 3.1. The neutron detector set-up used in [59,77]. The central array contained detectors mounted close to each other and thus sensitive to cross-talk. From ref. [77].

In order to verify the results from the calculation, the cross-talk probability was also determined experimentally using monoenergetic neutrons from the neutron generator at the department of Reactor Physics at Chalmers University of Technology, Göteborg.

3.1.2 Experimental facility

The neutron generator at the department of Reactor Physics has proven to be most suitable for detector tests. The facility is shown in fig. 3.2. The neutrons are produced by accelerating a deuteron beam which hits a target composed of a tritium-loaded Ti-foil where a t(d,n)α fusion reaction takes place. The neutron energy is slightly depending of the direction of the outgoing neutron, but in the plane perpendicular to the incoming beam the energy is 14.1 MeV. The neutron flux was isotropic in the plane perpendicular to the beam axis.

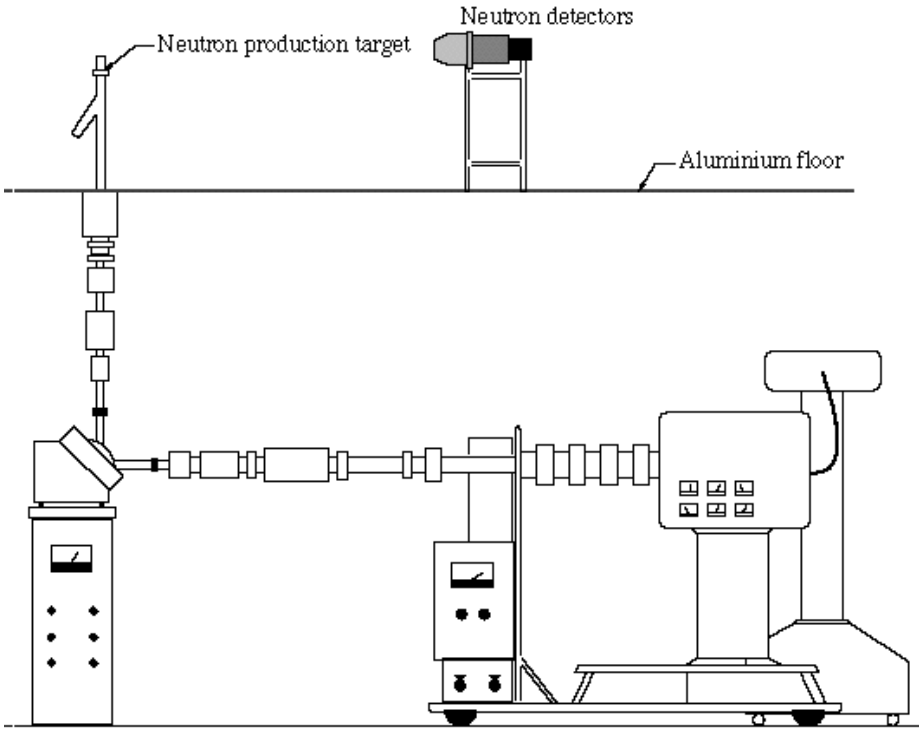

Fig. 3.2. The neutron generator facility at the Department of Reactor Physics. The measurements were performed on a thin aluminium floor, thus reducing the amount of scattered neutrons. From paper I.

The deuteron beam was pulsed with an internal bunching definition of less than 1 ns. An electron detector situated close to the tritium target served as time reference for the neutron pulses.

3.2 Experiment

3.2.1 Experimental set-up

The set-up is described in detail in paper I, and only a brief description will be given here. The detectors were of hexagonal cross section due to their usage in the NORDBALL set-up and had an active volume of 3.33 l. The liquid scintillator used in the detectors was Bicron BC-501. The fact that the flux was isotropic was used to distinguish the cross-talk events from the true neutron-neutron coincidences. The experimental geometry is shown in fig. 3.3. The detector A was kept at 3 m distance from the neutron production target. The detector B was placed 0.33 m apart from detector A, where an appreciable rate of cross-talk events was expected. A second measurement was made with the detector placed in position B', still with 3 m distance from the target but with 2.5 m distance to detector A. In this position, the expected cross-talk rate is negligible due to the small solid angle and the fact that scattering angles exceeding 90° do not occur for elastic scattering against protons.

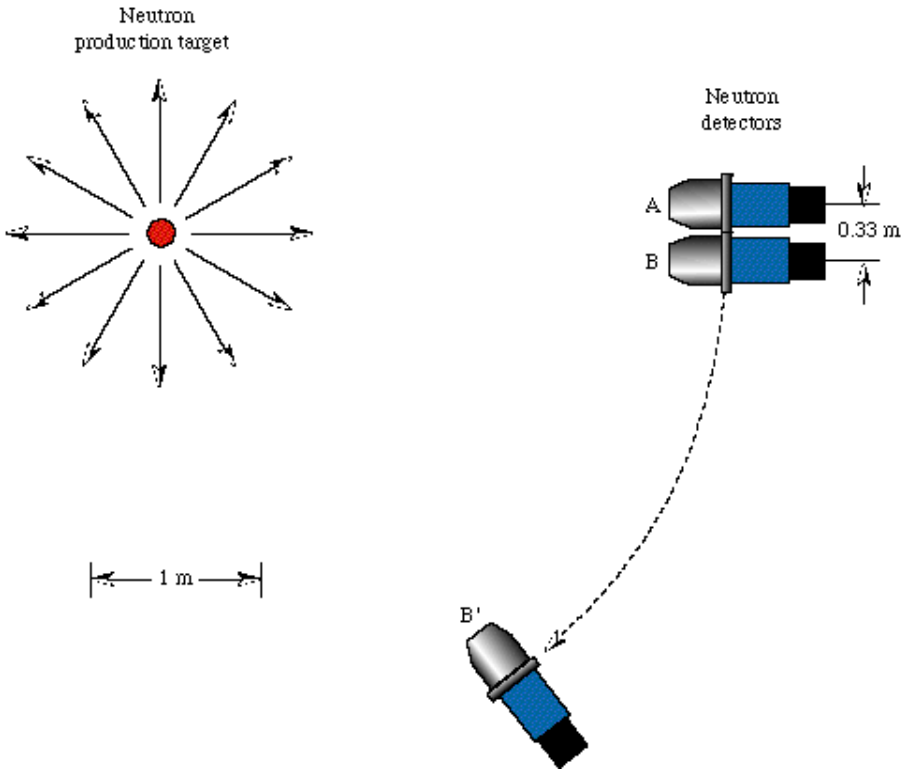

Fig. 3.3. Top view of the set-up used in the cross-talk experiment. The isotropic neutron flux in the z-plane allowed a simple reduction of the background from n-n coincidences by measuring with the detectors close together and far apart. From paper I.

The trigger for the data acquisition was set to demand coincidences between the two detectors. The time-of-flight between the deuteron pulse, defining when the neutrons

are created, and the registered hits in the neutron detectors was recorded together with pulse shape information according to figure 2.5. After selecting the neutron events, the TOF-spectra shown in fig. 3.4 were obtained for detector A with detector B in the two different positions. Small peaks are found at the time corresponding to prompt gamma rays from the beam hitting the target. These are not actual failures of the pulse shape discrimination method, we have here n-(γ+n)-coincidences. In these events, one detector is hit by a prompt gamma ray and a prompt neutron during the same accelerator pulse. The gamma ray then arrives first, determining the timing of the event, and the subsequent neutron deposits suitable amounts of energy to emulate the shape of a neutron pulse. The normalized difference spectrum is shown in the lower part of fig. 3.4. A broad distribution is shown where the cross-talk events are supposed to be found. The difference of the peaks from the true coincidences gives rise to strong positive and negative oscillations due to a small timing shift between the measurements. The integral of these oscillations gives no net contribution to the count rate.

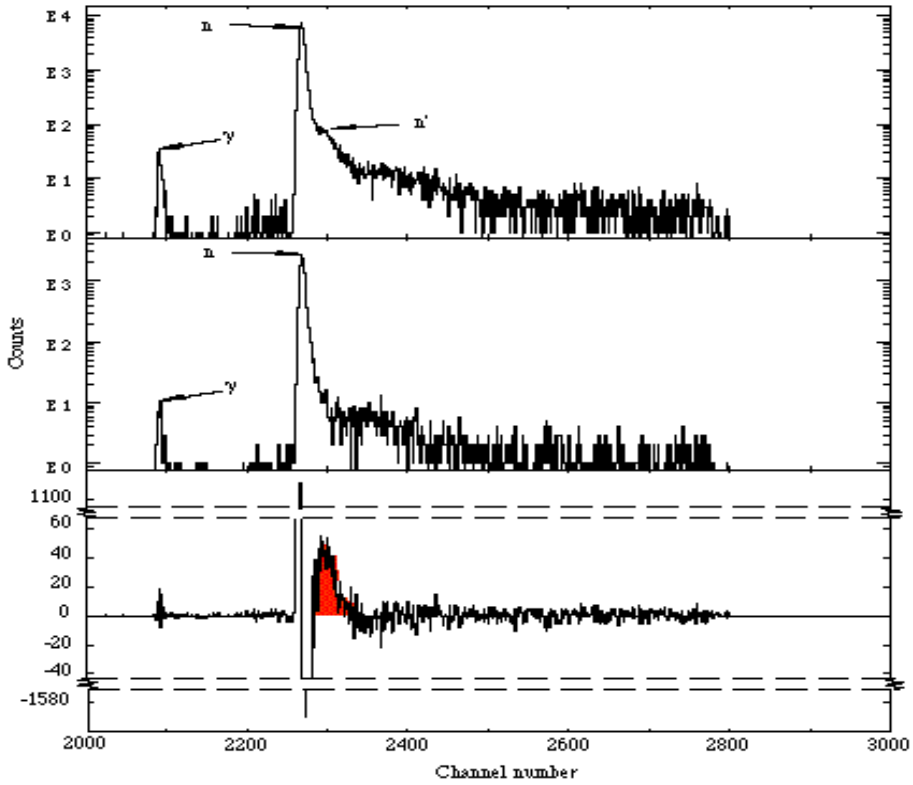

Fig. 3.4. TDC-spectra from position B (upper plot), B' (middle) and the difference spectrum (lower) after normalization. A clean TOF distribution of the cross-talk events remains after subtraction of the neutron-neutron coincidences.

In the experiments described in [59,77] a high-granularity central array of small cylindrical (Ø = 50 mm) neutron detectors was used. The cross-talk experiment was repeated with two of these detectors, mounted with 100 mm distance between the

detector centres. During this beam-time only a very low intensity neutron flux was available, and the beam bunching did not function properly either. These problems led to the advantage of having very few true neutron-neutron coincidences. The deduced cross-talk probabilities for the two measured geometries are listed in table 3.1.

	Experimental cross-talk probability	**Monte-Carlo calculation**
Hexagonal detector	$(2.5\pm1.1)\ 10^{-4}$	$(2.8\pm0.5)\ 10^{-4}$
Small cylindrical detector	$(2.5\pm0.4)\ 10^{-3}$	$(2.5\pm0.4)\ 10^{-3}$

Table 3.1. Experimental and theoretical cross-talk probabilities.

3.2.2 Monte-Carlo calculations

The Monte-Carlo code Menate was used for calculating the cross-talk. The code uses parametrized cross sections for elastic and inelastic scattering of neutrons against hydrogen and carbon and can mimic the situation for any given energy, detector geometry and threshold setting. Menate was run with settings corresponding to the values used in the experiments, yielding the results shown in table 3.1.

Experiment

4. The ISOLDE experiments

4.1 Background

4.1.1 Physics motivation

The ISOLDE Facility at CERN is ideal, in several features unique, for decay studies of exotic nuclei. The very high production yield of a number of halo nuclei, together with the low extraction energy, gives the experimenters access to study a strong, renewable ”radioactive source” reaching lifetimes down to a few milliseconds.

A typical property of extremely neutron-rich nuclei is ß-delayed particle emission which has been intensely studied at ISOLDE and other facilities. Can the decay properties of a halo nucleus tell us something about its initial internal structure? It should be clear that the measurable quantities are not directly properties of the wavefunction of the parent nucleus. But as already mentioned in section 1.2.5, the decay can preserve enough of the properties to get a picture of the original state. In fig. 4.1 the systematically high B_{GT} -values for decays to states within 3-5 MeV Q-value in the daughter nuclei are shown. The high B_{GT} -values indicate a large overlap between the initial and final states.

4.1.2 Experimental facilities at CERN-ISOLDE

The ISOLDE Facility has undergone a considerable metamorphosis during the years of this work. The ISOLDE-2 and ISOLDE-3 separators were connected to the synchro-cyclotron SC which delivered 600 MeV protons or 910 MeV ^{3}He. The production yield of some nuclei was enhanced using the latter primary beam. The ISOLDE-3 facility was developed as a high resolution instrument, but the layout of the site prohibited using the optimum ion-optical configuration.

When the SC was phased out of the CERN accelerator programme, a new facility was constructed, ISOLDE-PSB, where the primary beam is protons from the PS Booster with 1 GeV energy. As can be seen from fig. 2.1, the fragmentation production yields are strongly enhanced for light nuclei with increasing proton energy. The pulsed primary beam also allows for background measurements between spills and reduces the problems of target heating.

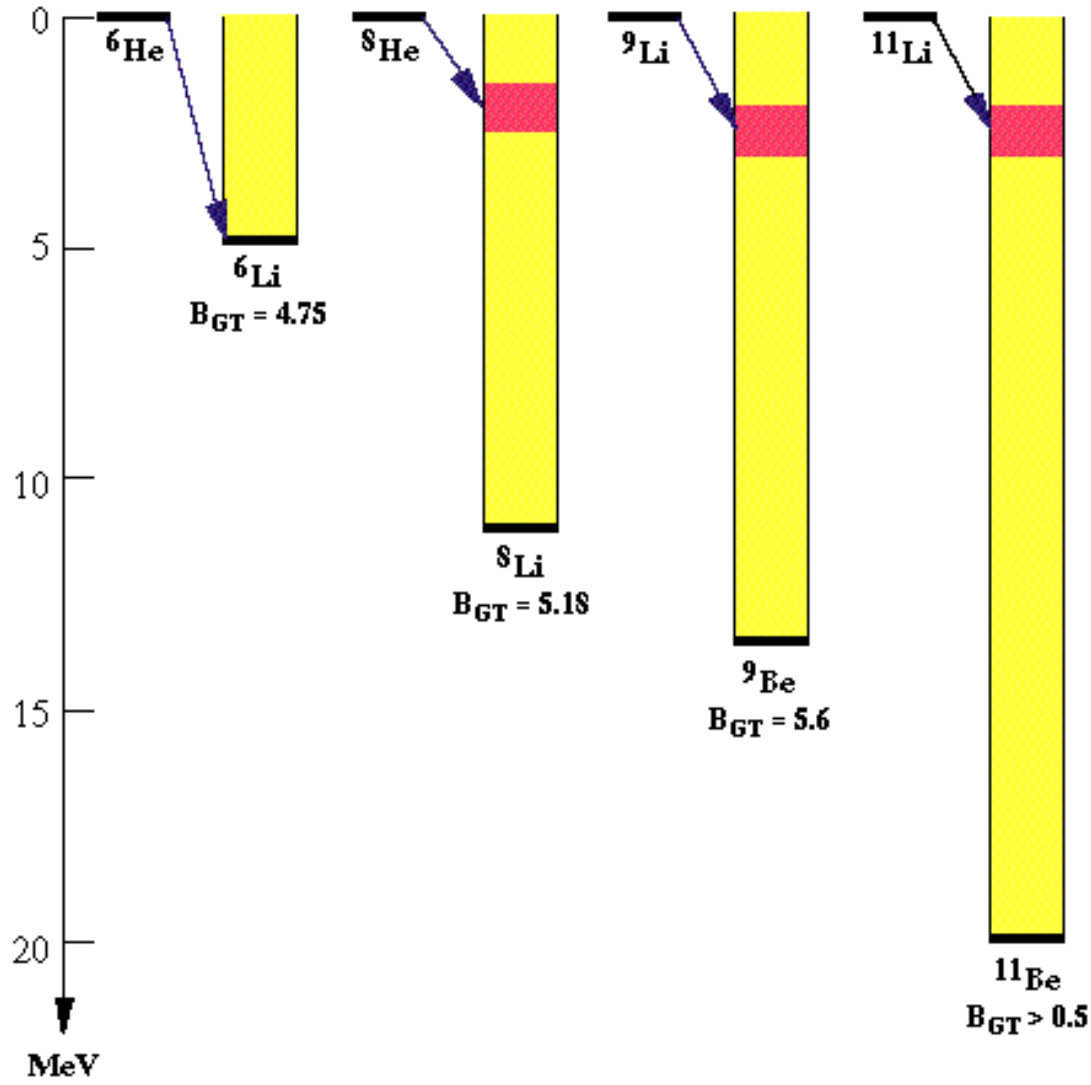

Fig. 4.1. B_{GT}-values for decays with Q-values of 3-5 MeV to states in the daughter nuclei for some neutron-rich isotopes.

4.2 Beam production

The production of ^{6,8}He was accomplished by letting a 910 MeV 1 μA ^{3}He beam from the Syncro-cyclotron impinge on a ThC-C target. The reaction products were ionized in a heated, Ar-filled FEBIAD-source and thereafter accelerated to 60 keV and mass separated at ISOLDE-2. The yield was $2 \cdot 10^5$ ions/s of ^{6}He and $2.3 \cdot 10^4$ ions/s of ^{8}He.

4.3 The experimental set-up

The main aim of the experiment described in paper II was to measure the beta-delayed charged particles from ^{6,8}He. It was previously known that there exists a deuteron branch from ^{6}He [23] and a triton branch from the decay of ^{8}He [80], but the experiments suffered from a very critical geometry and a rather high low-energy cut-off respectively. In [80], a ”classical” cylindrical proportional chamber was used as a ΔE-detector. In order to lower the low-energy cut-off a new ΔE-detector was developed.

4.3.1 The telescope detector — first generation

In order to decrease the energy loss in windows, dead layers and ΔE-detector and thus lower the detection limit, a new telescope was developed with a low-pressure proportional chamber as ΔE-detector. The geometry chosen was a mixture of the traditional proportional chamber and a parallel-plate detector [81]. The shape was cylindrical and the gas volume was limited by two thin polypropylene windows. Close to the entrance window a wire grid on ground potential was situated and at the exit window, wires on high voltage were mounted. See fig. 4.2. The wires on positive voltage had

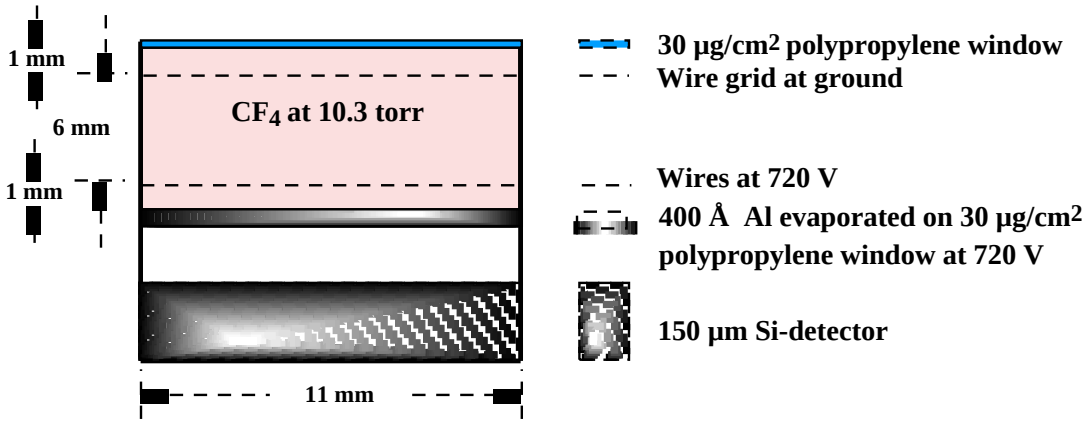

Fig. 4.2. Cross section of the gas telescope detector used in paper II.

20 µm diameter. The used voltage and the thin wires used created a field where the primary electrons drifted towards the anode wires without further ionization. In the close vicinity of the wires, the field was sufficient to allow secondary ionization. The gas used was CF_4 (freon R14) with low pressure, 10.3 torr. CF_4 was chosen due to its high drift velocity and low tendency of deposit build-up on the wires [82].

The charged particles traversing the gas volume then hit an ordinary surface barrier silicon detector, sufficiently thick to stop them completely.

4.3.2 The detector assembly

The final set-up used at ISOLDE-2 is shown in fig. 4.2. The incoming beam from the separator passed through a collimator and was implanted in a thin carbon foil (100 $\mu g/cm^2$). The collector foil was mounted on a turnable wheel, which also contained calibration sources, and was surrounded by the telescope and two silicon detectors. These were covered with 0.5 mm aluminium foil in order to prohibit heavier particles than electrons from penetrating and were used for monitoring the ß-activity. The data acquisition allowed for demanding coincidences between the telescope and the silicon detectors in order to exclude ß-events in the telescope, but this reduced the statistics too severely due to the small solid angle. The efficiency for ß-particles in the gas detector was anyhow reassuringly low.

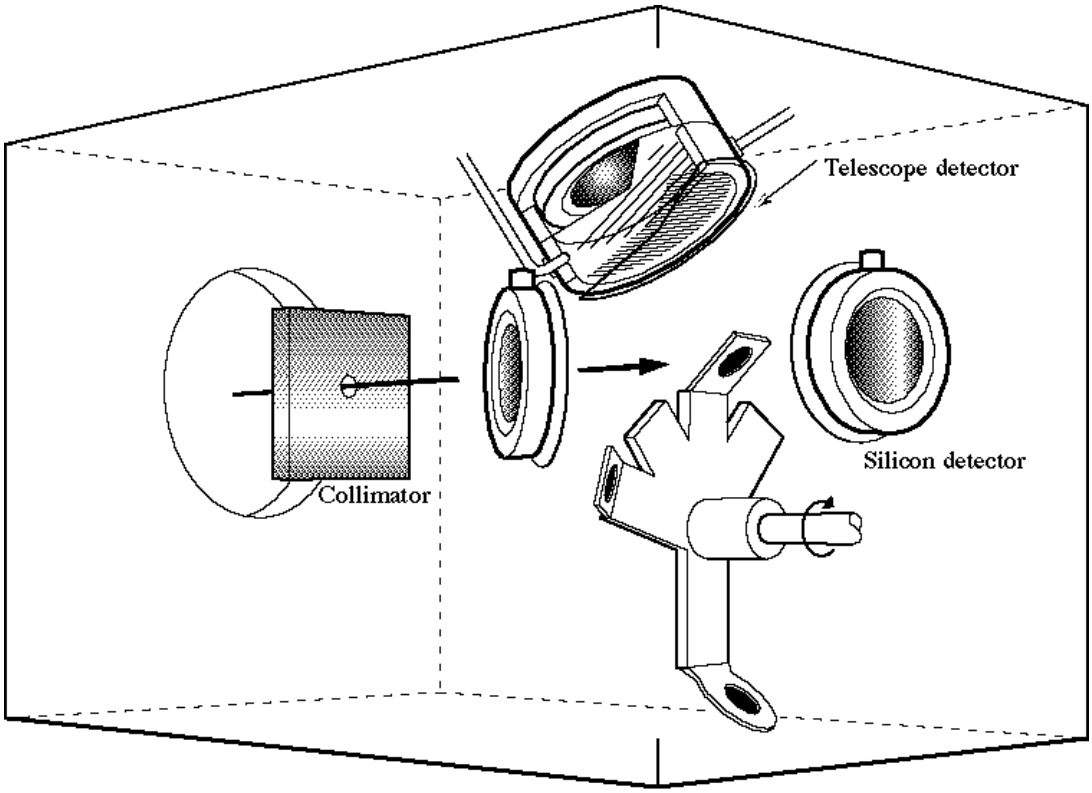

Fig. 4.3. An artist's view of the experimental set-up used. The collimated beam from the ISOLDE-2 separator was collected on a catcher foil, surrounded by the various detectors.

4.3.3 Experimental data

The ΔE-E plot, obtained with the gas telescope, for the ß-delayed charged particles emitted from ^{8}He is shown in fig. 4.4. The α-particles and the tritons are well separated down to low energies. The triton events were selected by applying polygon cuts in the bi-dimensional ΔE-E plot.

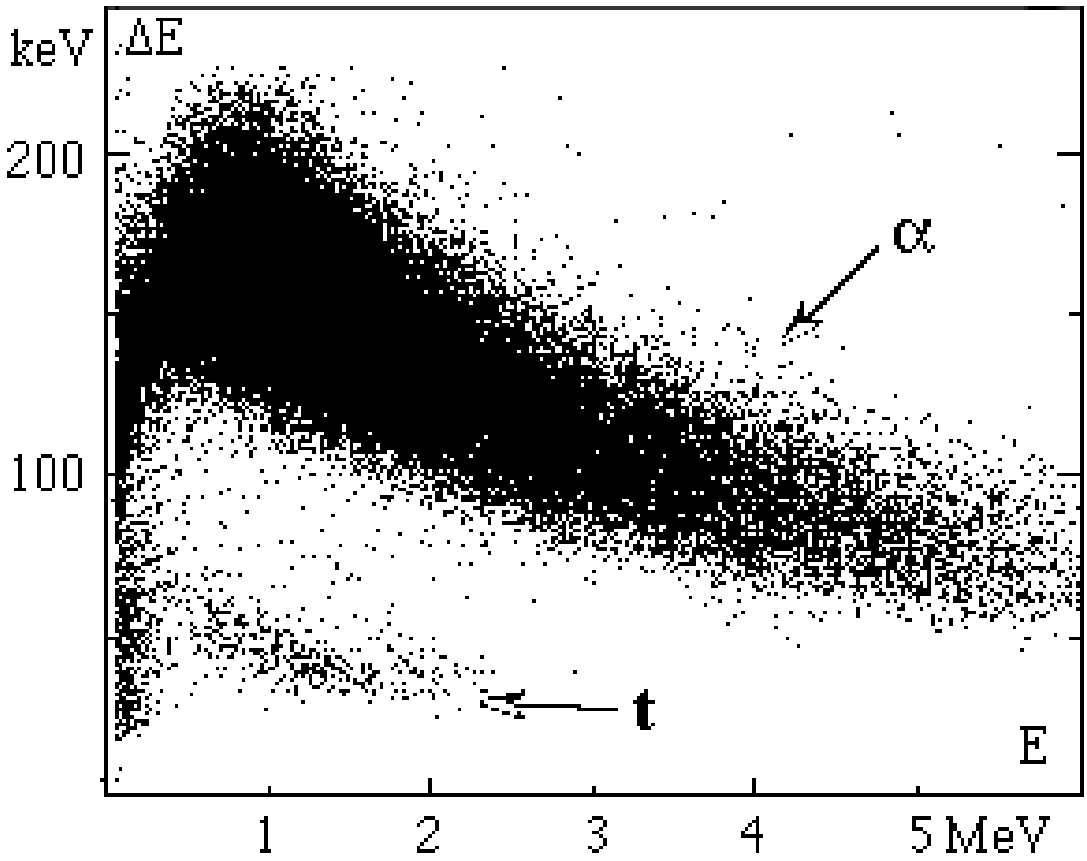

Fig. 4.4. ΔE-E-plot obtained with the gas-detector telescope showing the ß-delayed charged particles from ^{8}He. The α-particles and tritons are well separated.

4.3.4 The telescope detector — second generation

In order to lower the low-energy cut-off of the telescope, further modifications have been made. The geometry was turned around to allow for one window only, see fig. 4.5. This leaves the silicon detector immersed in the counter gas which might decrease the lifetime through flash-overs.

This geometry was used in a later experiment at ISOLDE, aiming at measuring all ß-delayed particles from the decay of ^{11}Li, including neutrons [60] using several liquid-scintillator detectors. Here, a thicker entrance window was used in order to allow for implantation of the radioactive beam in the foil. Thus, an optimal solid angle could be obtained, also for charged particles from daughter activity. This was crucial for detecting α-particles from the decay chain

$$^{11}\mathrm{Li} \xrightarrow{\beta^-} {}^{9}\mathrm{Li} + \mathrm{d}$$
$$\hookrightarrow {}^{9}\mathrm{Li} \xrightarrow{\beta^-} {}^{9}\mathrm{Be}^{*} \rightarrow \alpha + \alpha + \mathrm{n}$$

allowing for an indirect identification of the peripheral ß-decay shown in fig. 1.7. The experimental data are still under analysis, but some results are given in ref. [11] and will be discussed in section 6.4.1.

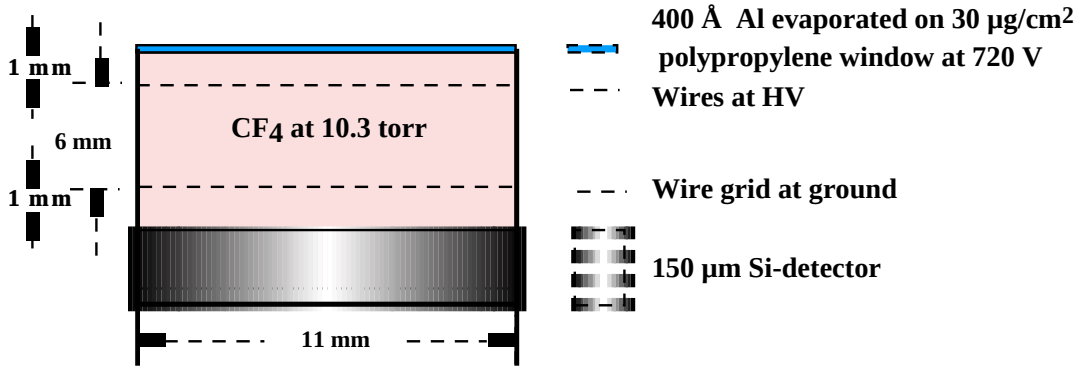

Fig. 4.5. Cross section of the ”overturned” gas telescope detector.

5. The GSI experiment

The planning, preparing, executing and finally analysing and interpreting of the experiment at GSI made up the largest part of this work. It will therefore be treated in some detail here.

5.1 Background

5.1.1 Physics motivation

During the early planning stages of the experiment at GSI, with proposal number S034, no data on dissociation of ^{11}Li existed in the region 28-790 MeV/u secondary beam energy. The measurements previously done had either focused upon measuring charged fragment momentum distributions [38] or neutron angular distributions [6]. At GSI, the possibility existed to measure dissociation with complete kinematics, measuring the three-dimensional momenta of all incoming and outgoing participants. The possibility of bending the non-reacting ions out of the beam direction with a dipole magnet instead of stopping them in a thick detector made the signal-to-background ratio much more favourable than in the experiments performed at GANIL [6,59,77] and MSU [44,46]. There was also the possibility to measure the longitudinal momentum distributions from the break-up of ^{11}Li into ^{9}Li.

5.1.2 Experimental facilities at GSI

In recent years, GSI has expanded its experimental facilities considerably by the construction of the heavy-ion synchrotron SIS and the numerous experimental possibilities in conjunction with it. See fig. 5.1 for a schematic overview. A fragment separator, FRS, is installed in order to separate exotic nuclei at high energies - up to 18 Tm rigidity. Very advanced experiments can be performed in the Experimental Storage Ring (ESR) which can be filled with either primary beams from the SIS or secondary beams from the FRS.

The detection facilities are well developed in several ”caves”, of which the largest and most versatile is the cave B, the so-called 4π-cave. It houses the FOPI detection system which is used for complete kinematics nuclear matter studies. Further down the beam line, the dipole magnet ALADIN and the large area neutron detector LAND, both used in the present work, are situated.

Fig. 5.1. Overview of GSI with the ion-sources, linear accelerator UNILAC, heavy-ion synchrotron SIS, the fragment separator FRS, the experimental storage ring ESR and the experimental area with cave B.

5.1.3 The experiment

The experiment was logically and physically divided into two parts. Using the FRS in the energy-loss mode, the longitudinal momentum distributions of the charged fragments created in the break-up of ^{11}Li into ^{9}Li were measured. In cave B, a set-up with ability to measure break-up reactions with complete kinematics was utilized. The experiment was the first full-scale experiment made, producing a secondary radioactive beam and studying the secondary reactions at the main experimental area.

5.2 Beam production

5.2.1 General conditions

For the first part of the experiment, when a secondary beam of ^{11}Be was produced, the primary beam of ^{18}O, was ionized in a RFQ (Radio Frequency Quadrupole) source and preaccelerated in the HLI (High Charge Injector), bypassing the first part of the linear accelerator UNILAC. The primary beam intensity was here 10^9 particles/s. Later, in order to maximise the intensity of the more exotic nuclei ^{8}He, ^{11}Li and ^{14}Be, a Penning-type ion-source with higher output, $2 \cdot 10^{10}$ particles/s, was used. The ^{18}O beam was first accelerated in the UNILAC to 20 MeV/u and afterwards injected into the SIS synchrotron. The energy of the primary beam in SIS was varied between 340 and 640 MeV/u in order to maximise the yield of the secondary nuclei of interest at

the intrinsic rigidity of 9.5 Tm. A problem of the beam transport was the fact that no direct beam-line connection existed between the FRS and the main experimental area. Thus, the secondary beams had to pass the ESR in the so-called α-mode, meaning that the beam took one turn. A phase-space mismatch between the two instruments severely limited the transmission to roughly 2 %. However, a benefit of the bad transmission was that the momentum width was limited to $\Delta p/p \approx 10^{-3}$, yielding a good momentum definition of the secondary ions.

The passage through the ESR meant a further limitation of the experiment. The nominal bending power of the FRS and the transfer beam line was 18 Tm, but the nominal bending power of the ESR was limited to 10 Tm. In order to avoid fringe fields a setting of 9.5 Tm was used. The transfer beam line was thus also fixed at a rigidity of 9.5 Tm for all secondary beams which defined the beam energy for those.

5.2.2 Production of ^{11}Be

In the case of ^{11}Be, the primary energy was set to 520 MeV/u. The FRS was operated in an achromatic mode, using a Bρ-ΔE-Bρ selection (see section 2.3.1 and fig. 2.2). A problem during the setting-up phase, illustrating the sensitivity of the separator ion-optics, was that though the settings were correctly made with the stable beam of ^{18}O for transfer of ^{11}Be, the main component reaching cave B, located 300 m downstreams, was ^{13}B. This was an effect of the thin scintillator paddle mounted in the dispersive focal plane of the FRS, effecting the achromacity of the separator. See also section 5.5.2. Only when a setting of the last stages of the FRS with a simultaneous monitoring of the ions arriving at the experimental set-up was done, a correct setting could be found.

5.2.3 Production of ^{8}He, ^{11}Li and ^{14}Be

The production of ^{8}He, ^{11}Li and ^{14}Be was facilitated by the extreme relation between neutrons and protons these nuclei exhibit, $A/Z \geq 3.5$. Thus, only a Bρ-selection was necessary of the fragments produced from the 340 MeV/u ^{18}O beam. In figure 5.2 an excerpt of the chart of the nuclides is shown, together with the limits of transmission imposed by the fragmentation of a primary ^{18}O beam and the Bρ-selection, if only fragmentation of the primary beam is taken into account. As can be seen, this selection yielded the wanted species with some contamination of tritons and ^{6}He. Fig. 5.3 shows the energy-loss spectra in the thin plastic scintillator POS2 (fig. 5.4) situated in front of the secondary reaction target in the 4π-cave for the two cases, with and without degrader.

5.3 Longitudinal momentum distributions

During the experiment, my main concern was regarding the complete kinematics set-up. Thus, I participated only in the interpretation of the results from the longitudinal momentum distributions simultaneously measured at FRS and will not dwell upon the experimental details from this part of the experiment. However, a brief description of the experimental set-up is necessary in order to understand the results.

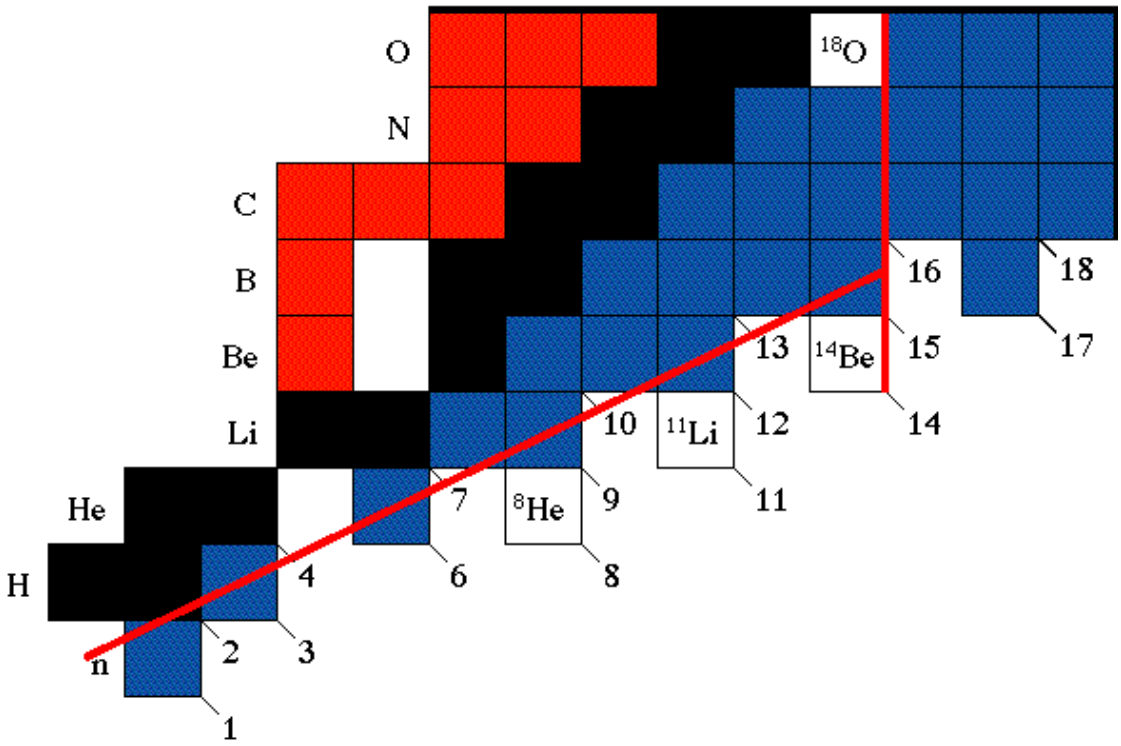

Fig. 5.2. Excerpt of the nuclear chart showing the Bρ-selection (only the nuclides below the sloping line are able to pass if no momentum spread of the secondary ions is assumed) upon the nuclides possible to produce by fragmentation of a primary ^{18}O beam.

The FRS was run in the energy-loss mode as illustrated in fig. 1.15. This meant that the secondary reaction target, Al or Pb, was mounted in the middle focal plane of the instrument. A change in the longitudinal momentum in the break-up process was transformed into a position change in the final focal plane which could be re-calculated into longitudinal momentum. The position distributions were measured with *one* Bρ-setting by means of position-sensitive multi-wire chambers, with additional TOF- and ΔE-measurements utilizing scintillators and an ionization chamber (PPAC) for particle identification. The momentum spread of the incoming ^{11}Li beam, caused by the production process, does not, in first-order ion-optical imaging, affect the measured width. In order to compensate for effects induced by angular scattering, energy-loss straggling and ion-optical aberrations the distributions obtained from transmission measurements through the same secondary targets with the non-reacting ^{11}Li were used. As the secondary target had a constant thickness, thus disturbing the achromacity, some additional compensations had to be made. The transverse acceptance of the FRS for this measurement was ±105 MeV/c and the longitudinal ±60 MeV/c.

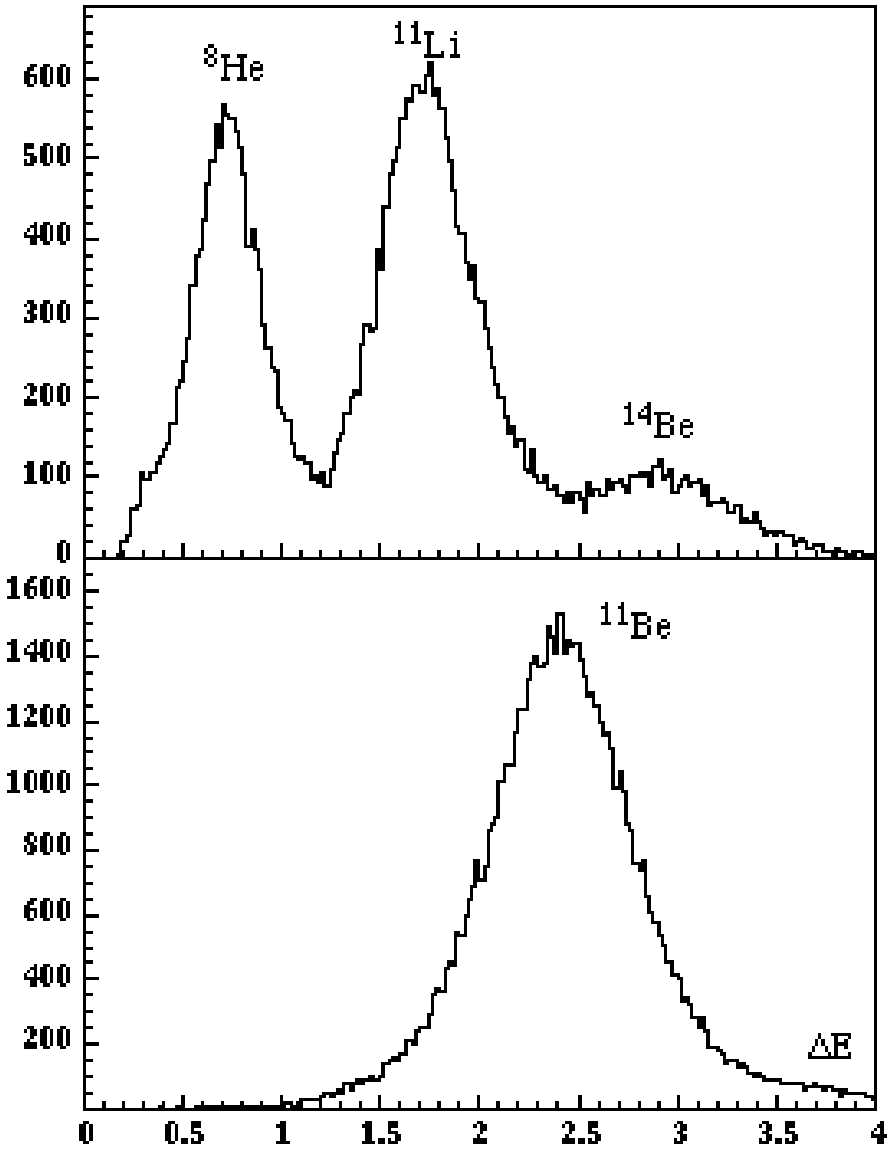

Fig. 5.3. Energy-loss spectra from the thin plastic scintillator POS2 situated in the 4π-cave show the charges of the secondary ions in the two modes of the FRS, without and with degrader

5.4 Complete kinematics experiment — set-up

The experimental set-up for the complete kinematics experiment in cave B is shown in figure 5.4. The positions of the incoming ions were defined by a MWPC [83] at the entrance of the cave. Close to the secondary reaction target, a scintillator foil read out by four photomultiplier tubes was situated. This detector also had a certain position resolution according to section 2.4.1.3 and was labelled POS2.

Right in front of the secondary reaction target, a position sensitive MWDC was mounted. It is labelled MWDC-1 in the figure. Directly behind it, the secondary tar-

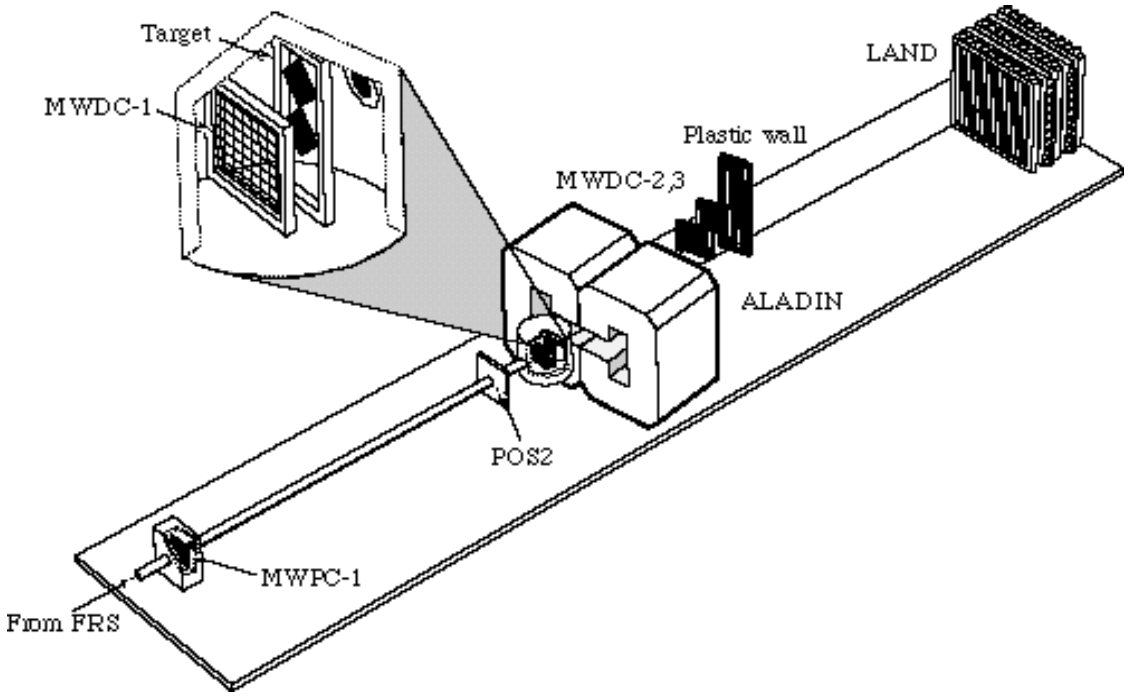

Fig. 5.4. An artists view of the experimental set-up in the 4π-cave at GSI. The target chamber containing MWDC-1 and the target ladder is magnified.

gets were mounted on a target ladder. It had the capacity of housing two targets and an empty target frame and could be manipulated from outside the cave.

The target was followed by a large-gap dipole magnet, ALADIN [84], with a maximum magnetic field of 1.6 T. The deflected charged fragments were subsequently detected in two MWDCs marked MWDC-2 and MWDC-3 respectively. A final time-of-flight and energy loss measurement was performed using a thin plastic wall (TOF-wall) consisting of 7 paddles.

The neutrons were detected in the Large Area Neutron Detector, LAND [72], described briefly in section 5.4.2.

5.4.1 The Multi-Wire Drift Chambers

The three MWDCs used were developed jointly by the TH Darmstadt, Aarhus University and CTH/GU Gothenburg groups, solely for this experiment. The main features were taken from ref. [85] and a very thorough description of the building, testing, calibration and analysis procedures is given in refs. [86,87].

Each wire plane consists of alternating cathode and anode wires with 5 mm spacing. A schematic picture is shown in fig. 5.5. The anode wires are of 20 μm diameter and the double cathode wires of 50 μm diameter with 500 μm internal distance. The wires were made of gold-plated tungsten. The double cathode wires modify the field in order to enhance the charge collection.

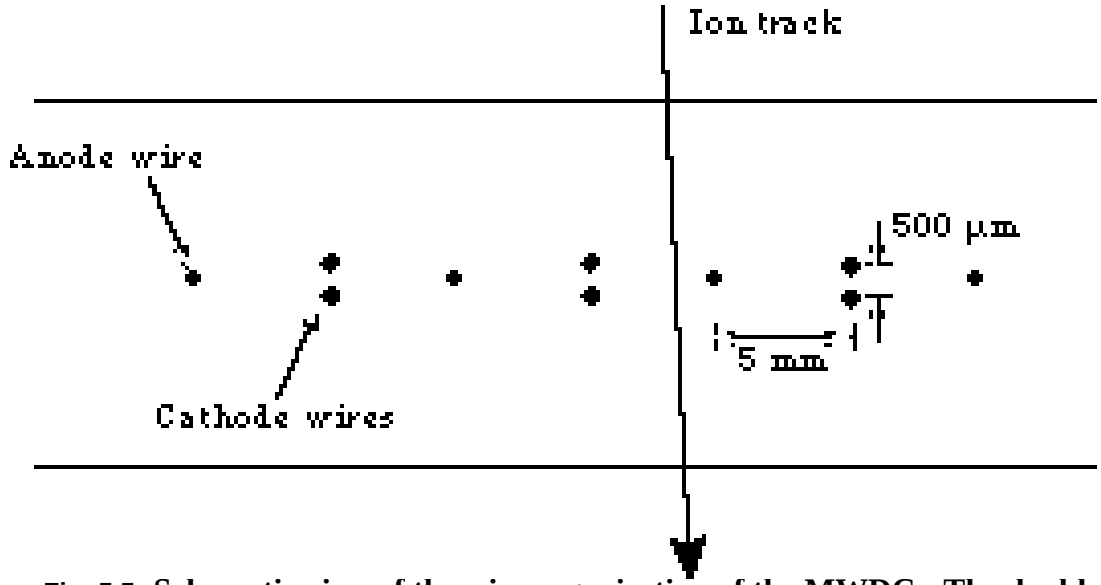

Fig. 5.5. Schematic view of the wire organisation of the MWDCs. The double cathode-wire arrangement enhances the charge collection.

Each plane in the MWDCs yields 5 parameters, as an example the parameters from MWDC-1 are listed in table 5.1. The times are all measured with respect to the trigger detector POS2.

Entity	Description
t_L	Time read out at left end of delay line
t_R	Time read out at right end of delay line
t_C	Time read out at one cathode
$E_{C,\,ODD}$	Energy read out from odd cathodes
$E_{C,\,EVEN}$	Energy read out from even cathodes

Table 5.1. Parameters read out from MWDC-1.

A schematic picture of the read-out is shown in fig. 5.6. The anode wires are connected to a delay line with a delay of $t_{delay} = 2$ ns between each wire. Thus, the total time between the passage of the ion (approximately given by the trigger detector) and the pulse arrival at the left and right ends of the delay line can be expressed as

$$t_L = nt_{delay} + t_{drift} \tag{5.1}$$

$$t_R = (N-n)\,t_{delay} + t_{drift} \tag{5.2}$$

if the total number of delay modules is N and the ion passes drift cell n, ranging from 0 to N. The wire having fired can be deduced according to

$$t_L - t_R = (2n - N)\, t_{delay}. \quad \textbf{(5.3)}$$

To find the track location within the cell, the drift-time information is needed. It is extracted by forming the entity

$$t_L + t_R = 2t_{drift} + Nt_{delay} \quad \textbf{(5.4)}$$

The remaining degree of freedom is whether the location of the track is to the left or to the right of the anode wire. This was determined from the pulses induced in the surrounding cathode wires. These origin from the avalanches at the anode wires and the size of the signal is sensitive to which side of the anode wire the avalanche takes place. Thus, an unambiguous position determination can be made by comparing the odd and even signals.

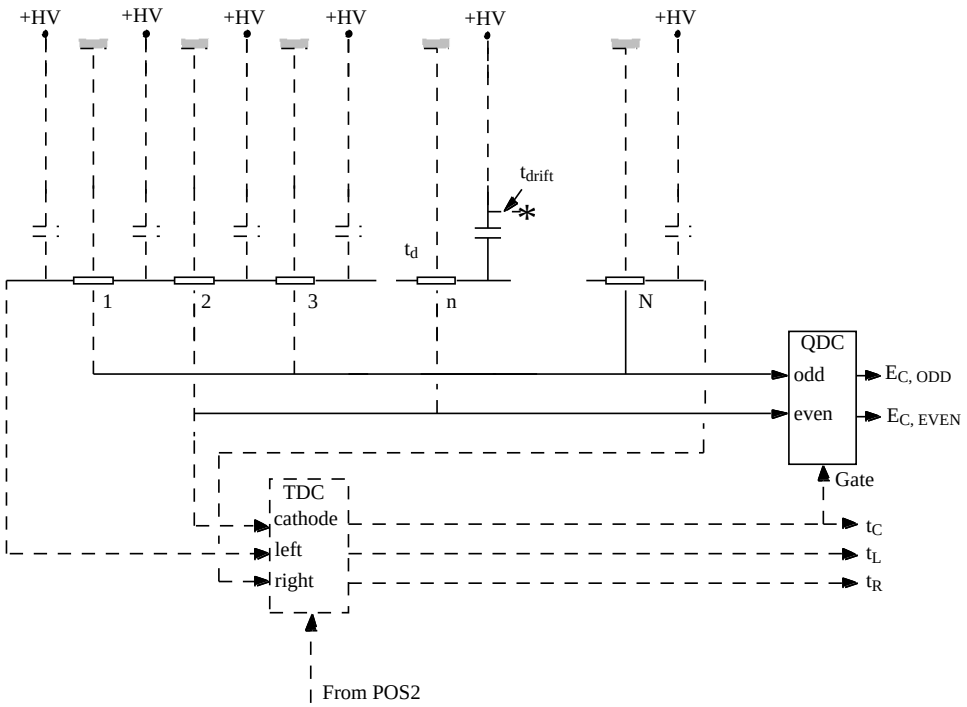

Fig. 5.6. Schematic picture of the MWDC read-out. The anode wires are read out in both directions along a delay line. The cathode wires are alternatingly connected to signal lines labelled ”odd” and ”even”.

As the pulses from the cathode wires stem from the secondary ionization avalanche at the anode wire, the relation **(5.5)**, where t_C denotes the time of the cathode pulse, is valid:

$$t_C \approx t_{drift} \quad \textbf{(5.5)}$$

Thus, the *checksum* variable can be formed according to:

$$t_{check} = t_L + t_R - 2t_C \approx N t_{delay} \quad \textbf{(5.6)}$$

As can be seen from **(5.6)**, this entity should be approximately constant for a correct event. Multiple hits where the pulses read out at the left and at the right end of the delay line do not origin from the same ion can thus be discarded.

The modules used in the delay line exhibited a considerable spread with regard to delay time. This made the locations of the peaks in the wire identification spectra (according to **(5.3)**) unlinear, and every peak, corresponding to a wire, had to be treated separately. Also the relation between drift time and track position within the drift cell exhibited strong unlinearities. If the flux of incoming particles is uniform over the drift cell, the resulting drift-time distribution would ideally resemble a rectangle. This was definitely not the case for the used MWDCs, having a distribution as is shown in fig. 5.7. From count-rate considerations it could be deduced that this

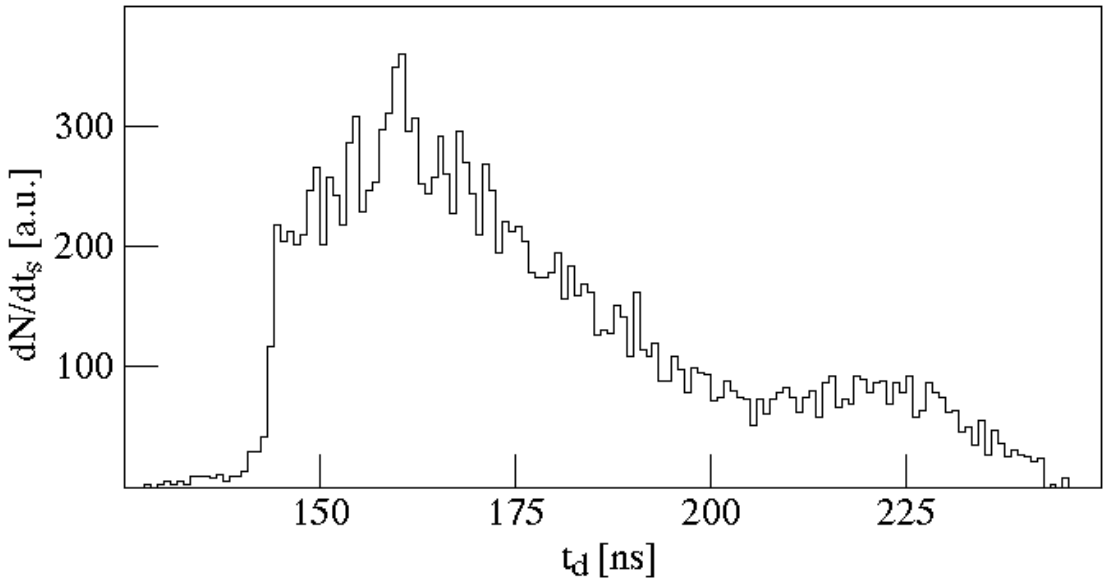

Fig. 5.7. Typical drift-time distribution from the x-plane of MWDC-3, obtained with a 640 MeV/u ^{18}O-beam. From ref. [87].

behaviour did not result from efficiency variations within the drift cells. The unlinearities could not be fully explained in the analysis. One possible explanation would be formation of a cloud of δ-electrons, widening the primary ionization volume. The transformation was thus made with look-up tables created from data where the drift cell in question was homogeneously irradiated by the beam, assuming a position-independent efficiency. The unlinearities in the drift time severely degraded the position resolution to slightly better than 2 mm.

5.4.2 The neutron detector LAND

The LAND detector is made up of 200 submodules, paddles, each 2m*0.1m*0.1m, arranged 20 by 20 in layers, alternating vertically and horizontally aligned. See fig. 5.8. The total active volume is 2m*2m*1m. Each of the paddles is made up of 10

alternating layers of iron and plastic scintillator. The incoming neutrons interact with the iron nuclei by producing hadronic showers that are detected in the scintillator material.

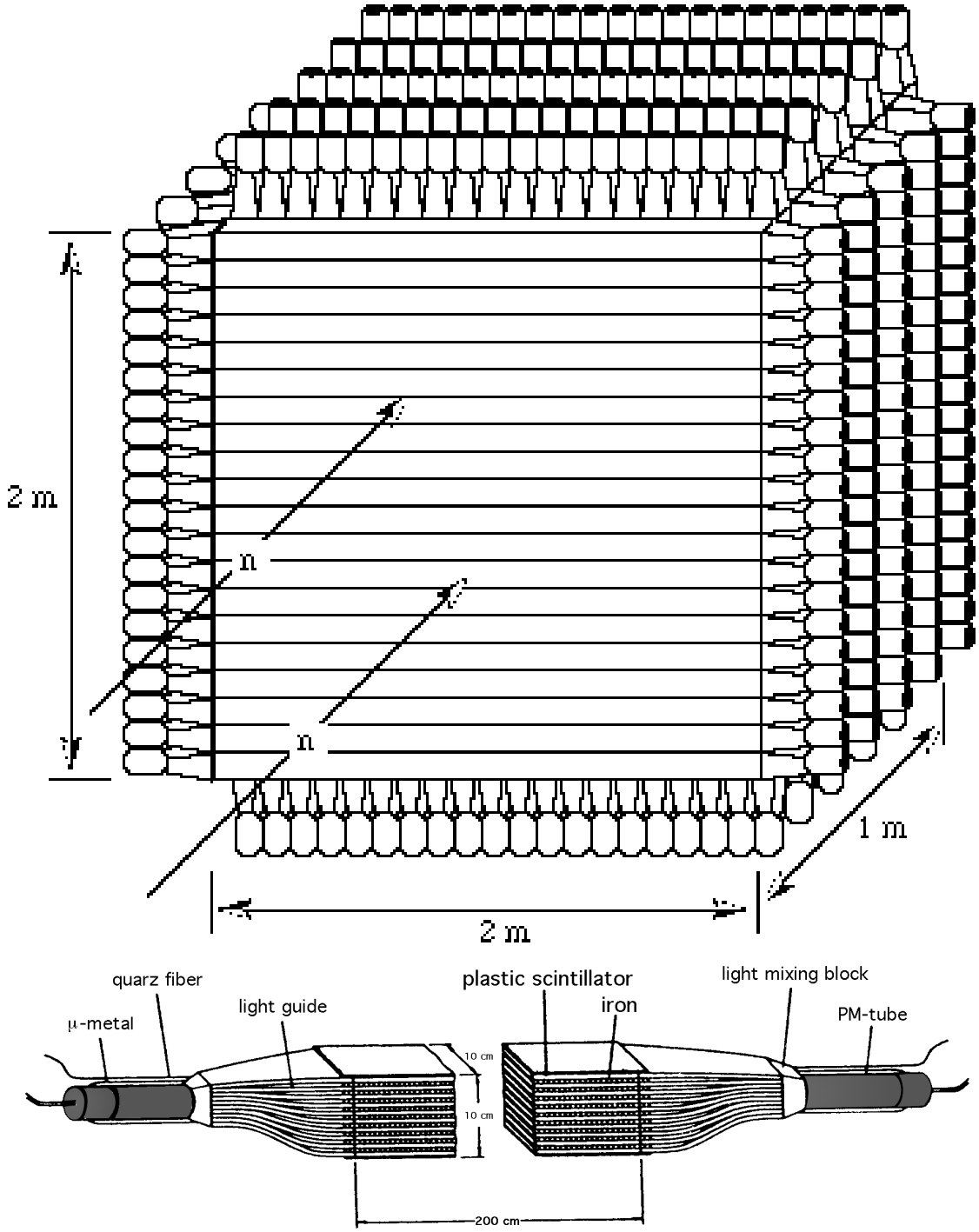

Fig. 5.8. View of the Large Area Neutron Detector (LAND). The lower inset shows how each of the 200 paddles are constructed.

A high position resolution is obtained due to the good time resolution and high granularity, 6 cm along the direction of the paddle and 10 cm perpendicular to the direction of the paddle. A tracking algorithm [56] is used for optimization of the position deter-

mination and disentangling of multi-neutron events when more than one paddle is hit. The efficiency for 240 MeV neutrons is high, 85±6 %. An internal time-calibration monitoring is made in between beam spills by using cosmic rays.

5.5 Reaction identification - event selection

In order to extract the wanted information for the different measured reactions, the correct events had to be singled out. The procedure to do this was similar for all beams, in the subsequent discussion the reaction $^{8}\mathrm{He} \rightarrow {}^{6}\mathrm{He} + n + X$ will be used as an example.

5.5.1 Selection information

The selection of the $^{8}\mathrm{He} \rightarrow {}^{6}\mathrm{He} + n + X$ events was made by demanding several conditions. As the beam from FRS was mixed (see figs. 5.2 and 5.3), a selection of the incoming ^{8}He was necessary. The outgoing fragments also had to be identified according to mass and charge. The ”tools” available were the ΔE, TOF and position information from the beam detectors. The most important measured and synthesized entities which were used in the data analysis are listed in table 5.2

Entity	Description
POS2E	ΔE in the trigger detector POS2
W1XPO	x-position in the MWDC-1
W1YPO	y-position in the MWDC-1
W2XPO	x-position in the MWDC-2
W2YPO	y-position in the MWDC-2
W3XPO	x-position in the MWDC-3
W3YPO	y-position in the MWDC-3
TOFX	Paddle position in the TOF-wall
TOFT	TOF between trigger detector and TOF-wall
TOFE	ΔE in TOF-wall
NX	x-position in LAND
NY	y-position in LAND
NZ	z-position in LAND
NT	TOF between trigger detector and LAND

Table 5.2. A selection of measured and synthesized entities used in the data analysis. The labels are taken from the actual n-tuples.

5.5.2 Incoming ions

The setting of the beam line allowed for ions with an intrinsic rigidity of 9.5 Tm according to

$$B\rho = \frac{p}{300Z} \quad (5.7)$$

where *p* denotes the total momentum. The rather low acceptance of the beam line implied that the ions produced and subsequently transported had the momenta, velocities and energies listed in table 5.3 with high accuracy.

Ion	p (MeV/c/u)	ß	T (MeV/u)
^{8}He	712.5	0.607545	241.253
^{11}Li	777.273	0.640682	281.696
^{14}Be	814.286	0.658149	305.736
^{11}Be	1036.36	0.743732	461.964
^{6}He	950	0.714025	398.986
^{3}H	950	0.714025	398.986

Table 5.3. Momentum, velocity and kinetic energy of the ions transmitted at the beam-line setting of 9.5 Tm.

The normal way of ion identification, following a fragment separator, is to plot the TOF (i.e. inverse velocity) as a function of the energy loss in a ΔE-detector. The optimal solution here would have been to measure the TOF between FRS and cave B, with a flight path of approximately 300 m. A ΔE-detector was placed in the middle focal plane of FRS to accomplish this, but had to be dismounted during the experiment since it disturbed the achromaticity of the separator. This meant that no actual TOF information in front of the target was available, instead the TOF of the reaction fragments and non-reacting ions between the trigger detector and the plastic wall was used. The use of this method was justified by the fact that the reaction products differ very little in velocity from the incoming ions. Thus, as shown in fig. 5.9, an ion identification plot could be made where TOFT was plotted as a function of POS2E (see table 5.2). A very clean separation could then be obtained, yielding a reliable identification of the incoming ion species by imposing two-dimensional cuts.

5.5.3 Reaction fragments

The outgoing reaction fragments passed through the aperture of the dipole magnet ALADIN. The acceptance of the magnet was well above the acceptance of the beam detectors. After selection of the wanted incoming ions, the charge of the outgoing ion was selected by applying cuts to the TOFE (ΔE in the plastic wall). The different isotopes were bent according to their rigidity and when plotting the position difference between the MWDC-2 and MWDC-3 as a function of the position in MWDC-2 (that

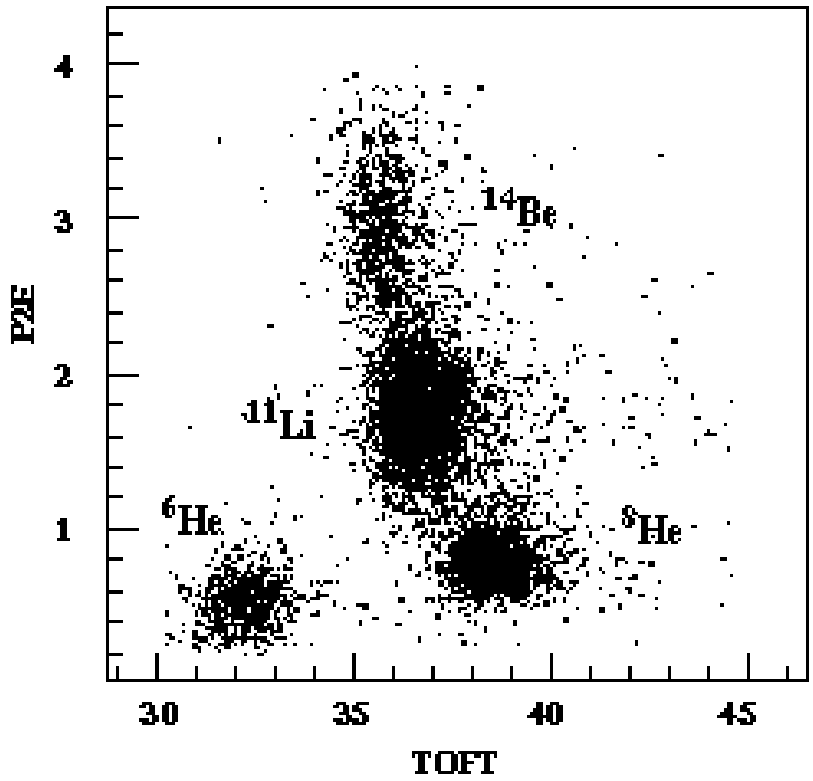

Fig. 5.9. Identification of the incoming ions could be made in the TOFT versus POS2E-plot. The incoming ions ^{8}He, ^{11}Li and ^{14}Be together with the contaminant ^{6}He are well separated.

is, W2XPO-W3XPO as a function of W2XPO), a good separation could be achieved as seen in fig. 5.10. Here an A/Z selection was made, and together with the charge identification the nuclides could be identified unambiguously.

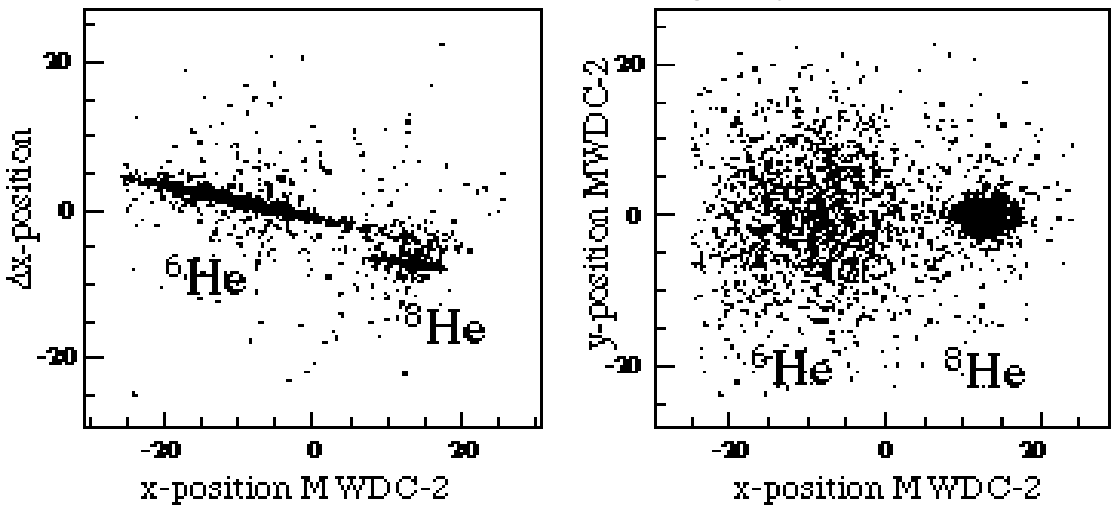

Fig. 5.10. Scatterplots obtained from the MWDCs. The left plot, with the difference in the x-position on the ordinate, yields a good separation between the different isotopes.

5.6 Extracting momentum distributions

5.6.1 Shapes and widths

An important issue in the interpretation of experiments with halo nuclei have been the shapes and widths of the momentum distributions. These two properties are closely related as pointed out in [88]. In the Goldhaber model [89] for fragmentation a Gaussian momentum distribution is obtained for the fragments:

$$W = \frac{1}{(2\pi\sigma^2)^{3/2}} e^{-\frac{1}{2}\frac{\boldsymbol{p}^2}{\sigma^2}} = \frac{1}{(2\pi\sigma^2)^{3/2}} e^{-\frac{1}{2}\frac{p_x^2}{\sigma^2}} e^{-\frac{1}{2}\frac{p_y^2}{\sigma^2}} e^{-\frac{1}{2}\frac{p_z^2}{\sigma^2}} \quad \textbf{(5.8)}$$

If instead a system that can be described by a Yukawa wave function is assumed the corresponding momentum distribution, obtained by a Fourier transform, is a Lorentzian:

$$\Psi(\boldsymbol{r}) = \sqrt{2\pi\rho}\frac{\exp(-r/\rho)}{r} \Rightarrow W = \frac{\Gamma}{2\pi^2}\frac{1}{\left(\frac{\Gamma^2}{4} + \boldsymbol{p}^2\right)^2} \quad \textbf{(5.9)}$$

The FWHM can be used for comparing different distributions if the true three-dimensional momentum distribution is measured. However, due to the strongly varying measuring conditions parallel (usually by time-of-flight) and perpendicular (normally by using position-sensitive detectors) to the beam direction this is seldom done, even in the complete kinematics experiments that have been performed where it would be possible. Instead, momentum distributions are presented and interpreted after integrations have been made of the true distribution. See Table 5.4.

Distribution	Integrations performed
$W_{\mathbf{r}}$	Along the z-axis
$W_{\mathbf{y}}$	Along the z- and x-axis
$W_{\|\|}$	Along the x- and y-axis

Table 5.4. Integrations performed when obtaining different momentum distributions. The beam is taken to travel along the z-axis.

As indicated in equation 5.8, a Gaussian distribution is separable and can be integrated once or twice without changing the width or the shape. For a Gaussian momentum distribution any effects of limited acceptance in any of the integrated directions

can be disregarded, e.g. when the longitudinal distribution is measured with a fragment separator in the energy-loss mode.

$$W_{\parallel} = \iint \left(\frac{1}{(2\pi\sigma^2)^{3/2}} e^{-\frac{\boldsymbol{p}^2}{2\sigma^2}} \right) dp_x dp_y \propto e^{-\frac{p_z^2}{2\sigma^2}}, \text{FWHM} = 2.35\sigma \tag{5.10}$$

For a Lorentzian integrated once and twice we get:

$$\begin{aligned} W_r &= \int_{-\infty}^{\infty} \frac{\Gamma}{2\pi^2} \frac{1}{\left(\frac{\Gamma^2}{4} + \boldsymbol{p}^2 \right)^2} dp_z = \frac{\Gamma}{2\pi \left(\frac{\Gamma^2}{4} + p_r^2 \right)^{3/2}}, \text{FWHM} = \Gamma \sqrt{2^{2/3} - 1} \\ W_y &= \int_{-\infty}^{\infty} \int_{-\infty}^{\infty} \frac{\Gamma}{2\pi^2} \frac{1}{\left(\frac{\Gamma^2}{4} + \boldsymbol{p}^2 \right)^2} dp_x dp_z = \frac{\Gamma}{2\pi \left(\frac{\Gamma^2}{4} + p_y^2 \right)}, \text{FWHM} = \Gamma \end{aligned} \tag{5.11}$$

where

$$p_r = \sqrt{p_x^2 + p_y^2} \tag{5.12}$$

The first case corresponds to measurements where the position of the particles behind the reaction target have been projected to a plane and the second where two-dimensional information has been used. For the GSI experiment these situations were found in the MWDCs and LAND (where the three-dimensional position information was projected upon the first plane of paddles, see section 5.6.3), respectively. For a Lorentzian distribution a complication occurs when there are limitations to the acceptance, i.e. only a limited range of p_x and p_y are able to pass through the instrument. The influence on the momentum distribution can easily be simulated by putting in finite integration limits:

$$W_{\parallel} = \int_{-\varepsilon}^{\varepsilon} \int_{-\varepsilon}^{\varepsilon} \frac{\Gamma}{2\pi^2} \frac{1}{\left(\frac{\Gamma^2}{4} + \boldsymbol{p}^2 \right)^2} dp_x dp_y = \frac{2\varepsilon\Gamma \operatorname{atan}\left(\frac{\varepsilon}{\sqrt{\varepsilon^2 + \frac{\Gamma^2}{4} + p_z^2}} \right)}{\pi^2 \left(\frac{\Gamma^2}{4} + p_z^2 \right) \sqrt{\varepsilon^2 + \frac{\Gamma^2}{4} + p_z^2}} \tag{5.13}$$

If, for example, a Lorentzian-shaped longitudinal momentum distribution with a FWHM = 47 MeV/c is fed through an instrument with limited transverse momentum acceptance ($\Delta p_x = \Delta p_y = \varepsilon$) the lineshape gets distorted according to fig. 5.11. The results regarding lineshapes and widths have to be treated very carefully to avoid interpreting an effect mainly stemming from the acceptance of the instrument.

In our experiment at the FRS, this did not pose a great problem. The acceptance of the FRS amounts to ±105 MeV/c in transverse momentum space for a beam momentum

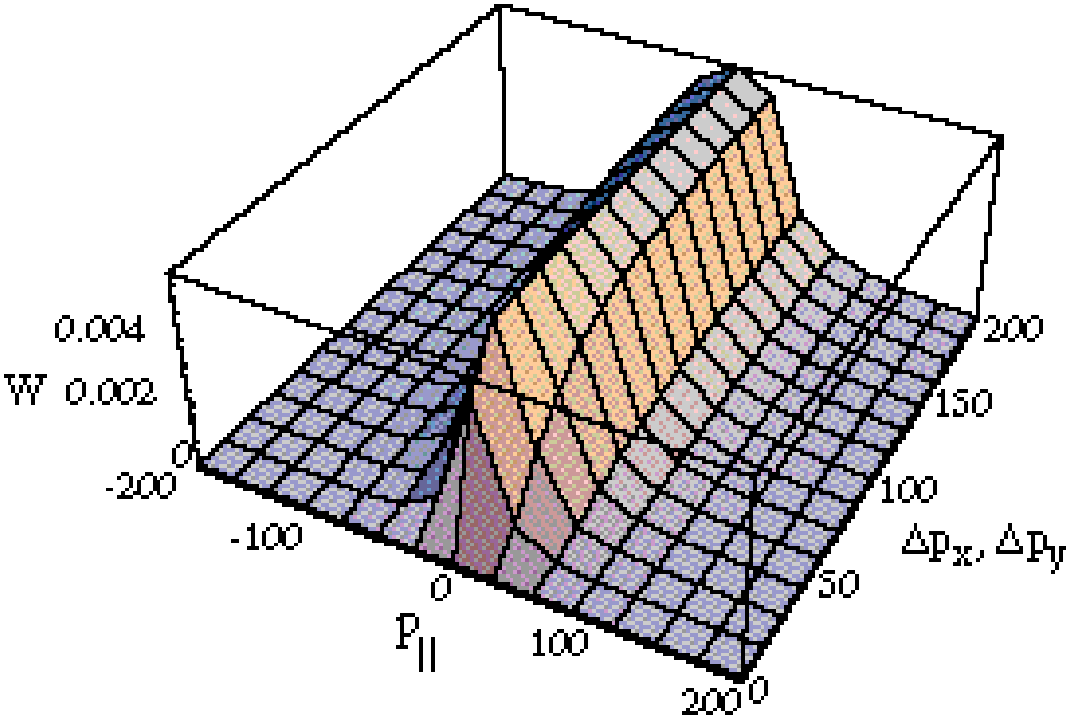

Fig. 5.11. Distortion of a Lorentzian-shaped longitudinal momentum distribution with FWHM = 47 MeV/c measured with limited transverse momentum acceptance.

of 777 MeV/c, as in the case of ^{11}Li. Fig. 5.11 shows the measured FWHM (Full Width Half Maximum) of a longitudinal momentum distribution as a function of the transverse momentum acceptance for a Lorentzian longitudinal distribution with originally FWHM = 50 MeV/c. In the limit of zero acceptance, i.e. $p_x = p_y \to 0$, the amplitude of the measured longitudinal momentum distribution becomes proportional to ε^2, which can be seen in fig. 5.11, but for infinitesimal values of ε the lineshape approaches $\mathrm{FWHM} = \Gamma\sqrt{\sqrt{2}-1}$. The FRS acceptance is large enough to only cause a minor distortion, a decrease of the measured width by 4 %.

5.6.2 Extracting fragment momentum distributions

The measured entity used for extracting transverse momentum distributions is the y-position in the MWDC-2. The bending in the ALADIN dipole magnet did not, in first order approximation, disturb the ion track along the y-direction. If the distance between the secondary target and the position sensitive detector as well as the beam momentum are known, the transformation to a momentum distribution is made by a scaling factor only after the wanted reaction has been selected by applying the conditions mentioned in section 5.5.

In reality, the extraction of the true momentum distributions was complicated by a number of effects; the divergence of the beam, the angular straggling in the target and the beam detectors and reactions not originating from the target. The divergence and angular straggling were handled by also studying the distribution of non-reacting ions. The background could be subtracted with help from the runs without a target.

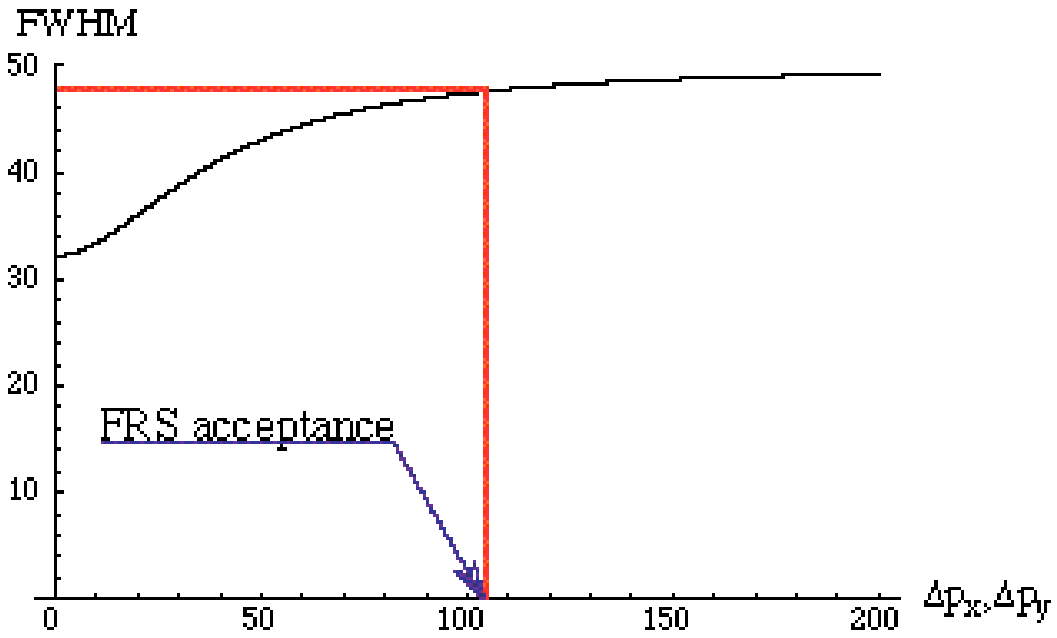

Fig. 5.12. Measured longitudinal momentum FWHM as a function of transverse acceptance for an originally FWHM = 50 MeV/c longitudinal distribution. The FRS acceptance is large enough not to critically influence the result.

The steps to obtain the final widths were as follows in the case of $^{8}\mathrm{He} \rightarrow {}^{6}\mathrm{He} + n + X$:

- Extract the ”raw” ^{6}He momentum distributions with and without target, using

$$p_y = p_0 \frac{(\mathrm{W2YPO} - \mathrm{W1YPO})}{d_2} \qquad \textbf{(5.14)}$$

  where p_0 corresponds to the momentum of the incoming beam and d_2 the mean distance between the target and MWDC-2. In first order approximation, the y-position in MWDC-2 is not affected by the bending in ALADIN, and by correcting for the y-position in MWDC-1, the effects of the size of the beam-spot are compensated. The usage of the y-position in MWDC-2 instead of MWDC-3 was because of better efficiency in the former detector plane, and the fact that the better angular resolution obtained from the latter, following from the larger distance, was not needed with the current limited counting statistics.
- Repeat for the non-reacting ^{8}He.
- By comparing the ^{8}He distributions with and without target, deduce the effect of angular straggling in the target. According to **(2.5)**, the typical deviation angle is $\propto p^{-1}$ for nuclides with the same charge and velocity. This means that the broadening in momentum space is the same for ^{6}He and ^{8}He.
- Fold the ^{6}He distribution without target with the deduced angular straggling.
- Subtract, with correct scale factors, the folded distribution without target from the distribution measured with target.

- The momentum distribution is obtained by fitting the resulting ^{6}He distribution with the appropriate function folded with the lineshape of the non-reacting ^{8}He.

The treatment differed somewhat for the different ions measured, in the case of ^{8}He a Gaussian lineshape was found to describe the data well which made the treatment straightforward. The broadening of the ^{6}He distribution without target was made by folding in an appropriate Gaussian, and the final width of the distribution could be obtained by quadratically subtracting the σ:s according to

$$\sigma_{^{6}\mathrm{He}} = \sqrt{\sigma^2_{\mathrm{measured}} - \sigma^2_{\mathrm{straggling}}} \qquad \textbf{(5.15)}$$

When analysing the ^{11}Li data, a more sophisticated treatment was necessary as the ^{9}Li distributions were more accurately described by Lorentzians. The non-reacting ^{11}Li was also not that well described by a simple Gaussian. In this case, the actually measured ^{11}Li distribution was used. This distribution was, for every step in the fitting process, mathematically folded with a Lorentzian. The resulting distribution was then compared with the measured distribution and the parameters of the Lorentzian accordingly varied. This kind of fitting process naturally consumes a large amount of computing power.

5.6.3 Extracting neutron momentum distributions

The procedure of extracting single neutron distributions from the reaction $^{8}\mathrm{He} \rightarrow {}^{6}\mathrm{He} + n + X$ was easier than for the charged fragments. The three-dimensional position information from the LAND detector was simply recalculated into radial momentum, using the formula

$$p_r = p_0 \frac{\sqrt{(\mathrm{NX} - \mathrm{W1XPO})^2 + (\mathrm{NY} - \mathrm{W1YPO})^2}}{d_{\mathrm{LAND}} + \mathrm{NZ}}, \qquad \textbf{(5.16)}$$

compensating for the size of the beam spot. Here, the distribution is integrated along the beam axis only. The position information could also be used to extract the projected momentum distributions in the x- and y-directions.

6. Results and conclusions

6.1 The cross-talk measurements

Two important conclusions could be drawn from the cross-talk experiments;

- The probability of cross-talk was small enough not to severely influence the results reported in refs. [6,59,77].
- For this range of neutron energies (≈14 MeV), the Monte-Carlo code Menate delivers correct estimations for the cross-talk probability. Most geometries can thus be modelled during the planning stage.

Recently, an attempt to verify the code for low-energy neutrons was made at Chalmers University of Technology [90]. Here a ^{252}Cf fission source is used, which has an average neutron multiplicity of 3.77. The energy distribution of the neutrons ranges from zero to about 15 MeV (with a steep decrease in intensity above 1 MeV), and the energy of each incoming neutron is measured by means of time-of-flight, where a gamma ray from a fission fragment is used as time reference. See fig. 6.1. To avoid effects from angular anisotropy in the true neutron-neutron coincidences, the opening angle θ between the detectors is kept constant and only the distance between the source and detector B is varied.

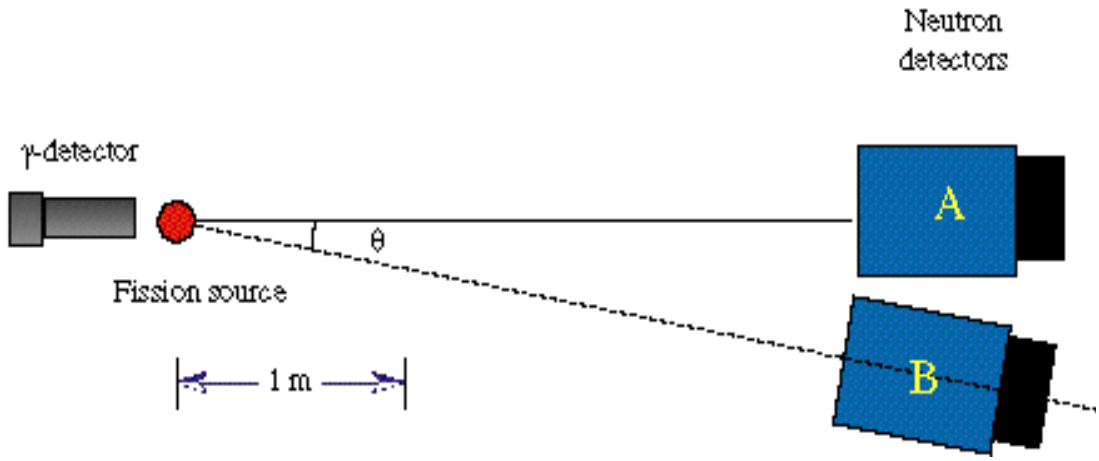

Fig. 6.1. The set-up used for measuring cross-talk for low-energy neutrons. The gamma rays from the fission process are used as time reference for determination of the energy of the neutron by time-of-flight. Detector B is positioned along the dashed line in a number of positions.

The data were not good enough to qualitatively determine the rate of cross-talk for low energies, but true cross-talk events could be identified unambiguously in the analysis, demonstrating the feasibility of the method. The long-term stability of the electronics set-up is a major problem here, as the count-rate of interesting events from a fission source that can be handled without extreme radiation precautions is very low.

Another possibility would be to use the neutron generator described in section 3.1.2 with a moderator enclosing the production target. This would have a suitable thickness for moderating the neutrons down to typical energies of 1 MeV. The energy for each neutron could then be deduced by TOF measurements, as the ”random walk”-path in the moderator is negligible compared to the total flight path.

Hopefully, the validity of the Menate code could thus also be verified for neutrons at the low-energy threshold of this type of detectors, making cross-talk estimations a computer task only in the future.

6.2 ^{6}He

By looking at the chart of nuclides, strong paring effects in the helium isotopes are found as ^{6,8}He are particle-stable but ^{5,7}He are not. The nucleus ^{6}He is found to be a two-neutron halo nucleus, with rather low two-neutron separation energy (0.973 MeV). The ^{4}He + n + n configuration has been calculated microscopically and the wavefunction is well established [29].

6.2.1 Decay properties

The ß-decay of ^{6}He was studied at ISOLDE with the set-up described in paper II and section 4.3. The lower limit of the branching ratio for ß-delayed deuteron emission was previously measured to be $(2.8 \pm 0.5)\cdot 10^{-6}$ [23]. In that experiment, ß-delayed deuteron emission was found for the first time. The current set-up was more insensitive to the position of the deposited radioactivity in terms of efficiency, though the low-energy cutoff was similar. This led to the revised value of $(7.6 \pm 0.6)\cdot 10^{-6}$ for deuterons above 360 keV.

The level scheme of ^{6}He and daughter nuclei is shown in fig. 6.2. In paper II two alternative decay routes (shown in fig. 6.3) are discussed; a) the conventional involving a direct decay to the continuum and b) a scenario where the particle emission, through a virtual state, takes place before the ß-decay. The inclusion of the latter process makes it possible to reproduce the absolute intensity of ß-delayed deuteron emission, but it is crucial to have a large overlap between ^{6}He and a configuration containing a 4 % admixture of an α-particle and a dineutron for this path to be present.

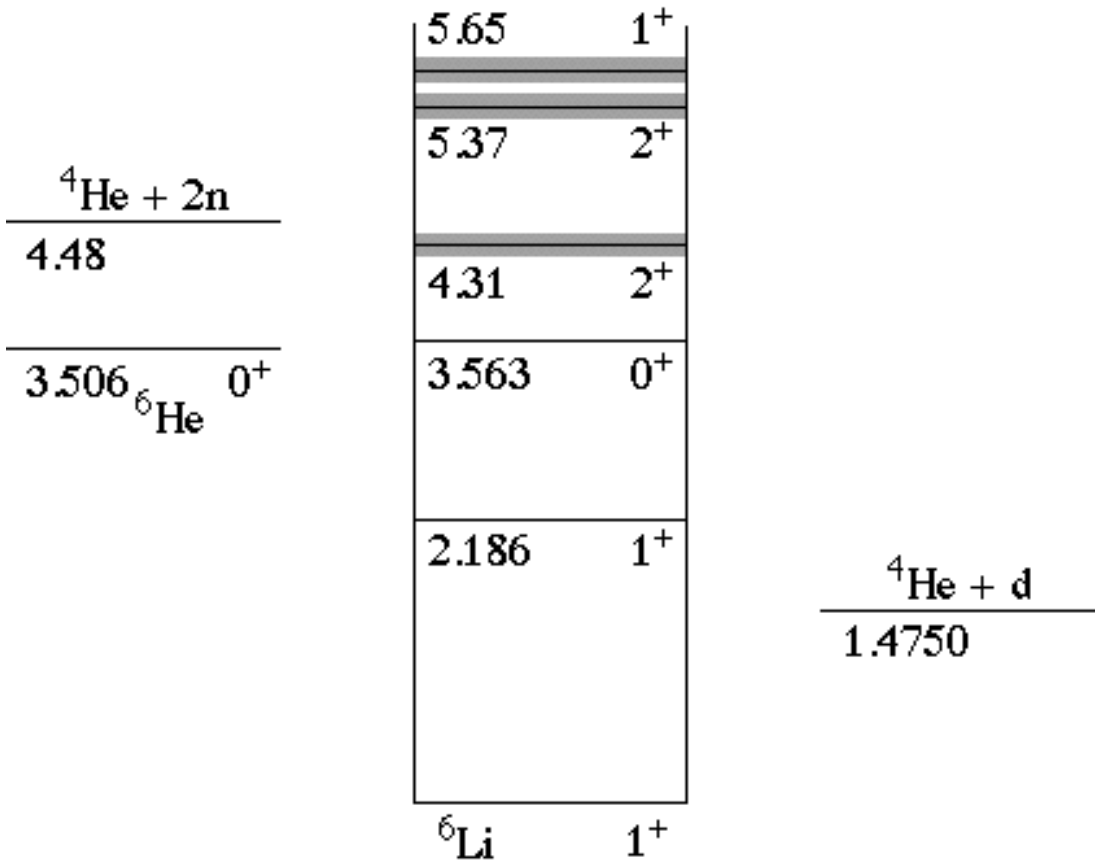

Fig. 6.2. Decay scheme of the ^{6}He ß-decay daughter ^{6}Li. The grey areas indicate broad levels.

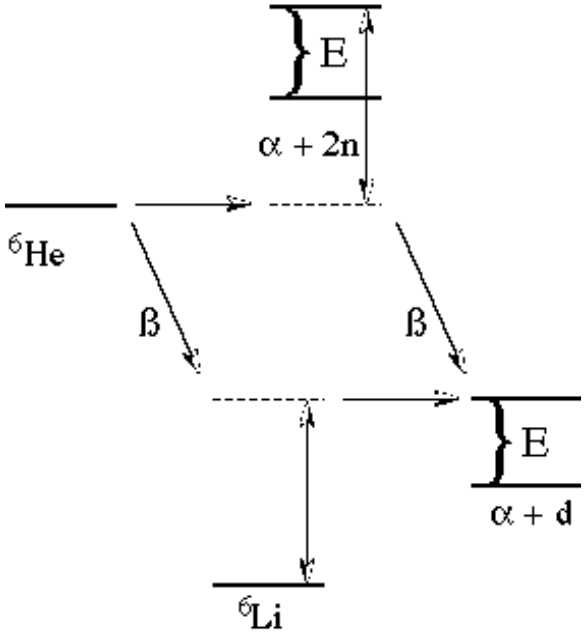

Fig. 6.3. Alternative decay routes for emission of deuterons from the ß-decay of ^{6}He. From paper II.

6.3 ^{8}He

The nucleus ^{8}He is the most extreme nucleus with respect to the ratio between neutrons and protons that is still particle stable, with A/Z = 4. The two-neutron and four-neutron separation energies of 2.14 MeV and 3.11 MeV respectively indicate that the true picture of ^{8}He is not a two-neutron halo nucleus, but an α-particle surrounded by four neutrons. The total interaction cross section and 2n- and 4n-removal cross sections lead to the same conclusions [32]. Zhukov et al. [91] have calculated the spatial angular correlations of the four outer neutrons with the COSMA method and show that the simple geometrically symmetric configurations shown in fig. 6.4 have maximum probability.

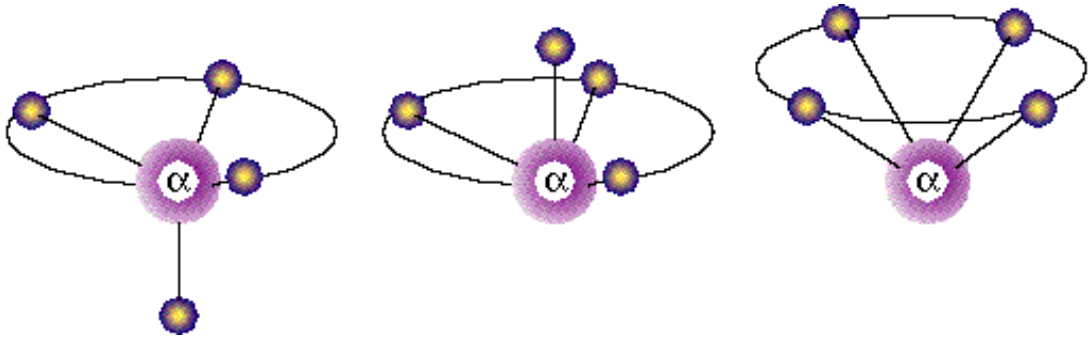

Fig. 6.4. Geometrical configurations according to maximum probable spatial angular correlations of the four outer neutrons in ^{8}He. From ref. [91].

6.3.1 Decay properties

The decay properties, regarding ß-delayed charged particle emission, of ^{8}He was investigated in paper II. The decay scheme is shown in fig. 6.5. The feeding of the 9.3 MeV excited level in the daughter nucleus ^{8}Li energetically permits ß-delayed triton emission either through the ^{5}He + t or ^{4}He + t + n channels. The high B_{GT}-value of this transition indicates a large overlap between the wavefunction of the ^{8}He ground state and the 9.3 MeV excited state in ^{8}Li, and the high branching ratio for subsequent triton emission implies strong three-nucleon correlations in the daughter state.

6.3.2 Reactions with ^{8}He at 240 MeV/u

The GSI experiment described in section 5 gave the possibility to measure two-neutron removal cross sections for reactions on lead and carbon targets. The cross sections are given in table 6.1, though the poor statistics for the lead target renders the

	σ_{-2n} (b)
C-target	0.27 ± 0.03
Pb-target	1.0 ± 0.7

Table 6.1. Two-neutron removal cross sections for 240 MeV/u ^{8}He on carbon and lead targets.

^{8}He

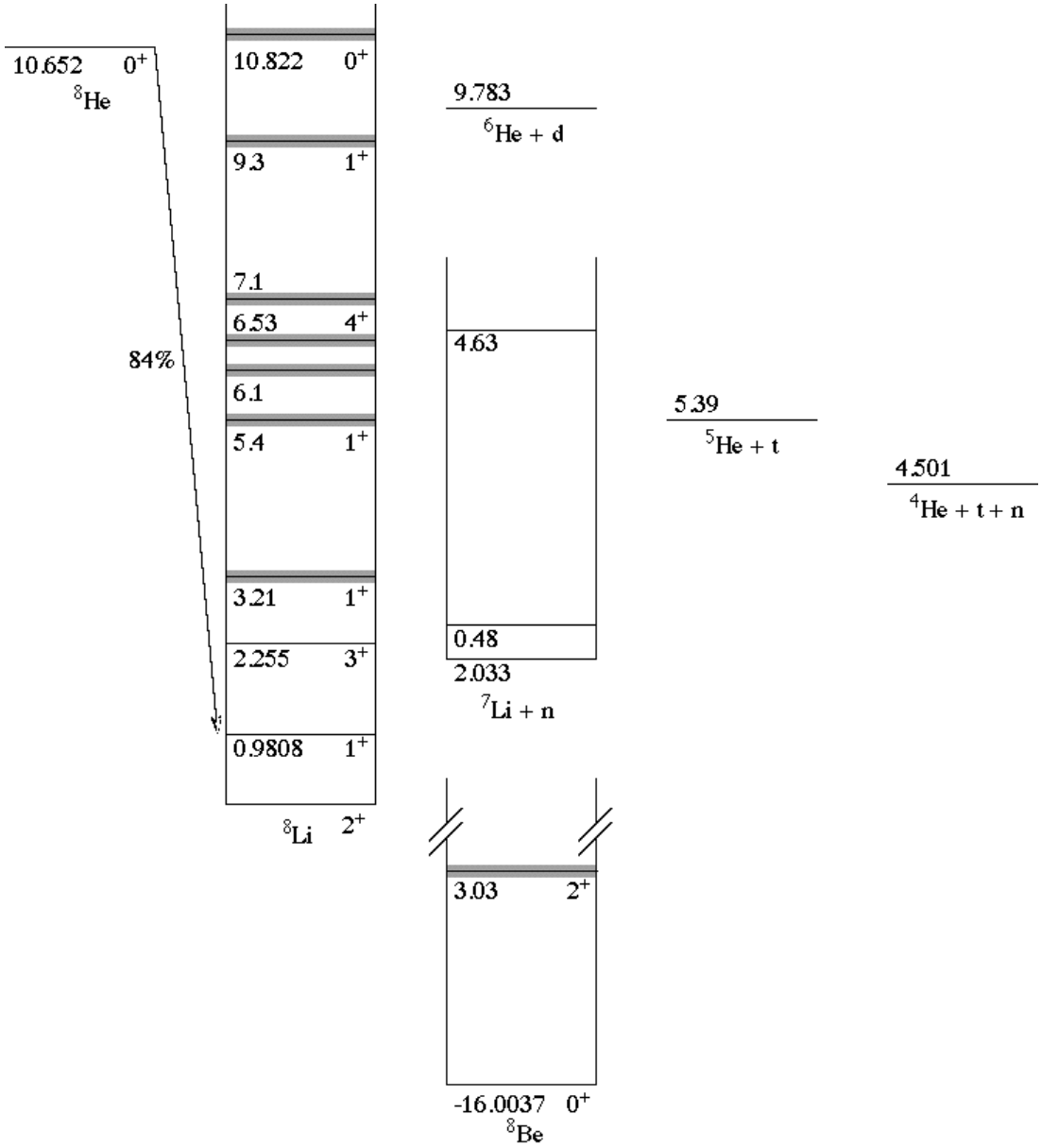

Fig. 6.5. Decay scheme of ^{8}He and daughter nuclei.

measurement a limited value. In ref. [94], other cross-section values, from the same experimental set-up were presented. The discrepancy stems from a further refinement in the treatment of the raw data, leading to a considerable loss of statistics and a more strict application of the selection cuts in the isotope separation- (A/Z-)plots (see fig. 5.10). The transverse neutron and ^{6}He momentum distributions were extracted for the carbon target only, due to insufficient statistics on the lead target. The extracted distributions were fitted with single Gaussian lineshapes, which described the distributions better than a single Lorentzian. The neutron distribution was extracted as a radial distribution, with only an integration along the beam axis made (according to section 5.6.1), but also as a doubly integrated distribution. The momentum distribution of the charged fragments was extracted from the neutron-coincident data in order to enhance the counting statistics as the non-coincident data were subject to scale-down in the acquisition. However, a fragment distribution of equal width, within the

error bars, but with less statistics is obtained when no neutron coincidence is demanded. The widths are given in table 6.2 and the distributions are shown in fig. 6.6.

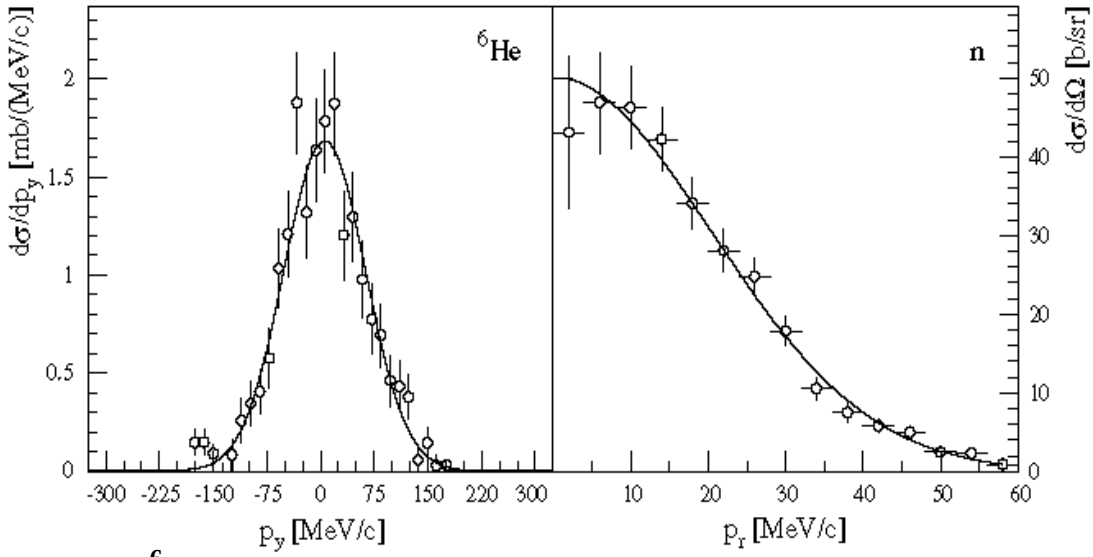

Fig. 6.6. ^{6}He (transverse) and neutron (radial) momentum distributions from the reaction ^{8}He → ^{6}He + n + X. The distributions were fitted with single Gaussian distributions.

	σ_{Gauss} (MeV/c)	FWHM (MeV/c)
n	20.5(21.2) ± 1.5	48.2 ± 3.5
^{6}He	56 ± 3	132 ± 7

Table 6.2. Widths of the neutron and ^{6}He momentum distributions from break-up of ^{8}He.

The three-dimensional position information from the LAND detector made it possible to extract the radial momentum distributions but also the momentum distributions projected on the x- and y-axis. According to section 5.6.1, the width of a Gaussian-like distribution is not affected by one or two integrations. Thus, by comparing the different projections, some conclusions about the lineshape can be drawn. The result of a Gaussian fit of the x-projection is given within the parenthesis in table 6.2, giving the same result within the error bars.

A compilation of the measured widths at various beam energies is shown in fig. 6.7. A trend towards broader distributions at high energies is seen, both for the charged fragments and the neutrons, similar to what is found for ^{11}Li [47]. A simple break-up scenario within the Serber model cannot take such an energy dependence into account. An attempt to find ways of describing the phenomenon is made in paper VI, assuming two different break-up scenarios, through the ^{7}He resonance by scattering of one of the four outer neutrons, or by populating an excited 2^{+}–state in ^{8}He above the

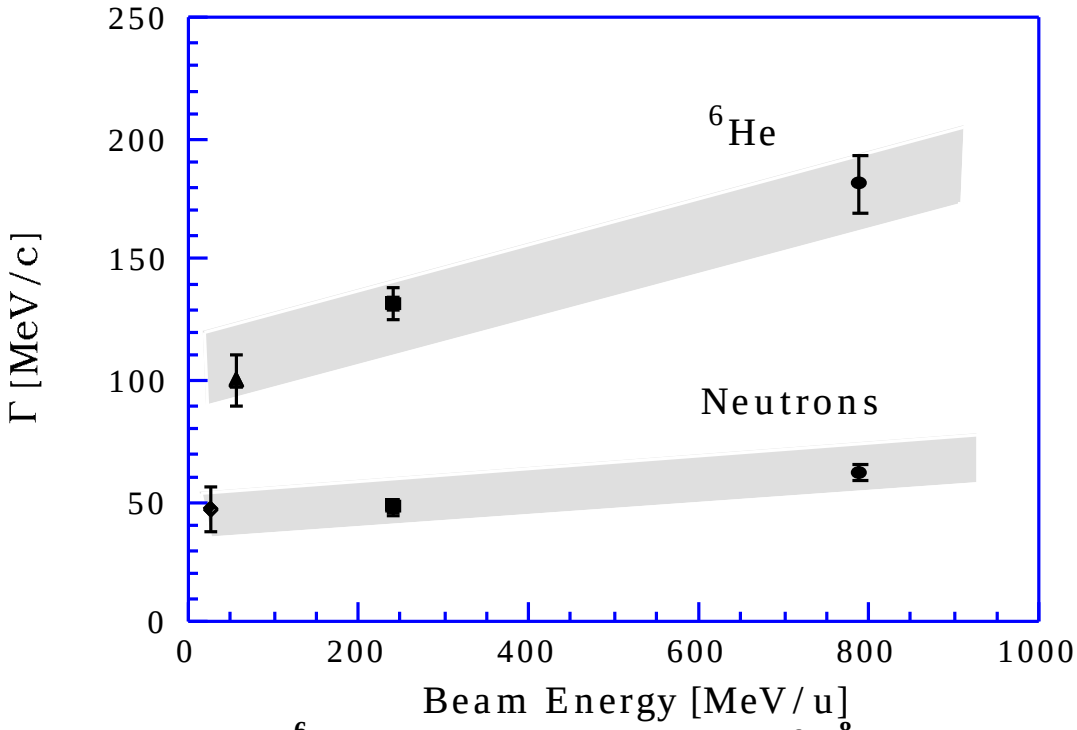

Fig. 6.7. Measured ^{6}He and neutron momentum widths for ^{8}He on a light (Be, C) target for a range of beam energies. The values are given as Full Width Half Maximum. Values from paper VI (squares), [38] (circles), [92] (triangle) and [93] (diamond). From paper VI.

^{6}He + 2n threshold. The probability for the latter process is supposed to cease with increasing energy. An admixture of 30 % for this reaction channel makes it possible to reproduce the ^{6}He momentum distributions, but still yields a too broad distribution for the neutrons. Furthermore, the measured neutron multiplicity is not compatible with a large admixture of the ^{8}He*-reaction channel where both of the dissociated neutrons are expected to lie within the acceptance of the neutron detector.

Fig. 6.8 shows the relative number of neutrons detected in the neutron detector LAND in halo-removal reactions of ^{11}Be, ^{8}He and ^{11}Li on lead and carbon targets. The values are corrected for the detection and track identification efficiency for 1n- and 2n-events. In the case of ^{8}He, the acceptance of the neutron detector amounts to $|p_{\perp}| < 60\text{MeV/c}$. The average measured neutron multiplicity is 0.89, indicating that one of the dissociated neutrons either gets absorbed in the target or frequently escapes the solid angle coverage of the detector. The second case would indicate that one neutron is emitted according to a broad distribution stemming from the break-up process.

6.3.2.1 Other reaction c hannels?

Why only study the $^{8}\text{He} \rightarrow {}^{6}\text{He} + n + X$ reaction channel? Figure 6.9 is taken from a GEANT-tracking through the ALADIN dipole magnet. The experimental set-up was optimized for studying the reaction $^{11}\text{Li} \rightarrow {}^{9}\text{Li} + \text{n} + \text{n}$ and had not high enough acceptance for studying other reaction channels than $^{8}\text{He} \rightarrow {}^{6}\text{He} + n + X$ in the case of ^{8}He. As can be seen in the figure, the centre of the α-particle distribution is com-

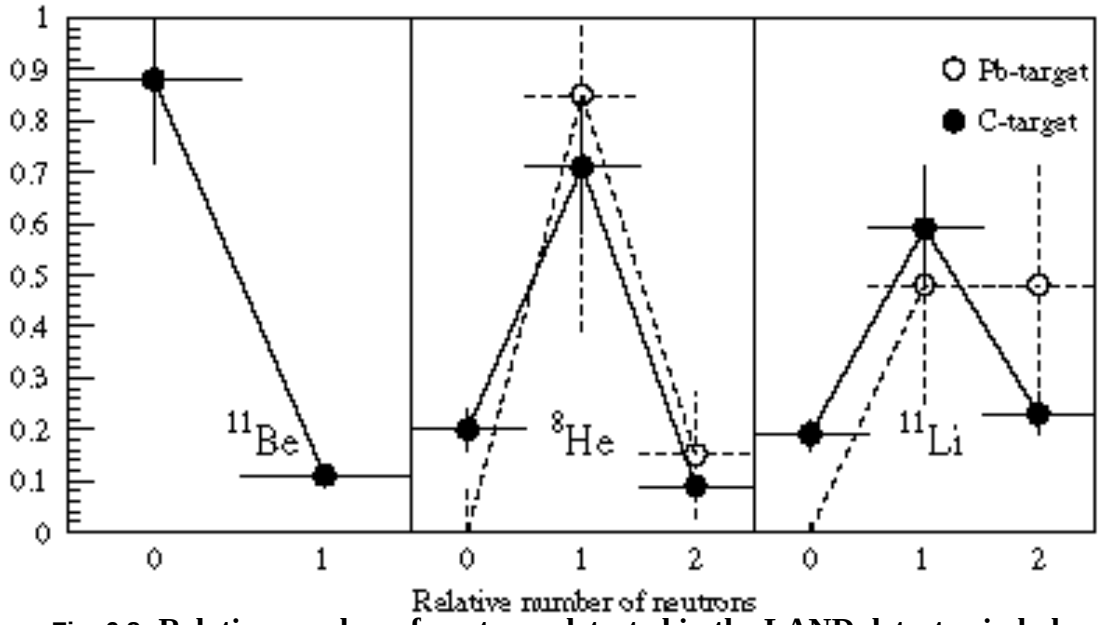

Fig. 6.8. Relative number of neutrons detected in the LAND detector in halo-removal reactions with ^{11}Be (460 MeV/u), ^{8}He (240 MeV/u) and ^{11}Li (270 MeV/u). The ”missing” neutrons are either absorbed in the target or subject to large-angle scattering, thus to a large extent escaping the detector coverage. From ref. [56].

pletely outside the active area of MWDC-2 and MWDC-3. The very interesting reaction channel $^{8}\mathrm{He} \rightarrow {}^{4}\mathrm{He} + n + X$ is thus inaccessible in this experiment.

An unambiguous identification of fragments with Z=1 (i.e. tritons) could not be made either since the signals in the plastic wall were too small. In the case of ^{8}He, this meant that no core removal reactions could be studied.

6.4 ^{11}Li

6.4.1 Decay properties

The most apparent probe of the halo structure in ^{11}Li that can be used in decay studies is the peripheral ß-decay shown in fig. 1.7, where the ^{9}Li + n + n system decays into a ^{9}Li + d system. This is elaborated in [95], stating that the ß-decay matrix elements are determined practically by the halo part of distances $R \geq 4$ fm

As can be seen in the decay scheme shown in fig. 6.10, a multitude of decay channels are open to the decay of ^{11}Li into states in ^{11}Be. As discussed in section 4.1.1, the B_{GT}-value for decay to the 18.5 MeV excited state in ^{11}Be was based upon the triton branch only. A summation of all possible branches is experimentally a very difficult task, but the identification of the ß-delayed deuteron branch [11] using the improved gas-detector telescope increases the lower limit on the Gamow-Teller strength to the 18.5 MeV state, $B_{GT} \geq 1.2$. Corroborating evidence for ß-delayed deuteron emission was found by studying the shape of the energy distribution of the emitted Z = 1 parti-

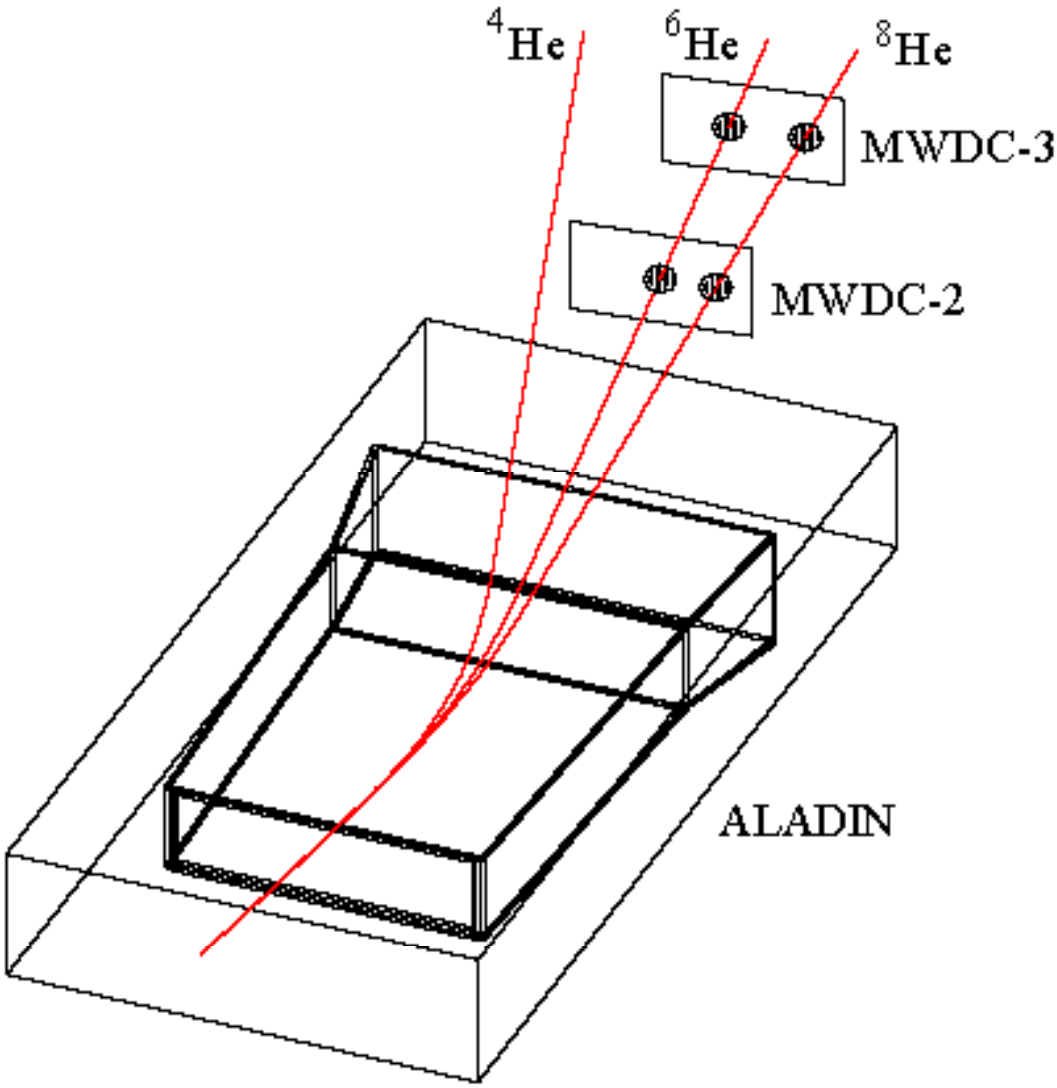

Fig. 6.9. Flight paths for three He-isotopes through ALADIN following the break-up of ^{8}He at 240 MeV/u. From paper VI.

cles, together with the existence of ^{9}Li manifested by half-life identification and energy distribution of α-particles characteristic for its decay. The data on ß-delayed neutrons are still under analysis.

6.4.2 Reactions with ^{11}Li at 280 MeV/u

6.4.2.1 Cross sections

The cross sections from the reaction ^{11}Li $\rightarrow$^{9}Li + X were obtained from the two set-ups at FRS and in cave B. The higher beam intensity made the results from the former set-up more reliable, though the latter yielded the same result within the error bars. The reaction cross sections are listed in table 6.3.

Additional to the halo-removal channel, a multitude of other reaction channels were detected within the acceptance of the ALADIN-LAND set-up. Most prominent is the channel ^{11}Li +Pb$\rightarrow$^{8}Li + X with a cross section of 0.47±0.16 b, but also charge-changing reactions take place.

^{11}Li

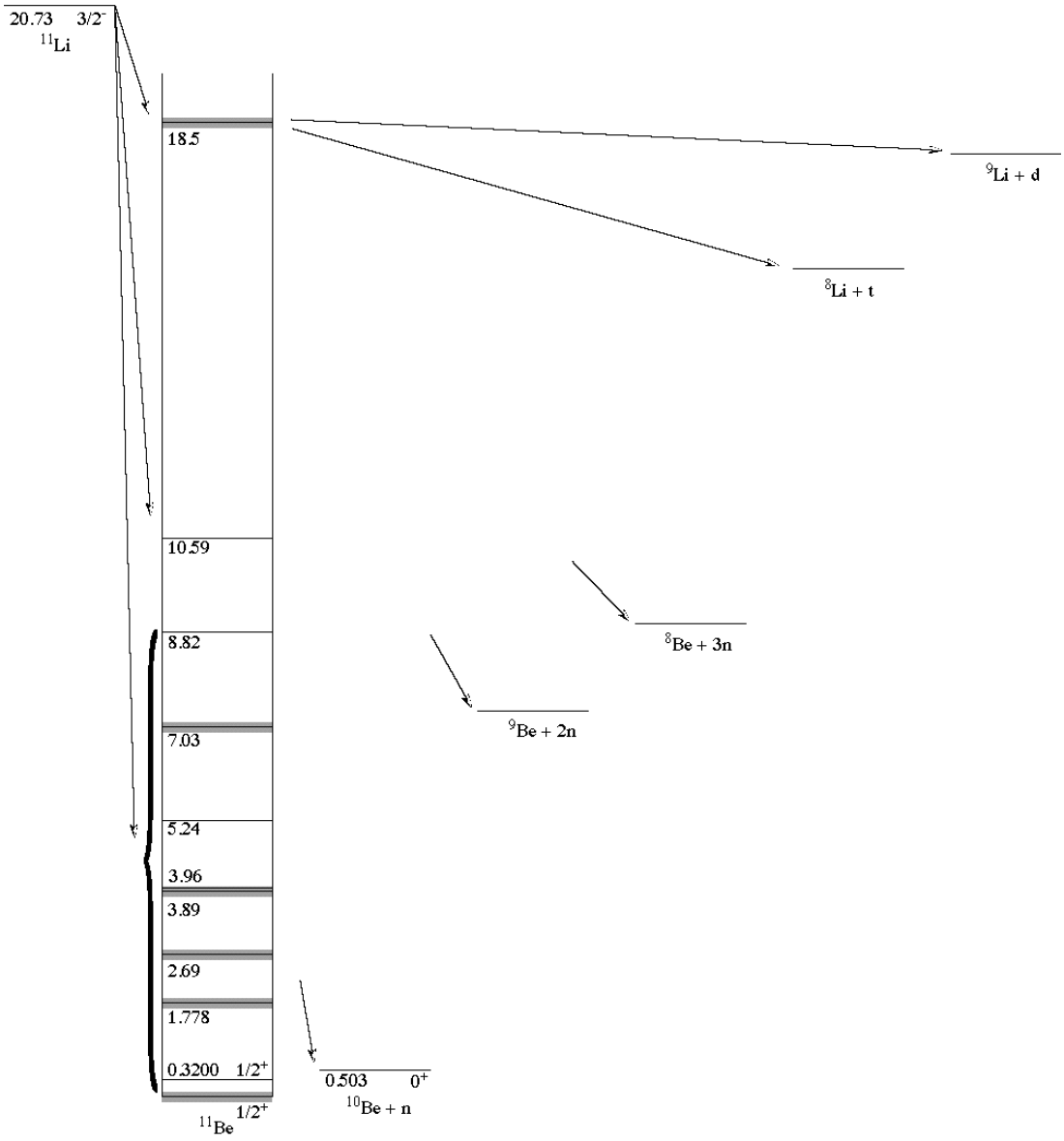

Fig. 6.10. Decay scheme of ^{11}Li. From ref. [96].

Target	σ_{-2n} (b) ALADIN-LAND	σ_{-2n} (b) FRS
C	0.26 ± 0.02	
Al		0.47 ± 0.08
Pb	1.9 ± 0.7	1.9 ± 0.4

Table 6.3. Two-neutron removal cross sections for ^{11}Li measured at 280 MeV/u

6.4.2.2 Momentum distrib utions - halo remo val

The obtained data are unique with respect to the completeness of the measurements, having measured longitudinal and transverse momentum distributions at the same energy and with large acceptances. The measurement with the FRS was performed with *one* Bρ-setting only, and as discussed in section 5.6.1 the acceptance should be sufficient to allow for the measurements to reflect the true momentum distribution. The transverse momentum distributions were extracted as described in section 5.6.2. The resulting distributions are shown in fig. 6.11. The shown distributions had to be unfolded from the different broadening effects not connected with the dissociation reaction. In both cases, the non-reacting ^{11}Li beam was used to deduce the influence of these effects. All distributions were fitted with Lorentzian functions where a folding with the *measured* experimental ^{11}Li-distributions was made. The decreasing longitudinal acceptance at the edges was mimicked by applying a linear decrease of the Lorentzian.

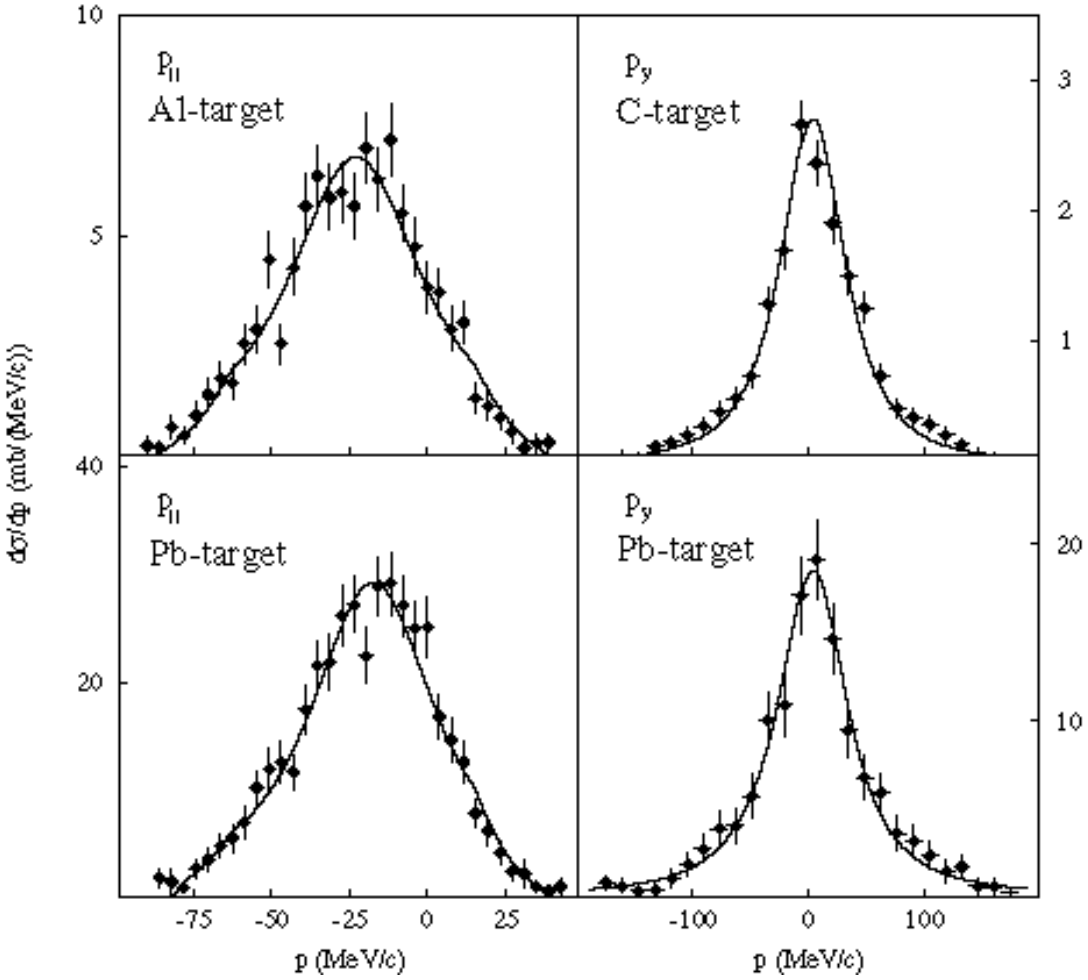

Fig. 6.11. Measured longitudinal and transverse momentum distributions from the reaction ^{11}Li → ^{9}Li + X at 280 MeV/u. From paper III.

The deduced widths of the measured ^{9}Li momentum distributions are listed in table 6.4. The remarkable thing here is the very similar value obtained, FWHM ≈ 47 MeV/c, regardless of light or heavy target and transverse or longitudinal momentum. The visual difference in fig. 6.11 between the transverse and longitudinal

momentum distribution stems from the different scales and the disparate folding functions. This similarity seems to be in conflict with the idea mentioned in section 1.4.2, that the longitudinal momentum distribution should be less affected by the break-up process. The transverse distribution should, at least for the lead target, be influenced by a Coulomb kick and thus be broader than the longitudinal. The underlying mechanism for the explanation given in paper III has already been touched upon; the core-break-up reactions. It appears that the ^{9}Li-core often does not survive collisions with impact parameters less than $b = R_C + R_T$ plus a few fermi. Thus, a depletion of the halo removal channel occurs for small impact parameters where the Coulomb broadening is significant. This idea finds support in a measurement done by Nakamura and collaborators [97] where the cross section of the halo removal reaction ^{11}Be + Pb $\rightarrow$ ^{10}Be + n + X decreased strongly for impact parameters below 12 fm and the relatively large σ_{-3n}-value given in section 6.4.2.1.

Distribution	Target (Thickness, g/cm^2)	Experimental FWHM (MeV/c)	Beam FWHM [a] (MeV/c)	Deduced FWHM (MeV/c)	χ_N^2 [b]
p_y	C (1.293)	72	41	45 ± 4	1.9
p_y	Pb (0.302)	73	42	49 ± 4	0.8
$p_{\|\|}$ [c]	Al (5.4)	54	15	49 ± 3	1.3
$p_{\|\|}$ [c]	Pb (8.0)	51	15	45 ± 3	0.9

Table 6.4. Momentum widths of ^{9}Li fragments after break-up of ^{11}Li.

a. The distributions have been integrated over two momentum directions meaning that the FWHM corresponds directly to the Γ parameter defined in eq. **(5.11)**.

b. Normalized $\chi 2$

c. The values refer to a coordinate system moving with the projectile

The neutron momentum distribution from the reaction ^{11}Li $\rightarrow$ ^{9}Li + n + X on a carbon target is shown in the lower part of fig. 6.14. All neutron momentum distributions were fitted with the radial (once integrated) Lorentzian function defined in eq. **(5.11)**. The results are shown in table 6.6.

Energy (MeV/u)	Reaction channel	Target	Γ (MeV/c)
280	^{9}Li	C	36 ± 6
280	^{9}Li	Pb	33 ± 4

Table 6.5. Measured Γ-values for neutron momentum distributions from halo removal reactions of ^{11}Li.

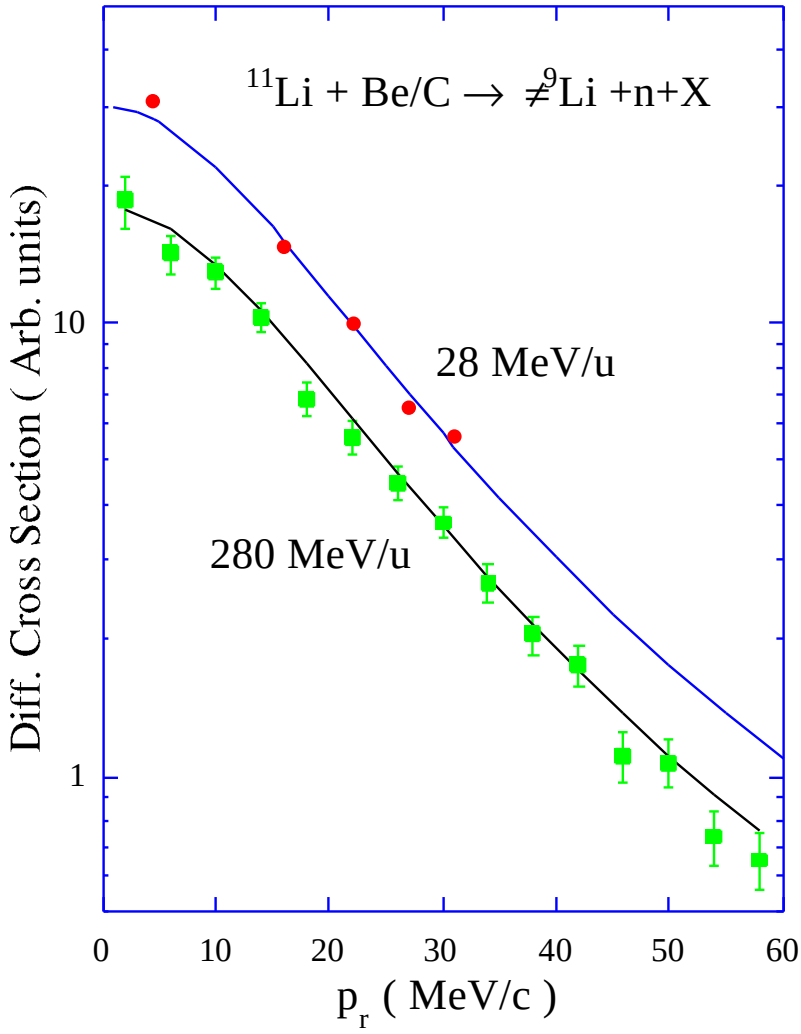

Fig. 6.12. Neutron transverse momentum distributions from the reaction ^{11}Li → ^{A}Z≠^{9}Li + n +X measured at 28 and 280 MeV/u. The data points stem from paper IV, the figure is taken from ref. [98].

6.4.2.3 Momentum distrib utions – core break-up

The physics of the core break-up reactions has been mentioned in section 1.4.7 and will be further discussed in the context of ^{11}Be (section 6.5.1). The neutron distributions were extracted with a condition ^{11}Li → (^{A}Z≠^{9}Li) + n +X in order to mimic the selection criteria used in the data at 28 MeV/u measured at GANIL. However, the acceptance of the MWDCs put a further constraint, A/Z>2.3, to the exit channels that could be studied. The results are presented in paper IV, and a striking resemblance of the widths measured at 28 and 280 MeV/u is found. See fig. 6.12. This is in contrast to the halo-removal data presented in fig. 1.16, indicating that the core break-up data might be less sensitive to the reaction mechanism and might thus carry more information about the true wavefunction of the halo neutrons. The widths are listed in table 6.6.

Energy (MeV/u)	Reaction channel	Target	Γ (MeV/c)
28	≠^{9}Li	Be	42±4
280	A/Z > 2.3, ≠^{9}Li	C	43±3
280	A/Z > 2.3, ≠^{9}Li	Pb	36±4

Table 6.6. Measured Γ-values for neutron momentum distributions from core break-up reactions of ^{11}Li.

6.5 ^{11}Be

6.5.1 Reactions with ^{11}Be at 460 MeV/u

In fig. 6.13, the transverse momentum distributions for neutrons from three different reaction channels are shown. The widths of the neutron distributions, fitted with a simple Lorentzian, are listed in table 6.7 for a beam of ^{11}Be impinging upon a carbon target.

Reaction channel	Γ (MeV/c)	Physical relevance
^{10}Be	98 ± 5	Reaction mechanism
^{7}Li	67 ± 5	Halo momentum
^{9}Li	36 ± 3	^{10}Li resonance

Table 6.7. Widths of the neutron momentum distributions following break-up of ^{11}Be on a carbon target into various reaction channels.

6.5.1.1 Halo remo val, ^{11}Be → ^{10}Be + n + X

The halo removal reaction in ^{11}Be has been considered as an ideal test case for gaining further understanding of the reaction processes involved in dissociation of a halo nucleus [59,77]. This is, naturally, justified by the relatively simple ^{10}Be + n structure of the one-neutron halo system. Fig. 6.8 shows that the average detected neutron multiplicity in the halo removal channel is 0.10 only. This, together with the relatively large width of the neutron distribution, indicates that the halo neutron is either absorbed or diffracted in the break-up process and the measured distribution can thus tell us relatively little about the ^{11}Be ground state.

6.5.1.2 Core break-up, ^{11}Be → ^{7}Li + n + X

As previously argued, the halo particles might be less influenced by the break-up process in the events where the core is shattered into pieces. Here, the reaction channel ^{11}Be → ^{7}Li + n + X was chosen as it was well covered by the acceptance of the

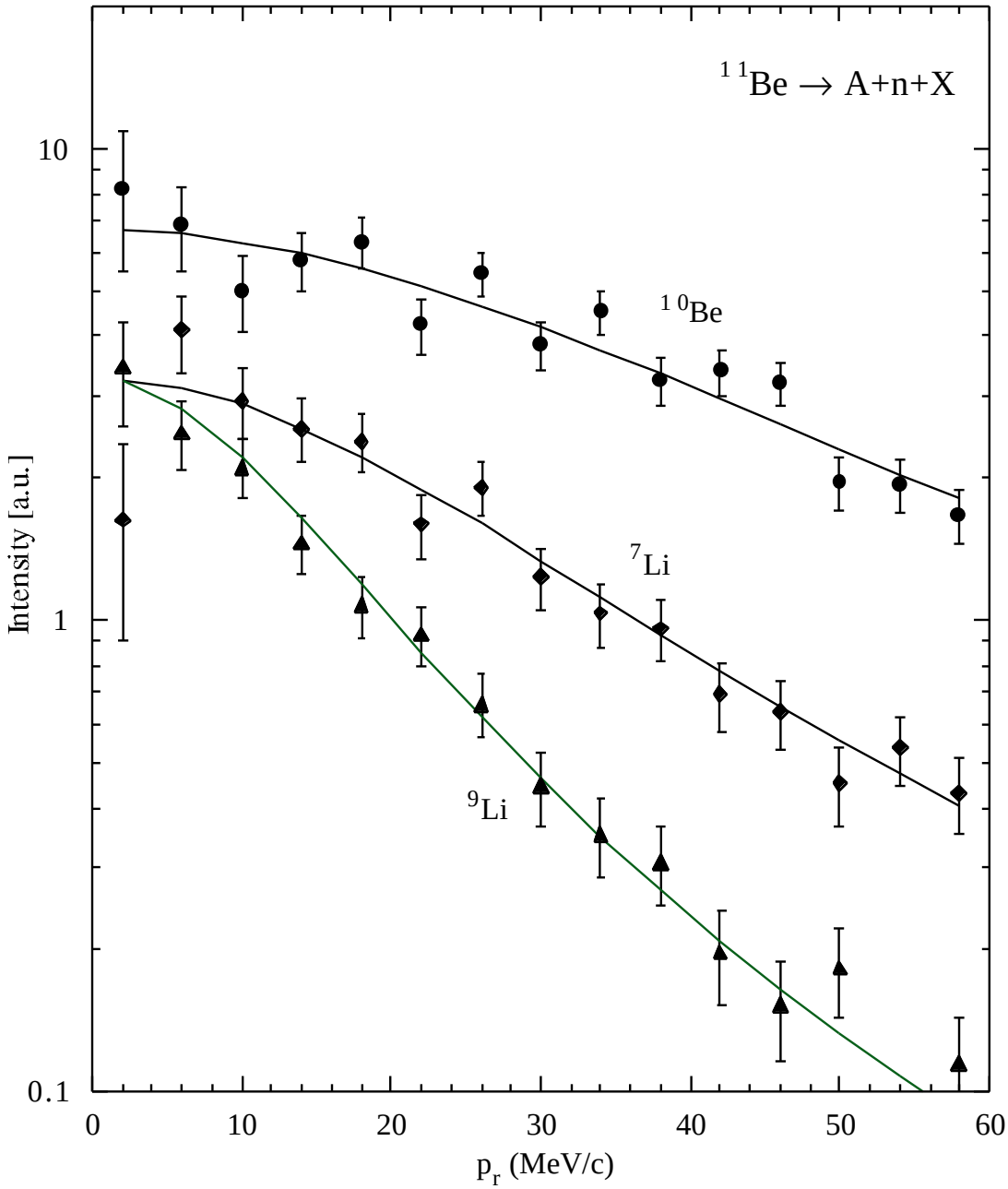

Fig. 6.13. Transverse momentum distributions for neutrons emitted in the reaction ^{11}Be → A + n + X on a carbon target. The data points denoted by circles, diamonds and triangles represent A = ^{10}Be, ^{7}Li and ^{9}Li respectively.

ALADIN-MWDC spectrometer. The channel ^{11}Be → ^{8}Li + n + X was also investigated and yielded a similar width, but this result was less reliable as the selection of ^{8}Li was influenced by non-reacting ^{11}Be. These two nuclides have similar A/Z relations, 2.67 and 2.75 respectively and thus the distributions in the spectrometer are overlapping. The problem cannot be completely resolved by a Z = 3 condition in the TOF-wall as a small amount of ^{11}Be ”leaks” through, which is enough to influence the much less abundant true ^{8}Li events. As the neutrons in coincidence with ions identified as ^{11}Be mainly stem from reactions in the beam detectors (MWDC-2,3, TOF-wall) following the ALADIN magnet, i.e. after the bending, the neutrons thus pro-

duced predominantly hit the half of the LAND detector situated closest to the TOF-wall. See fig. 5.4. By using the other half of the detector, opposite to the symmetry axis defined by the incoming beam, a low-statistics distribution could be extracted.

The persistence of the width of the momentum distributions when choosing different core break-up channels, together with the fact that the distributions are clearly narrower (see table 6.7) than the one obtained from the halo-removal channel (the ^{8}Li- and ^{7}Li-coincident distributions also have a small component of neutrons stemming from the core, with large width) indicates that the core break-up reactions give a more accurate picture of the true halo neutron momentum.

6.5.1.3 One-proton removal, ^{11}Be $\rightarrow$ ^{9}Li + n + X

The previously mentioned fact that the neutron momentum distributions are the same, regardless of which core break-up channel is selected, seems to be contradicted when the reaction channel ^{11}Be $\rightarrow$ ^{9}Li + n + X is considered. This is a quite specific process where only one of the core protons is extracted by the reaction, and the resulting momentum distribution is very narrow, Γ = 36 MeV/c. An attempt to explain this narrow width is illustrated in fig. 6.14. The measured momentum width resembles the result from ^{11}Li completely, indicating that the unbound nucleus ^{10}Li plays a key role in the A = 11 halo nuclei. By extraction of a proton from the ^{10}Be-core in ^{11}Be, a ^{9}Li + n system can be created. The same thing is likely to happen when one of the two halo neutrons in ^{11}Li is absorbed or diffracted in the target. This is anticipated for a light target according to fig. 6.8, where the average number of detected neutrons is 1.05. The implications of having the dissociation proceeding through the unbound ^{10}Li state is discussed further in paper V.

6.6 The future

6.6.1 π^0 production

A complementary way of studying the halo neutrons is to study the π^0-production when the halo neutrons hit a light target. An experiment aiming at this is proposed to take place at GSI, using the Crystal Ball, made of 162 NaI crystals which cover a solid angle amounting to 95 % of 4π. The 2-photon decay of the π^0 will be detected in coincidence with the core fragment and optionally neutrons [99]. If the beam energy is chosen close to the π^0-production threshold, the production rates are very sensitive to the internal momentum distributions of the target and projectile nucleons. However, it must be noticed that this method mainly probes the high-momentum components of the halo wave function.

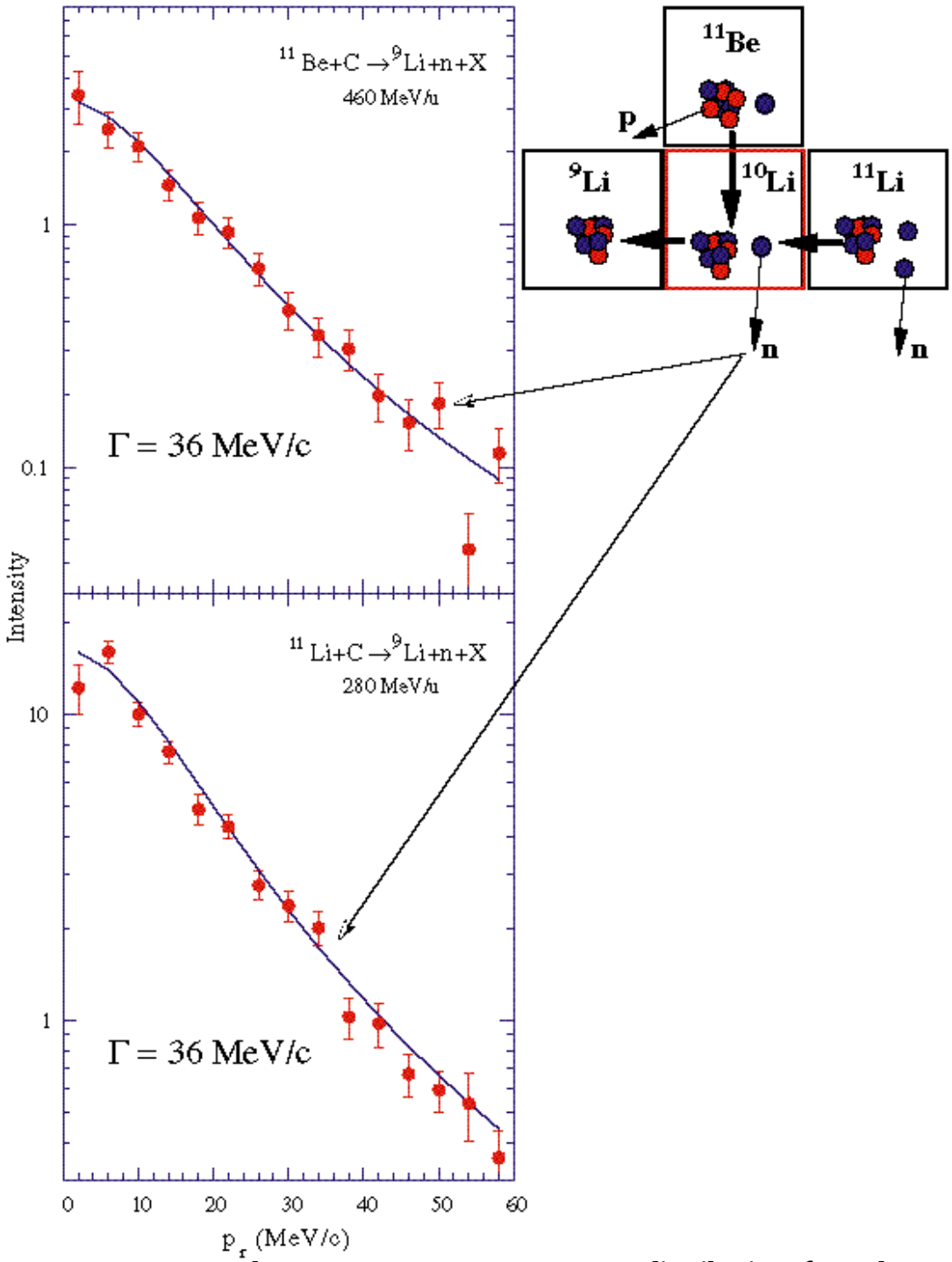

Fig. 6.14. Measured transverse neutron momentum distributions from the reactions ^{11}Be → ^{9}Li + n + X and ^{11}Li → ^{9}Li + n + X on a carbon target. The distributions resemble each other to a very high extent. An attempt to explain this is shown in the excerpt of the chart of nuclides in the upper right corner; the role of the unbound nucleus ^{10}Li. By extraction of a proton from the ^{10}Be-core in ^{11}Be, a ^{9}Li + n system can be created. The same thing is likely to happen when one of the two halo neutrons in ^{11}Li is absorbed or diffracted on the target.

6.6.2 New facilities

The measurements performed within the scope of this work had to a large extent been impossible to carry out only one decade earlier. It is apparent that the large investments that have been made in radioactive-beam facilities has propelled the physics of exotic nuclei to new heights. What can then be expected in the near future? Some radioactive-beam projects in various states of preparation will be mentioned here;

6.6.2.1 Postacceleration of radioactive beams

The fragment-separator type of radioactive beam facility is in many respects the most versatile one, as almost every nuclide can be produced in the process of fragmenting the primary nuclei regardless of the chemical properties. However, the demand for a relative thin production target in order to not severely disturb the beam characteristics does limit the production rate. The only way of increasing the yield is to increase the primary beam intensities, which is not always feasible. Another drawback is the limitation to high and intermediate beam energies, excluding experiments close to the Coulomb barrier which are of great interest.

The ISOL-type facilities have much larger production yields for a number of nuclides, but the multi-step process of extraction and ionization imposes limits to the shortest half-lives that can be studied. Furthermore, the beam transport system is usually limited to some tenths of keV, an energy not useful for reaction studies. However, the target fragmentation/spallation method is the basis for a number of new machines recently brought to operation or being in the planning state. Since 1992, the ARENAS^3 [100] facility in Louvain-la-Neuf is operating. Here, a primary beam of 30 MeV protons is accelerated by a small cyclotron and hits a production target. The produced radioactive nuclei are ionized, separated and subsequently accelerated to a few MeV/u in a second cyclotron. Although the beams that can be produced here are limited to light nuclides, the facility opens up possibilities of studying several interesting astrophysical aspects, in particular by measuring (p,γ) cross sections via inverse kinematics in a new energy region.

The existing ISOLDE at CERN will soon be upgraded with a postaccelerator in order to facilitate a proposed experiment, REX-ISOLDE [101], to study very neutron-rich Na-Mg and K-Ca isotopes. An ion source for reaching high charge states will be installed at an existing beam line and will be followed by a acceleration structures and experimental stations. Here, a multitude of studies in the energy region 0.8 - 2 MeV/u will become possible, e.g. elastic scattering experiments with inverse kinematics.

Another future large radioactive-beam project that has been approved is the SPIRAL facility at GANIL [102]. Here, the secondary beams will be created in heavy-ion collisions with a heavy (e.g. uranium) target. The primary beam can be varied within the currently available range at GANIL with respect to energy and ion species, for ^{12}C up to 95 MeV/u. The use of a primary HI beam is supposed to grant a higher yield and selectivity than a proton beam for a number of interesting nuclides. Following the production target and ion-source, a secondary beam line with a spectrometer for first level separation transports the created ions to the medium-energy ions cyclotron CIME. This new accelerator will be built with an available energy range of

$T/A = 2 - 25$ MeV/u $(K = 265, T = KZ^2/A)$ and will deliver secondary beams to the experimental areas via the existing α-spectrometer.

6.6.2.2 Developments of the production process

If the production target in subject to an intense flux of thermal neutrons, a number of neutron-rich nuclei with masses between 75 and 150 can be produced by fission. The neutrons from a nuclear reactor is thus suitable as primary ”beam” and the fission target is placed inside the reactor shielding, close to the reactor core. The OSIRIS facility in Studsvik, Sweden operates in this mode. In Grenoble, a similar facility is projected, the PIAFE project [65], using the intense neutron flux (10^{14} s^{-1} cm^{-2}) from the ILL in order to create fission reactions. The ions can subsequently be transported to the existing SARA cyclotron and accelerated to 2 – 10 MeV/u.

The intensity of the secondary beams is the main bottleneck when high statistics and new drip-line nuclei are wanted. In order to increase the production rate, the intensity of the primary beam must be raised, leading to heating problems in the production target. A programme aiming at future use of higher primary-beam intensities is the RIST (Radioactive Ion-Source Test) project at Rutherford Appleton Laboratory, using 800 MeV protons [103]. Here, the production target consists of thousands of thin, stacked tantalum foils arranged in order to maximize the heat dissipation. The goal is to develop a production target that can withstand beam powers 100 times larger than at ISOLDE-PSB.

6.6.2.3 Exotic nuclei - electron collider

A very ambitious project is being planned at RIKEN, Japan, called the RI (Radioactive Ions) Beam Factory [104]. It utilizes a double storage ring MUSES (Multi-USe Experimental Storage-rings) for radioactive beams together with a storage ring for electrons. Beam energies ranging to 600 MeV/u for light beams and 150 MeV/u for uranium beams are planned. The radioactive beams will be able to collide with other heavy ions or electrons, and by running the storage rings in the same direction, in merging mode, reactions with low relative energy can be studied.

6.7 Final remarks

As I have been trying to show, in a rather fragmented way, the research regarding halo nuclei and other exotics along the neutron drip line is a highly active and diversified field. The development of the insight is fast, and many views believed to be true some years ago are now reduced to be regarded as inceptive in the best case. A similar future development can thus be expected. However, though our understanding has increased drastically, the picture we have of these nuclei is to a large extent phenomenological. There is no theory having true predictive power, like the shell-model for ”normal” nuclei, that is applicable for nuclei at the drip line, though there should be no doubt that our fellow theoreticians are hunting it with full force. One important key to further understanding lies in obtaining experimental data of higher quality. The currently existing data are often poor, concerning resolution and most frequently regard-

ing counting statistics. An experiment like the one at GSI described in section 5, measuring the break-up remnants with good resolution and efficiency/solid angle coverage has the ability to reveal a multitude of interesting new physics. In reality, the experiment suffered from low intensity of the secondary beams and the extracted results were to some extent found wanting.

However, during this work a number of interesting new pieces in the halo puzzle has been found. The cross-talk measurements are not directly related to the halo nuclei, but are important in order to improve the credibility of the experiments measuring neutrons. The new branching ratios for ß-delayed deuteron and triton emission from ^{6}He and ^{8}He respectively have yielded new ideas about the structure of these nuclei. The data taken at GSI have given a multitude of new information regarding momentum distribution widths, shapes and reaction cross sections. The parts that can be singled out is the persistency, regardless if measured in the longitudinal or transverse direction, of the momentum distribution of ^{9}Li from break-up of ^{11}Li, the revelation of the role of the reaction mechanism seen in the neutron momentum distributions stemming from ^{11}Be, the possible beam-energy insensitive results from core-removal reactions, and the role and structure of the ^{10}Li-resonance deduced from single-particle removal reactions.

”He rests. He has travelled.”

James Joyce, ”Ulysses”

7. Acknowledgements

First I would like to thank Göran Nyman for being a superb supervisor, in every respect. His outstanding qualities as a physics tutor, colleague and fellow human have made the work together with him a real pleasure. Furthermore, he possesses invaluable organizing and administrative skills which I, and many others, have greatly benefited from.

Prof. Björn Jonson for creating a very stimulating research enviroment at Chalmers University of Technology, for his never-ending curiosity and enthusiasm regarding physics which has been most inspiring and for numerous valuable discussions. He has also given me the ability to spend a large part of my time as a PhD student at laboratories abroad, which has been extremely rewarding in many respects.

Thanks to the present and former people of the Subatomic Physics group in Göteborg for generating a good-humoured and creative atmosphere to work in.

Special thanks to Prof. Dr. Dr. Achim Richter and Dr. Gerhard Schrieder at TH-Darmstadt for good cooperation and financing prolonged visits in Germany.

Mats, Mats, Katarina, Andreas, Martin and Leif for good companionship within and outside the work, at many varying laboratories. Frank and Haik, Karsten and Torben and all other collegues and friends at TH Darmstadt, GSI, ISOLDE, GANIL and RIKEN and in Aarhus, Madrid, Moscow and Orsay.

I would also like to express my gratitude to my parents, for supporting me in many ways and for always encouraging me to proceed along any path that I have chosen to follow.

Finally, I would like to thank Anna, for being my anchor in the world outside physics and for coping with my frequent absences, physical and/or mental, and our son Carl, 3 months old, for diverting me from this work in the most charming way…

8. References

1. I. Tanihata, H. Hamagaki, O. Hashimoto, Y. Shida, N. Yoshikawa, K. Sugimoto, O. Yamakawa, T. Kobayashi, N. Takahashi, Phys. Rev. Lett. **56**(1985)2676
2. P.G. Hansen, B. Jonson, Europhys. Lett. **4**(1987)409
3. L. Johannsen, A.S. Jensen and P.G. Hansen, Phys. Lett. **B244**(1990)357
4. E. Arnold, J. Bonn, A. Klein, R. Neugart, M. Neuroth, E.W. Otten, P. Lievens, H. Reich, W. Widdra, Phys. Lett. **B281**(1992)16
5. E. Arnold, J. Bonn, A. Klein, R. Gegenwart, W. Neu, R. Neugart, E.W. Otten, G. Ulm, K. Wendt, Phys. Lett. **B197**(1987)311
6. R. Anne, S.E. Arnell, R. Bimbot, H. Emling, D. Guillemaud-Mueller, P.G. Hansen, L. Johannsen, B. Jonson, M. Lewitowicz, S. Mattsson, A.C. Mueller, R. Neugart, G. Nyman, F. Pougheon, A. Richter, K. Riisager, M.-G. Saint-Laurent, G. Schrieder, O. Sorlin, K. Wilhelmsen, Phys.Lett. **250B**(1990)19
7. R. Serber, Phys. Rev. **72**(1947)1008
8. B Blank, J.-J. Gaimard, H. Geissel, K.-H. Schmidt, H. Stelzer, K. Sümmerer, D. Bazin, R. Del Moral, J.P. Dufour, A. Fleury, F. Hubert, H.-G. Clerc and M. Steiner, Z. Phys **A343**(1992)375
9. G. Nyman, R.E. Azuma, P.G. Hansen, B. Jonson, P.O. Larsson, S. Mattsson, A. Richter, K. Riisager, O. Tengblad, K. Wilhelmsen, Nucl. Phys. **A510**(1990)189
10. M.J.G. Borge, P. G. Hansen, L. Johannsen, B. Jonson, T. Nilsson, G. Nyman, A. Richter, K. Riisager, O. Tengblad, K. Wilhelmsen and the ISOLDE Collaboration, Z. Phys. **A 340**(1991)255-261
11. I. Mukha, M.J.G. Borge, D. Guillemaud-Mueller, P. Hornshøj, F. Humbert, B. Jonson, T.E. Leth, G. Martinez Pinedo, T. Nilsson, G. Nyman, K. Riisager, G. Schrieder, M.H. Smedberg, O. Tengblad, K. Wilhelmsen Rolander, Accepted for publication in Phys. Lett. **B**
12. K. Wilhelmsen, **ß-decay of neutron rich nuclei**, Licenciate Thesis, Göteborg 1991 (unpublished)
13. E. Rutherford, A.B. Wood, Philos. Mag. **31**(1916)379
14. R.B. Roberts, R.C. Meyer, P. Wang, Phys. Rev. **55**(1939)510
15. V.A. Karnaukhov, G.M. Ter-Akopian, V.G. Subbotin, Proc. Asilomar Conf. Reactions between complex Nuclei, Eds. A. Ghiorso, R.M. Diamond, H.E. Conzett, University of California Press, Berkeley, Calif., (1963)434
16. V.I. Kuznetsov, N.K. Skobelev, Sov. J. Nucl. Phys. **5**(1967)810

17. R.E. Azuma, L.C. Carraz, P.G. Hansen, B. Jonson, K.-L. Kratz, S. Mattsson, G. Nyman, H. Ohm, H.L. Ravn, A. Schröder, W. Ziegert, Phys. Rev. Lett. **43**(1979)1652
18. R.E. Azuma, T. Björnstad, H.Å. Gustafsson, P.G. Hansen, B. Jonson, S. Mattsson, G. Nyman, A.M. Poskanzer, and H.L. Ravn, Phys. Lett. **B96**(1980)31
19. M. Langevin, C. Detraz, D. Guillemaud, F. Naulin, M. Epherre, R. Klapisch, S.K.T. Mark, M. De Saint Simon, C. Thibault, F. Touchard, Nucl. Phys. **A366**(1981)449
20. M.D. Cable, J. Honkanen, E.C. Schloemer, M. Ahmed, J.E. Reiff, Z.Y. Zhou, J. Cerny, Phys. Rev. **C30**(1984)1276
21. M. Langevin, C. Détraz, M. Epherre, D. Guillemaud-Mueller, B. Jonson, C. Thibault, Phys. Lett. **B146**(1984)176
22. J.P. Dufor, R. Del Moral, F. Hubert, D. Jean, M.S. Pravikoff, A. Fleury, A.C. Mueller, K.-H. Schmidt, K. Sümmerer, E. Hanelt, J. Frehaut, M. Beau, G. Giraudet, Phys. Lett. **B206**(1988)195
23. K. Riisager, M.J.G. Borge, H. Gabelmann, P.G. Hansen, L. Johannsen, B. Jonson, W. Kurcewicz, G. Nyman, A. Richter, O. Tengblad, K. Wilhelmsen, Phys. Lett. **B235**(1990)30
24. D. Bazin, R. Del Moral, J.P. Dufor, A. Fleury, F. Hubert, M.S. Pravikoff, R. Anne, P. Bricault, C. Détraz, M. Lewitowicz, Y. Zheng, D. Guillemaud-Mueller, J.C. Jacmart, A.C. Mueller, F. Pougheon, A. Richard, Phys. Rev. **C45**(1992)69
25. Particle Emission from nuclei, ed. D.N. Poenaru, M.S. Ivaşcu, CRC Press, Boca Raton, Florida
26. Y. Tosaka and Y. Suzuki, Nucl. Phys. **A512**(1990)46
27. G.F. Bertsch and H. Esbensen, Ann. Phys. **209**(1991)327
28. T. Otsuka, N. Fukunishi and H. Sagawa, Phys. Rev. Lett. **70**(1993)1385
29. M.V. Zhukov, B.V. Danilin, D.V. Fedorov, J.M. Bang, I.J. Thompson and J.S. Vaagen, Physics Reports **231**(1993) 151.
30. K. Riisager, Reviews of Modern Physics **66**(1994)1105
31. W.D. Myers and W.J. Swiatecki, Ann. Phys. **55**(1969)395
32. I. Tanihata, D. Hirata, T. Kobayashi, S. Shimoura, K. Sugimoto, H. Toki, Phys. Lett. **B289**(1992)261
33. D.V. Fedorov, A.S. Jensen and K. Riisager, Phys. Lett. **B312**(1993)1
34. D.V. Fedorov, A.S. Jensen and K. Riisager, Phys. Rev. **C49**(1994)201
35. V.M. Efimov, Comm. Nucl. Part. Phys **19**(1990)271
36. R.J. Glauber, Phys. Rev. **99**(1955)1515
37. C.A. Bertulani, G. Baur, Physics Reports **163**(1988)300
38. T. Kobayashi, O. Yamakawa, K. Omata, K. Sugimoto, T. Shimoda, N. Takahashi and I. Tanihata, Phys. Rev. Lett **60**(1988)2599

39. G. Münzenberg, H. Geissel, P. Armbruster, K.-H. Behr, B. Blank, K.H. Burkard, H.-G. Clerc, M. Chen, J.P. Dufour, B. Franczak, J.J. Gaimard, E. Hanelt, R. Kirchner, O. Klepper, B. Langenbeck, F. Nickel, K. Poppensieker, M.S. Pravikoff, E. Roeckl, D. Schardt, K.-H. Schmidt, H.-J. Schött, Th. Schwab, B. Sherrill, K. Sümmerer, H. Wollnik, GSI-89-80 Preprint (1989)
H. Geissel, P. Ambruster, K.H. Behr, A. Brünle, K. Burkard, M. Chen, H. Fogler, B. Franczak, H. Keller, O. Klepper, B. Langenbeck, F. Nickel, E. Pfeng, M. Pfützner, E. Roeckl, K. Rykaczewski, I. Schall, D. Schardt, C. Scheidenberger, K.-H. Schmidt, A. Schröter, T. Schwab, K. Sümmerer, M. Weber, G. Münzenberg, T. Brohm, H.-G. Clerc, M. Fauerbach, J.-J. Gaimard, A. Grewe, E. Hanelt, B. Knödler, M. Steiner, B. Voss, J. Weckenmann, C. Ziegler, A. Magel, H. Wollnik, J.P. Dufor, Y. Fujita, D.J. Viera and B. Sherrill, Nucl. Instr. Methods **B70** (1992) 286

40. B.M. Sherrill, D.J. Morrissey, J.A. Nolen, N. Orr, J.A. Winger, Nucl. Instr. Methods **B70** (1992) 298

41. N. Orr, Private communication

42. P.G. Hansen, contribution to ENAM -95, Arles

43. M. Zahar, M. Belbot, J. J. Kolata, K. Lamkin, R. Thompson, N. A. Orr, J. H. Kelley, R. A. Kryger, D. J. Morrisey, B. M. Sherrill, J. A. Winger, J.S. Winfield and A. H. Wuosmaa, Phys. Rev. **C48**(1993)1484-1487

44. K. Ieki, D. Sackett, A. Galonsky, C.A. Bertulani, J.J. Kruse, W.G. Lynch, D.J. Morrissey, N.A. Orr, H. Schulz, B.M. Sherrill, A. Sustich, J.A. Winger, F. Deák, Á. Horváth, Á. Kiss, Z. Seres, J.J. Kolata, R.E. Warner, D.L. Humphrey, Phys. Rev. Lett. **70**(1993)730

45. S. Shimoura, T. Nakamura, M. Ishihara, N. Inabe, T. Kobayashi, T. Kubo, R.H. Siemssen, I. Tanihata, Y. Watanabe, Phys. Lett. **B348**(1995)29

46. D. Sackett, K. Ieki, A. Galonsky, C.A. Bertulani, H. Esbensen, J.J. Kruse, W.G. Lynch, D.J. Morrissey, N.A. Orr, B.M. Sherrill, H. Schulz, A. Sustich, J.A. Winger, F. Deák, Á. Horváth, Á. Kiss, Z. Seres, J.J. Kolata, R.E. Warner, D.L. Humphrey, Phys. Rev. **C48**(1993)188

47. M.V. Zhukov, B. Jonson, Nucl. Phys. **A589**(1995)1

48. I.J. Thompson, M.V. Zhukov, Phys. Rev. **C49**(1994)49

49. A.A. Korsheninnikov, K. Yoshida, D.V. Aleksandrov, N. Aoi, Y. Doki, N. Inabe, M. Fujimaki, T. Kobayashi, H. Kumagai, C.-B. Moon, E.Yu. Nikolskiy, M.M. Obuti, A.A. Ogloblin, A. Ozawa, S. Shimoura, T. Suzuki, I. Tanihata, Y. Watanabe and M. Yanokura, Phys. Lett. **B326**(1994)31.

50. A.N. Ostrowski, H.G. Bohlen, B. Gebauer, S.M. Grimes, R. Kalpakchieva, Th. Kirchner, T.N. Massey, W. von Oertzen, Th. Stolla, M. Wilpert, Th. Wilpert, Phys. Lett. **B338**(1994)13.

51. H.G. Bohlen, B. Gebauer, Th. Kirchner, M. von Lucke-Petsch, W. von Oertzen, A.N. Ostrowski, Ch. Seyfert, Th. Stolla, M. Wilpert, Th. Wilpert, S.M. Grimes, T.N. Massey, R. Kalpakchieva, Y.E. Penionzhkevich, D.V. Alexandrov, I. Mukha, A.A. Ogloblin and C. Detraz, Nucl. Phys. **A583**(1995)775

52. H.G. Bohlen, B. Gebauer, M. von Lucke-Petsch, W. von Oertzen, A.N. Ostrowski et. al., Z. Phys. **A344**(1993)381

53. B. Young, W. Benenson, M. Fauerbach, J.H. Kelley, R. Pfaff, B. Sherrill, M. Steiner, J. Winfield, T. Kubo, M. Hellström, N. Orr, J. Stetson, J. Winger, and S. Yennello, Phys. Rev. Lett. **C71**, 25(1993)4124

54. B. Young, W. Benenson, J.H. Kelley, R. Pfaff, B. Sherrill, M. Steiner, J. Winfield, T. Kubo, M. Hellström, N. Orr, J. Stetson, J.A. Winger, and S. Yennello, Phys. Rev. **C49**(1994)279

55. R.A. Kryger,A. Azhari, A. Galonsky, J.H. Kelley, R. Pfaff, E. Ramakrishnan, D. Sackett, B.M. Sherrill, M. Thoennessen, J.A. Winger and S. Yokahama, Phys. Rev. **C47**(1993)2439

56. M. P. J. Zinser, PhD Thesis, ”Aufbruchreaktionen hochenergetischer Neutron-Halo Kerne”, Johannes Gutenberg-Universität Mainz

57. S. Neumaier, G.D. Alkhazov, M.N. Andronenko, T. Beha, K.-H. Behr, A. Brünle, K. Burkhard, A.V. Dobrovolsky, P. Egelhof, C. Fischer, G.E. Gavrilov, H. Geissel, V.I. Iatsoura, H. Irnich, A.V. Khanzadeev, G.A. Korelev, A.A. Lobodenko, P. Lorenzen, G. Münzenberg, M. Mutterer, F. Nickel, W. Schwab, D.M. Seliverstov, P. Singer, T. Suzuki, J.P. Theobald, N.A. Timofeev, A.A. Vorobyov, Nucl. Phys. **A583**(1995)799

58. A.A. Korsheninnikov, K. Yoshida, D.V. Aleksandrov, N. Aoi, Y. Doki, N. Inabe, M. Fujimaki, T. Kobayashi, H. Kumagai, C.-B. Moon, E.Yu. Nikolskii, M.M. Obuti, A.A. Ogloblin, A. Ozawa, S. Shimoura, T. Suzuki, I. Tanihata, Y. Watanabe and M. Yanokura, Phys. Lett. **B316**(1993)38.

59. R. Anne, R. Bimbot, S. Dogny, H. Emling, D. Guillemaud-Mueller, P.G. Hansen, P. Hornshøj, F. Humbert, B. Jonson, M. Keim, M. Lewitowicz, P. Møller, A.C. Mueller, R. Neugart, T. Nilsson, G. Nyman, F. Pougheon, K. Riisager, M.G. Saint-Laurent, G. Schrieder, O. Sorlin, O. Tengblad and K. Wilhelmsen Rolander, Nucl. Phys. **A575** (1994) 125

60. M.J.G. Borge, D. Guillemaud-Mueller, P.G. Hansen, P. Hornshøj, F. Humbert, B. Jonson, A.C. Mueller, P. Møller, T. Nilsson, G. Nyman, A. Richter, K. Riisager, G. Schrieder, O. Tengblad and K. Wilhelmsen, Proposal to the ISO-LDE committee

61. K.-H. Schmidt, E. Hanelt, H. Geissel, G. Münzenberg, J.P. Dufor, Nucl. Instr. and Meth. **A260**(1987)287

62. Review of Particle Properties, Phys. Rev. **D50**(1994)

63. H. Geissel, G. Münzenberg and K. Riisager, To be published in Annu. Rev. Nucl. Part. Sci. (1995)

64. M. Bernas, S. Czajkowski, P. Armbruster, H. Geissel, Ph. Dessagne, C. Donzaud, H.–R. Faust, E. Hanelt, A. Heinz, M. Heese, C. Kozhuharov, Ch. Miehe, G. Müznenberg, M. Pfutzner, C. Rohl, K.-H. Schmidt, W. Schwab, C. Stephan, K. Sümmerer, L. Tassan-Got, B. Voss, Phys. Lett. **B331**(1994)19

65. **Report on the european radioactive beam facilities**, NuPECC Study Group, 1993

66. R. Anne, D. Bazin, A.C. Mueller, J.C. Jacmart, M. Langevin, Nucl. Instr. and Meth. **A257**(1987)215

67. H. Ravn, Nucl. Instr. and Meth. **B70**(1992)107

68. G. Charpak and F. Sauli, Nucl. Instr. and Meth. **162**(1979)405

69. J. Bialkowski, M. Moszynski and D Wolski, Nucl. Instr. and Meth. **A275**(1989)322

70. D Wolski, M. Moszynski, T. Ludziejewski, A. Johnson, W. Klamra, Ö. Skeppstedt, Nucl. Instr. and Meth. **A360**(1995)584

71. G. Pausch, W. Bohne, H. Fuchs, D. Hilscher, H. Homeyer, H. Morgenstern, A. Tutay, W. Wagner, Nucl. Instr. and Meth. **A322**(1992)43

72. Th. Blaich, Th.W. Elze, H. Emling, H. Freiesleben, K. Grimm, W. Henning, R. Holzmann, G. Ickert, J.G. Keller, H. Klingler, W. Kneissl, R. König, R. Kulessa, J.V. Kratz, D. Lambrecht, J.S. Lange, Y. Leifels, E. Lubkiewicz, M. Proft, W. Prokopowicz, C. Schütter, R. Schmidt, H. Spies, K. Stelzer, J. Stroth, W. Walus, E. Wajda, H.J. Wollersheim, M. Zinser and E. Zude, Nucl. Instr. Meth. **A314**(1992)136 and LAND Collaboration, GSI Scientific Report (1993).

73. H.G. Essel, H. Grein, T. Kroll, W. Kynast, M. Richter, H. Sohlbach, W. Spreng, K. Winkelmann, W.F.J. Müller, IEEE Transactions on Nucl. Science, NS-34, No. 4, (1987) 907-911

74. T. Blaich, R. Freifelder, N. Herrmann, J. Keller, P. Kozon, M. Krämer, Y. Leifels, V. Lindenstruth, W. Müller, R. Schmidt and K. Teh, GSI Scientific Report (1990)311

75. J.C. Angélique, L. Axelsson, G. Bizard, W.N. Catford, N.M. Clarke, G. Costa, M. Freer, S. Grevy, D. Guillemaud-Mueller, G.J. Gyapong, F. Hanappe, B. Heusch, B. Jonson, C. Le Brun, F.R. Lecolley, F. Lefebvres, M. Lewitowicz, E. Liegard, F.M. Marqués, G. Martinéz, A.C. Mueller, T. Nilsson, A. Ninane, G. Nyman, N.A. Orr, B. Peterson, F. Pougheon, K. Riisager, M.G. Saint-Laurent, Y. Schutz, M. Smedberg, O. Sorlin, L. Stuttgé and D.D. Warner, LPC Internal Report LPCC 95-10, Cont. to ENAM -95

76. PAW, Physics Analysis Workstation, CERN Program Library Long Writeup Q121, Version 2.03 (1993)

77. R. Anne, S.E. Arnell, R. Bimbot, S. Dogny, H. Emling, H. Esbensen, D. Guillemaud-Mueller, P.G. Hansen, P. Hornshøj, F. Humbert, B. Jonson, M. Keim, M. Lewitowicz, P. Møller, A.C. Mueller, R. Neugart, T. Nilsson, G. Nyman, F. Pougheon, K. Riisager, M.-G. Saint-Laurent, G. Schrieder, O. Sorlin, O. Tengblad, K. Wilhelmsen Rolander, D. Wolski, Phys. Lett. **B304**(1993)55

78. P. Désesquelles, A.J. Cole, A. Dauchy, A. Giorni, D. Heuer, A. Lleres, C. Morand, J. Saint-Martin, P. Stassi, J.B. Viano, B. Chambon, B. Cheynis, B. Drain and C. Pastor, Nucl. Instr. and Meth. **A307**(1991)366

79. S.E. Arnell, H.A. Roth, Ö. Skeppstedt, J. Bialkowski, M. Moszyski, D. Wolski and J. Nyberg, Nucl. Instr. and Meth. **A300**(1991)303

80. M.J.G. Borge, M. Epherre-Rey-Campagnolle, D. Guillemaud-Mueller, B Jonson, M. Langevin, G. Nyman, and C. Thibault, Nucl. Phys. **A460**(1986)373

81. T. Nilsson, **Development of an energy-loss detector for charged particles**, Diploma Thesis, Göteborg 1989 (unpublished)

82. F. Wenander, **A study of a telescope detector**, Diploma Thesis, Göteborg 1995 (unpublished)

83. H. Stelzer, Nucl. Instr. Meth. **A310**(1993)103

84. The ALADIN Collaboration, GSI Scientific Report, Darmstadt, (1989) 292.

85. R.S. Henderson, O. Hausser, K. Hicks, C. Gunter, W. Faszer, R. Sawafta and N. Poppe, Nucl. Instr. Meth. **A254** (1987) 61.

86. F. Humbert, PhD Thesis, ”Kinematisch vollständige Messung der Aufbruchreaktionen von leichten, neutronenreichen Kernen am Beispiel des Halokerns ^{11}Li”, Technische Hochschule Darmstadt (1995)

87. H. Simon, Diplomarbeit ”Untersuchung an einem Magnetspektrometer für Experimente mit exotischen Strahlen”, Technische Hochschule Darmstadt (1994), unpublished.

88. K. Riisager, Dr. scient thesis ”Residence in forbidden regions”, Aarhus University (1994), unpublished.

89. A.S. Goldhaber, Phys. Lett. **B53**(1974)306

90. P. Nadel-Turonski, T. Ranman, Diploma Thesis, Göteborg, in preparation.

91. M.V. Zhukov, A.A. Korsheninnikov and M.H. Smedberg, Phys. Rev. C **50**(1994)R1

92. J. Kolata, private communication with M Zhukov, 1995.

93. K. Riisager, R. Anne, S.E. Arnell, R. Bimbot, H. Emling, D. Guillemaud-Mueller, P.G. Hansen, L. Johannsen, B. Jonson, A. Latimier, M. Lewitowicz, S. Mattsson, A.C. Mueller, R. Neugart, G. Nyman, F. Pougheon, A. Richter, M.G. Saint-Laurent, G. Schrieder, O. Sorlin and K. Wilhelmsen, Nucl. Phys **A540**(1992) 365.

94. T. Nilsson, F. Humbert, W. Schwab, M. Zinser, Th. Blaich, M.J.G. Borge, L.V. Chulkov, H. Eickhoff, Th.W. Elze, H. Emling, B. Franzke, H. Freiesleben, H. Geissel, K. Grimm, D. Guillemaud-Mueller, P.G. Hansen, R. Holzmann, H. Irnich, L. Johannsen, B. Jonson, J.G. Keller, O. Klepper, H. Klingler, J.V. Kratz, R. Kulessa, D. Lambrecht, Y. Leifels, A. Magel, M. Mohar, E.F. Moore, A.C. Mueller, G. Münzenberg, P. Møller, F. Nickel, G. Nyman, A. Richter, K. Riisager, C. Scheidenberger, G. Schrieder, B.M. Sherrill, H. Simon, K. Stelzer, J. Stroth, O. Tengblad, W. Trautmann, E. Wajda and E. Zude, Nucl. Phys. **A583**(1995)795-798c

95. Y. Ohbayasi, Y. Suzuki, Phys. Lett. **B346**(1995)223

96. F. Ajzenberg-Selove, Nucl. Phys **A490**(1988) 1, Nucl. Phys **A506**(1990) 1.

97. T. Nakamura, S. Shimoura, T. Kobayashi, T. Teranishi, K. Abe, N. Aoi, Y. Doki, M. Fujimaki, N. Inabe, N. Iwasa, K. Katori, T. Kubo, H. Okuno, T. Suzuki, I. Tanihata, Y. Watanabe, A. Yoshida and M. Ishihara, Phys. Lett. **B331**(1994) 296

98. P.G. Hansen, A.S. Jensen and B. Jonson, To be published in Annu. Rev. Nucl. Part. Sci. (1995).

99. R. Holzmann for the LAND Collaboration + members of the CB and FRS Collaborations + many others, Proposal to GSI.

100. M. Loiselet, N. Postiau, G. Ryckewaert, R. Coszach, Th. Delbar, W. Galster, P.Leleux, I. Licot, E. Lienard, P. Lipnik, C. Michotte, J. Vervier, P. Decrock, M. Gaelens, M. Huyse, G. Vancraeynest, P. van Duppen, F. Binon, P. Duhamel, J. Vanhorenbeeck, Proc. III RNB conf., MSU, (1993) 179

101. **R**adioactive beam **EX**periments at **ISOLDE**, Proposal to the ISOLDE Committee, Aarhus - Brookhaven - Daresbury - Darmstadt - Dubna - Erlangen - Frankfurt - Gothenburg - Göttingen - Heidelberg - Leuven - Liverpool - Mainz - München - Paris - Saclay - Stockholm - Strasbourg - Surrey - Roskilde - Villeurbanne and CERN-ISOLDE collaboration, CERN/ISC 94-25

102. The SPIRAL Radioactive Ion Beam Facility, ed. M. Bex, GANIL Report R 94 02

103. Rutherford Appleton Laboratory WWW-server, nov. 1995

104. RI Beam Factory, I. Tanihata, RIKEN Report 1994

Index